Chem Soc Rev

Towards High-Efficiency Nanoelectrocatalysts for Oxygen Reduction through Engineering Advanced Carbon Nanomaterials

Journal:	*Chemical Society Reviews*
Manuscript ID	CS-SYN-05-2015-000414.R2
Article Type:	Review Article
Date Submitted by the Author:	15-Nov-2015
Complete List of Authors:	Zhou, Ming; Northeast Normal University, Faculty of Chemistry, and National & Local United Engineering Laboratory for Power Batteries Wang, Hsing-Ling; Los Alamos National Laboratory, Physical Chemistry and Applied Spectroscopy, Chemistry Division Guo, Shaojun; Peking University, Department of Materials Science and Engineering, & Department of Energy and Resources Engineering, College of Engineering

SCHOLARONE™
Manuscripts

Journal Name

ARTICLE

ROYAL SOCIETY OF CHEMISTRY

Towards High-Efficiency Nanoelectrocatalysts for Oxygen Reduction through Engineering Advanced Carbon Nanomaterials

Ming Zhou,*[†] Hsing-Lin Wang*[§] and Shaojun Guo*[#]

One of the critical issues in the industrial development of fuel cells (*e.g.*, proton exchange membrane fuel cells, direct methanol fuel cells and biofuel cells) is the high cost, serious intermediate tolerance, anode crossover, sluggish kinetics, and poor stability of the platinum (Pt) as the preferred electrocatalysts for oxygen reduction reaction (ORR) at cathode. The development of novel noble-metal-free electrocatalysts with low cost, high activity and practical durability for ORR has been considered as one of the most active and competitive fields in chemistry and materials science. In this critical review, we will summarize recent advances on engineering advanced carbon nanomaterials with different dimensions for the rational design and synthesis of noble-metal-free oxygen reduction electrocatalysts including heteroatom-doped carbon nanomaterials, transition metal-based nanoparticles (NPs)-carbon nanomaterials composites and especially the stable iron carbide (Fe₃C)-based NPs-carbon nanomaterials composites. Introducing advanced carbon nanomaterials with high specific surface area and stable structure into the noble-metal-free ORR field has not only led to a maximized electrocatalyst surface area for the electron transfer but also resulted in an enhanced electrocatalyst stability for the long-term operation. Therefore, the rational design and synthesis of noble-metal-free electrocatalysts based on heteroatoms, transition metal-based NPs and Fe₃C-based NPs functionalized carbon nanomaterials are of special relevance for their ORR applications, and represents a rapidly growing branch of research. The demonstrated examples in this review will open new directions on designing and optimizing advanced carbon nanomaterials for the development of extremely active and durable earth-abundant cathodic catalysts for fuel cells applications.

1. Introduction

The rapid increase in the global energy consumption and the environmental impact of traditional energy resources pose serious challenges to human health, energy security, and environmental protection.[1, 2] With the ever-increasing demand for next generation renewable and sustainable energy conversion technologies, it is undoubted that the substitution of economic and sustainable clean energy for traditional fossil fuels is becoming a necessity.[3-8] Fuel cells are clean and efficient energy conversion devices that can directly convert the chemical energy of fuels to electricity through electrochemical processes.[9-16] The first fuel cells were separately invented by Welsh physicist William Grove[17] and German physicist Christian Friedrich Schönbein[18] in the 1830s. The first commercial use of fuel cells came more than a century later in Gemini mission by National Aeronautics and Space Administration (NASA) to generate power for probes, satellites and space capsules in the 1960s.[19-21] By using hydrogen (H₂) or methanol as fuels and oxygen (O₂) as reductants, fuel cells can be operated at close to room temperature, and are considered as promising power solutions for future electric vehicles and portable electronic devices, **Fig. 1A**.[22-38] The cathodic reaction on fuel cells is the oxygen reduction reaction (ORR). In the conventional fuel cell technology, the noble-metal platinum (Pt) is used as a preferred and effective four-electron transfer (rather than the ineffective two-electron pathway) ORR electrocatalyst in both alkaline and acidic conditions (**Fig. 1B**), mainly because of its excellent electrocatalytic activity.[32, 36, 39-54]

In spite of recent significant technological advances, a couple of major challenges retain on the way to the widespread application of Pt as the ORR electrocatalysts:[32, 36, 39-62] (i) scarcity. The total loading and total content of Pt proposed by the U.S. Department of Energy (DOE) Fuel Cell Technologies Program in 2013 are 0.15 mg cm⁻² and 0.14 g kW⁻¹, respectively.[63, 64] On the basis of Pt price revised by U.S. DOE, the cost of Pt electrocatalyst still accounts for 49% of the proton exchange membrane fuel cells stack cost and 24% of the 80 kW_net proton exchange membrane fuel cells system cost.[63-65] Therefore, the cost of fuel cells is directly linked to the price of Pt in the volatile and highly monopolized precious metal market; (ii) easy deactivation by carbon monoxide (CO)

[†] *Faculty of Chemistry, and National & Local United Engineering Laboratory for Power Batteries, Northeast Normal University, Changchun, Jilin Province 130024, P.R. China. E-mail: zhoum739@nenu.edu.cn*

[#] *Department of Materials Science and Engineering, & Department of Energy and Resources Engineering, College of Engineering, Peking University, Beijing 100871, P.R. China. Email: guosj@pku.edu.cn*

[§] *Physical Chemistry and Applied Spectroscopy, Chemistry Division, Los Alamos National Laboratory, Los Alamos, New Mexico 87545, United States. E-mail: hwang@lanl.gov*

poisoning. Pt electrocatalysts are very sensitive to CO that cannot be completely separated from H_2 fuel by current engineering technology; even trace amounts of CO can be adsorbed preferentially onto the electrocatalytic active sites of Pt, resulting in a diminished catalytic activity; (iii) the fuel crossover effect caused by undesired catalytic oxidation of leaked fuel. In relation to the use of methanol as fuel in direct methanol fuel cells, methanol steam can permeate into the cathode chamber and poison Pt electrocatalysts due to the presence of crossover effects, thus greatly reducing electrocatalysts' lifespan; (iv) durability issues for Pt electrocatalysts are particularly critical because of the highly aggressive conditions of low pH, dissolved molecular oxygen, and the high positive potentials at which they operate.[60-62, 66-69] Pt nanoparticles (NPs) can dissolve and redeposit on other Pt NPs, and Pt can deposit in the membrane through the reduction of Pt^{2+} by H_2 diffusing from the anode (hydrogen crossover).[60, 61, 66, 70-72] Therefore, in one word, all the above drawbacks prevent the large-scale practical application of fuel cells, though alkaline fuel cells with Pt as an ORR electrocatalyst were successfully developed for the Gemini and the Apollo lunar missions carried by NASA in the1960s.[19-21, 73-76]
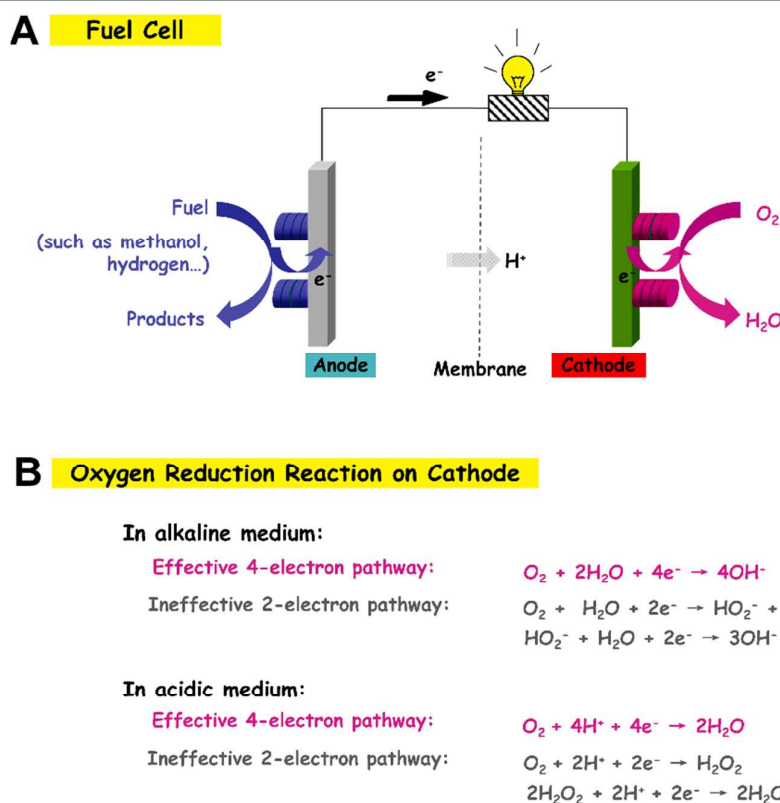

Fig. 1 (A) The typical fuel cells with methanol or H_2 as fuel. (B) ORR pathways in alkaline and acidic media.

At this juncture, how to reduce the costs by decreasing cathode Pt loadings or replacing Pt with other materials and meantime maintain the high performance is the crucial subject of most current ORR electrocatalytic researches. Recently, much effort has been devoted to developing low-cost and high-efficient ORR electrocatalysts through decreasing Pt content by synthesizing Pt-cheap metal composites,[43, 53, 77-80] developing transition metal-based NPs electrocatalysts,[77, 78, 81-92] or fabricating metal-free NPs electrocatalysts.[93-167] Among these directions, a major trend in fuel cells research and development (R&D) is the development of noble-metal-free electrocatalysts [*e.g.*, metal-free NPs, noble-metal-free transition metal-based NPs, and especially the stable iron carbide (Fe_3C)-based NPs] with outstanding features of low cost, high activity, high tolerance to deactivation by CO and crossover effect by methanol, and long durability for ORR.[8, 42, 55-58, 168-176] Carbon offers the unmatched versatility among the elements of the periodic table.[177-181] By combining the advantages of carbon materials with those of nanostructured materials, the advanced carbon nanomaterials with different dimensions have been widely used as the nanoscale support in the design and synthesis of electrocatalysts with superior performance.[8, 23, 42, 55-58, 169-175, 178-180, 182-196] In recent years, it has been reported that the introduction of advanced carbon nanomaterials into the noble-metal-free ORR field will further boost the ORR performance of these noble-metal-free electrocatalysts, which results in a fast growing branch of ORR electrocatalysts, **Fig. 2**.[65, 77, 78, 81-167, 176, 194-204]
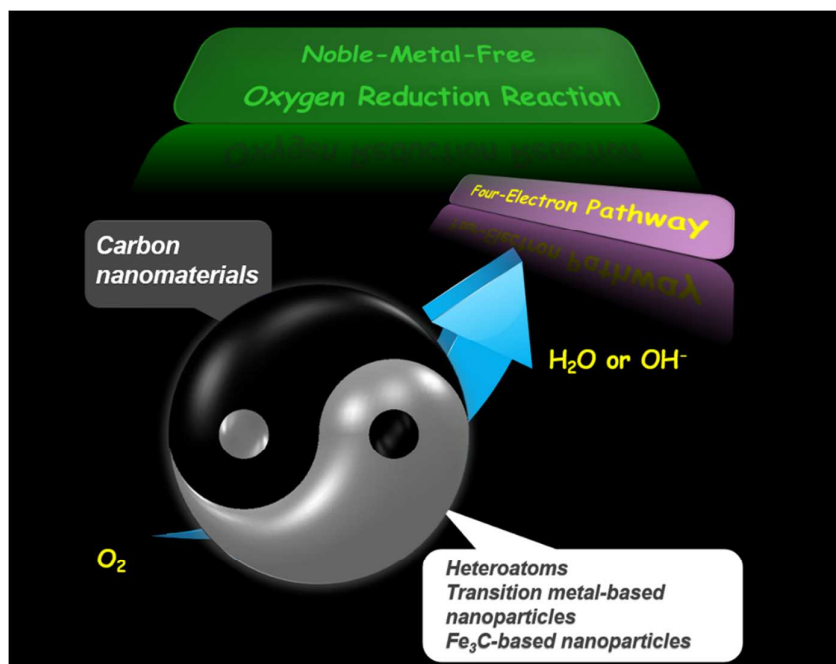
Fig. 2 Schematic illustration of the high-efficiency carbon nanomaterials-based noble-metal-free oxygen reduction electrocatalysts, which combine the advantages of carbon nanomaterials with large surface area/stable structure and heteroatoms/transition metal-based NPs/Fe$_3$C-based NPs with high ORR electrocatalytic activity.

The metal-free heteroatom-doped carbon nanomaterials are a new class of promising ORR electrocatalysts because they exhibit comparable or higher electrocatalytic activity, longer-term stability, and better tolerance against fuel crossover and CO poisoning effects compared to the commercial Pt/C electrocatalyst.[93, 95-167, 205-214] Both theoretical calculations and experimental results suggest that the substitution of carbon atom with heteroatoms in the sp^2 lattice of graphitic carbon can change the electronic arrangement of carbon-based material and tailor their electron donor property, and subsequently create the favorable sites for oxygen adsorption or splitting, thus offering the improved ORR electrocatalytic activity.[8, 42, 55-58, 169-173, 176, 215] Therefore, the development of advanced carbon nanomaterials being doped by single or multiple heteroatoms for the production of low-cost heteroatom-doped carbon-based nanomaterials with superior ORR electrocatalytic activities is highly desired.

In addition to the heteroatom-doped carbon nanomaterials, advanced carbon nanomaterials supported transition metal-based NPs is another kind of popular noble-metal-free electrocatalysts for enhancing ORR.[77, 78, 81-87, 89-92] By introducing carbon nanomaterials with different dimensions into transition metal-based NPs, the attractive assembly of transition metal-based NPs supported on carbon nanomaterials exhibits higher activity and stability in the ORR relative to their unsupported counterparts. Such superior performance would be attributed to the synergetic effect between carbon nanomaterials with large surface area/stable structure and the transition metal-based NPs with high ORR electrocatalytic activities, which in turn leads to stable and robust transition metal-based NPs/carbon nanomaterials composite surfaces with superior electrocatalytic ORR performances.[77, 78, 81-87, 89-92, 174, 175]

Owing to the harsh ORR conditions especially in acidic media, only a few types of materials have been found to be active and durable towards the ORR, such as metal-free heteroatom-doped carbon nanomaterials[95, 105] and the noble-metal-free transition metal-based NPs functionalized carbon nanomaterials mentioned above.[14, 65, 83, 88, 175, 216] Among them, the best one is the transition metal-based NPs functionalized carbon nanomaterials (*e.g.,* Fe-N-C) where the active sites are believed to involve surface nitrogen coordinated with iron.[14, 65, 202, 217] Three main types of sites in Fe-N/C have been identified:[60, 177, 199] (i) FeN$_4$/C sites where N is a nitrogen atom of the pyrrolic type; (ii) FeN$_4$/C sites where N is a nitrogen atom of the pyridinic type, and (iii) C-N sites. Among these three sites, the most active one is the FeN$_4$/C of the pyridinic type for which Fe is coordinated to the carbon support by four pairs of electrons, one pair *per* pyridinic nitrogen atom.[218] However, the leaching problem and low active site density (optimum iron content in Fe-N/C electrocatalysts is usually < 0.2 wt.%[219]) may cause a relatively poor durability, especially in acidic medium. Recently, a novel spherical ORR electrocatalyst based on graphitic shell encased Fe$_3$C NPs was reported to be highly active and stable for ORR.[182, 200, 202] On the surface of these electrocatalysts, little nitrogen or metallic functionality was detected while the electrocatalysts exhibited high activity and stability towards the ORR during rotating disk electrode measurements.[202] Also, the inner Fe$_3$C NPs, being protected by outer graphitic layers, play a synergetic role in activating the outer graphitic layers towards ORR.[202] These

nanomaterials have emerged as a kind of exciting "rising star" ORR electrocatalysts with superior and stable performance.

Advanced carbon nanomaterials-based noble-metal-free electrocatalysts are currently of great interest for chemistry, nanomaterials and nanotechnology, electrochemical energy and storage and electroanalysis. Several reviews were published recently on the topic of either heteroatom-doped carbon nanomaterials[55, 56, 168, 170, 171, 176, 194-196] or transition metal-based NPs[174, 175] for oxygen reduction. However, most of the existed reviews are concentrated on the advances on heteroatoms or transition metal-based NPs in ORR. Our review focuses on the most recent development of advanced carbon nanomaterials with different dimensions as the support for heteroatoms, transition metals-based NPs and especially Fe_3C-based NPs for the rational design and synthesis of high-efficiency noble-metal-free oxygen reduction electrocatalysts. This review has taken into consideration of the most recent developments and presented comprehensive discussion of rational design of the growing family of advanced carbon nanomaterials-based noble-metal-free ORR electrocatalysts in order to provide insights for developing novel and high-efficiency noble-metal-free ORR electrocatalysts.
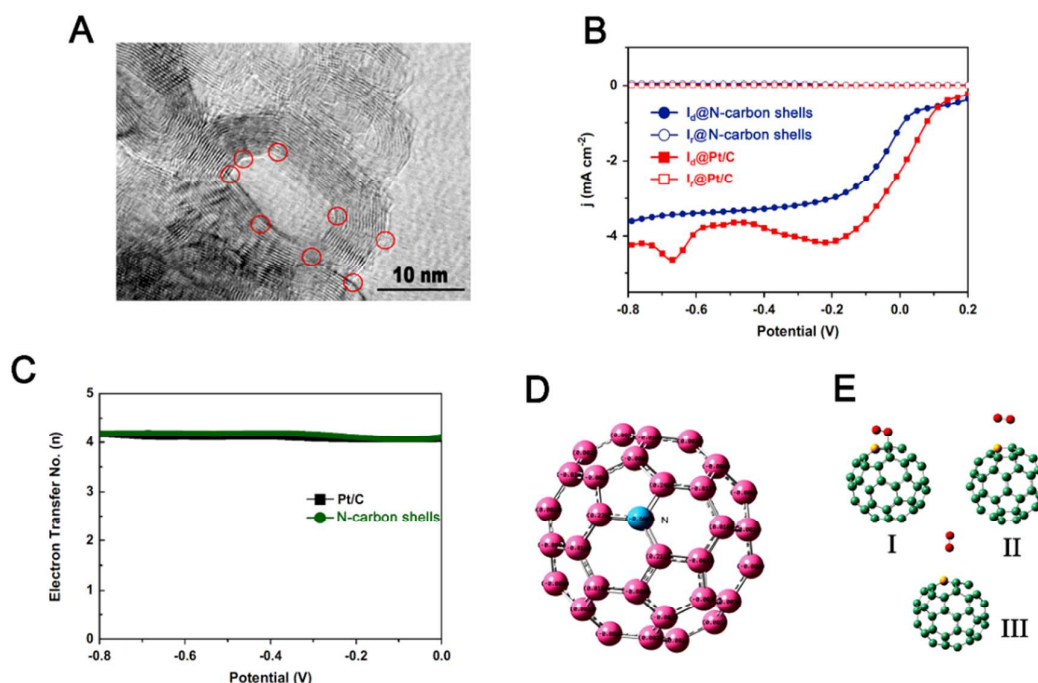
Fig. 3 (A) TEM image of N-carbon shells. (B) Rotating ring-disk electrode tests for N-carbon shells and Pt/C in O_2-saturated 0.1 M KOH with the rotating rate of 1600 rpm and the scan rate of 5 mV s^{-1}. I_d: disk current; I_r: ring current. (C) Electron-transfer numbers *per* oxygen molecule for N-carbon shells and Pt/C. (D) Calculated charge density distribution for N-C_{60} with the molecular formula of $C_{59}N$ as an example. (E) Schematic representations of three possible adsorption modes of an oxygen molecule on $C_{59}N$: HH1 Pauling model (I), HH2 Pauling model (II), and HHV Pauling model (III), respectively. (Adapted with permission from Ref [93] Copyright 2015 Elsevier.)

2. Engineering Carbon Nanomaterials for ORR

2.1 Heteroatom-Doped Zero-Dimensional (0D) Fullerene

The 0D C_{60} fullerene is deemed to being formed by wrapping up two-dimensional (2D) graphene (GN).[220] Since C_{60} was discovered in 1985,[221] the increasing interest and significance of the work in the fullerene field have generated the award of the 1996 Nobel Prize in Chemistry to the discoverers, Smalley, Curl, and Kroto.[222-224] C_{60} has been found to exhibit a wide range of interesting properties, in respect to electrical conductivity,[225] charge transport,[226] and photophysical behavior.[227] Besides C_{60} was extensively used as an electron acceptor, it also reveals a rich electrochemistry because of the unique dimensional and electronic structures.[228]

Nitrogen-doped carbon shells (N-carbon shells). By utilizing the first-principles spin-polarized density functional theory (DFT) calculations, it was predicted that the full catalytic ORR cycles could be completed energetically on 0D heteroatom-doped C_{60} fullerene, *i.e.*, nitrogen-doped C_{60} (N-C_{60}).[94] This has recently been experimentally proven that the fullerene-like nitrogen-doped carbon shells (N-carbon shells), produced by deliberately pyrolyzing fallen gingko leaves under N_2 atmosphere at high temperature, could be applied as the effective ORR electrocatalyst.[93] The red circles in **Fig. 3A** indicate the sharp turns with the ring structure of the N-carbon shells, which may result from the integration of nitrogen into the graphitic structure and accordingly would lead to more active sites than the basal plane of graphitic carbons. The ORR experimental results show that the obtained N-carbon shells exhibit high electrocatalytic activity for ORR, which is comparable to the commercial Pt/C, 20 wt.% Pt loading (**Fig. 3B**). The electron-transfer number *per* oxygen molecule on N-carbon shells is 4.1, indicating a four-electron transfer process of ORR (**Fig. 3C**). The theoretical calculations

were also explored to better understand the effect of nitrogen doping on the ORR of N-carbon shells. Due to the limited number of atoms that can be introduced in the model calculation, the N-C_{60} with the molecular formula of $C_{59}N$ was explored as a model for this study (**Fig. 3D**). Quantum mechanics calculations with B3LYP density functional theory (Gaussian03) indicate that the oxygen adsorption may process on the HH Pauling site (HH1), HP Pauling site, and HH C-C site of N-C_{60} (**Fig. 3E**). Because the carbon atoms adjacent to nitrogen dopants possess a considerably higher positive charge to counter balance the strong electronic affinity of the N atom, a free O_2 molecule can be adsorbed onto HH1 more easily compared to other two sites, suggesting that HH1 is a more likely adsorption mode for an O_2 molecule at the N-C_{60}. The N-induced charge delocalization can facilitate the optimal chemisorption mode of O_2, aside-on adsorption (HH1 Pauling site, **Fig. 3F**), onto the N-C_{60}. The biased diatomic adsorption can effectively weaken the O-O bonding and lower the adsorption energy to facilitate ORR at N-C_{60}. As such, doping carbon fullerene with nitrogen heteroatoms as in the N-C_{60} can

effectively create the metal-free active sites for the electrochemical reduction of O_2.[94]

2.2 Heteroatom-Doped 1D Carbon Nanotubes (CNTs)

The 1D CNTs can be considered as a 2D GN sheet rolled up into a nanoscale tube (which are single-wall CNTs), or with additional GN sheets around the core of a single-wall CNTs (called multi-wall CNTs).[220] These CNTs have the diameters in the range between fractions of nanometers and tens of nanometers and lengths up to several centimetres. Since their initial discovery by Iijima in 1991 when they were produced from a cathode by a carbon-are discharge method similar to that used for preparing C_{60}.[229] Because of their unique structural, electronic properties, high chemical stability, and extremely high mechanical strength and modulus,[230] CNTs have exhibited a wide range of potential applications including use as a high sensitivity microbalance,[231] gas detector,[232] catalyst support,[233] electron source in fields of emission mode for display,[234] tiny tweezers for nanoscale manipulation,[235] and probe tips for scanning probe microscopy.[236]
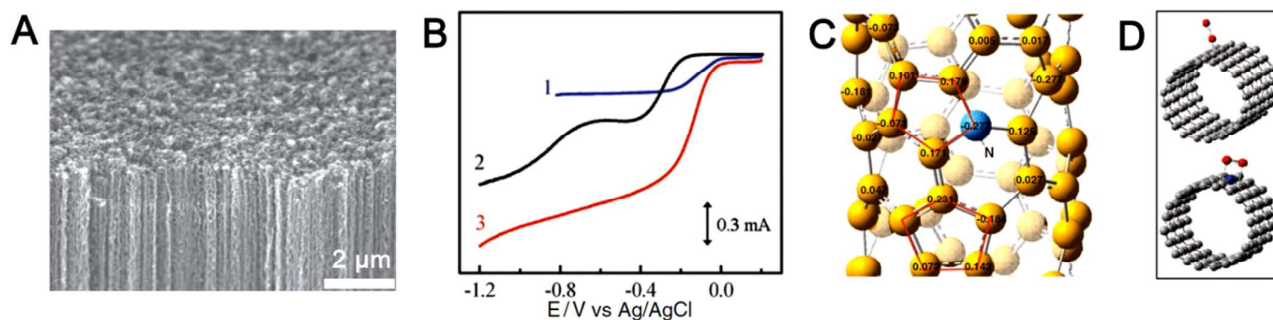

Fig. 4 (A) SEM image of vertically aligned N-CNTs. (B) Linear-sweep voltammetry (LSV) curves for ORR in air-saturated 0.1 M KOH at the Pt/C (curve 1), vertically aligned CNTs (curve 2), and vertically aligned N-CNTs modified glassy carbon electrodes (curve 3). (C) Calculated charge density distribution for the N-CNTs. (D) Schematic representations of possible adsorption modes of an oxygen molecule at the CNTs (top) and N-CNTs (bottom). (Adapted with permission from Ref [107] Copyright 2009 American Association for the Advancement of Science.)

2.2.1 Single heteroatom-doped CNTs

Nitrogen doped CNTs (N-CNTs). In 2009, Dai and co-workers reported that vertically aligned N-CNTs (**Fig. 4A**) produced by the pyrolysis of iron(II) phthalocyanine[237] could be used as an effective electrocatalyst for ORR in alkaline electrolyte.[107] The half-wave potentials for ORR at the vertically aligned N-CNTs electrode is comparable to that at the commercial Pt/C with 20 wt.% Pt loading (**Fig. 4B**). Control experiments suggest that compared with the nonaligned N-CNTs, the superior electrocatalytic performance of the vertically aligned N-CNTs is attributed to their large surface area with all of the nanotube top-ends falling on one plane at the interface between the aligned nanotube and electrolyte solution that facilitates the electrolyte/reactant diffusion. The as-prepared N-CNTs also show lower overpotential, smaller crossover effect, and better long-term operation stability. Quantum mechanics calculations with B3LYP hybrid density functional suggest that carbon atoms adjacent to nitrogen dopants possess a substantially higher positive charge density to counterbalance the strong electronic affinity of the nitrogen atom (**Fig. 4C**). A redox

cycling process reduces the carbon atoms that naturally exist in an oxidized form by the action of the electrochemical cycling, followed by reoxidation of the reduced carbon atoms to their preferred oxidized state upon O_2 absorption. The nitrogen-induced charge delocalization can also change the chemisorption mode of O_2 from the usual end-on adsorption (Pauling model) at the CNTs surface (top, **Fig. 4D**) to a side-on adsorption (Yeager model) onto the N-CNTs (bottom, **Fig. 4D**). The parallel diatomic adsorption can effectively weaken the O-O bonding to facilitate ORR at the N-CNTs. It should be noted that herein the N-CNTs were produced by the pyrolysis of iron(II) phthalocyanine[237] with the residual Fe NPs.[95, 105, 107] Although great care was taken during the electrochemical purification of N-CNTs before the ORR tests, the possible effects of metal contaminates on ORR remains a matter of controversy.[238-241] In this regard, it will be a significant advancement to develop a metal-free growth process to produce N-CNTs in order to confirm that the electroactivity of N-CNTs for ORR was indeed caused by the induction of nitrogen sites rather than the iron residue. In order to mitigate

this issue, a combination of plasma-etching with chemical vapor deposition (CVD) technology was used to generate N-CNTs by the use of SiO_2 NPs as metal-free electrocatalysts (**Fig. 5A**).[104] The ORR results suggest that the onset potential for the N-CNTs shifts to a more positive value than that of CNTs (**Fig. 5B**), consistent with the previous report on vertically aligned N-CNTs produced by the metal-catalytic growth.[107] The electron transfer number *per* oxygen molecule on the N-CNTs is 3.52-3.92 at the potential ranging from -0.1 V to 0.2 V (*vs.* Ag/AgCl, **Fig. 5C**), suggesting a four-electron process for ORR at the N-CNTs electrode. Owing to the metal-free growth, the observed electrocatalytic activity toward ORR for the newly produced N-CNTs could be exclusively attributed to the incorporation of nitrogen in the CNTs structure. This provides a solid evidence that nitrogen doping is able to dramatically enhance electrocatalytic activity of CNTs for ORR,[107] by creating the net positive charge on adjacent carbon atoms in the nanotube structure to readily attract the electrons from the anode for facilitating the ORR.
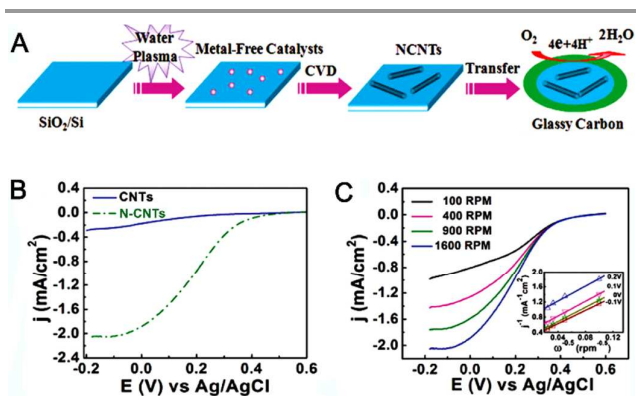

Fig. 5 (A) Metal-free growth of N-CNTs for ORR. (B) LSV curves of the N-CNTs and CNTs in O_2-saturated 0.5 M H_2SO_4 at a scan rate of 10 mV s^{-1}. (C) LSV curves of the N-CNT in O_2-saturated 0.5 M H_2SO_4 at different rotating rates of 100, 400, 900, and 1600 rpm at a scan rate of 10 mV s^{-1} The inset in Fig. 5C shows the Koutecky-Levich plots of the N-CNTs derived from LSV curves. (Adapted with permission from Ref [104] Copyright 2010 American Chemical Society.)

Different single heteroatom (such as boron[102] or sulfur[96])-doped CNTs were also explored as the metal-free electrocatalysts for ORR.[96, 102] **(i) Boron-doped carbon nanotubes (B-CNTs).** B-CNTs with tunable boron content of 0.86, 1.33, and 2.24 at.% (denoted as B1-CNTs, B2-CNTs, and B3-CNTs) were produced using CVD technology with benzene and triphenylborane as precursors and ferrocene as catalyst.[102] X-ray photoelectron spectroscopy (XPS) results show a rich collection of boron chemical states in B-CNTs, including BC_3, BCO_2, and BC_2O moieties. The resulting B-CNTs show the interesting boron content-dependent ORR activity with B3-CNTs exhibiting the biggest peak current density (8.0 mA mg^{-1}) and most positive peak position at -0.35 V *vs.* saturated calomel electrode (SCE) (**Fig. 6A**). Similar trends are also observed for the steady-state diffusion currents and the half-wave potentials in the LSV curves (**Fig. 6B**). Theoretical calculations indicate that the electrocatalytic activity of B-CNTs for ORR stems from conjugation between the vacant $2pz$

orbital of boron and the π orbital of carbon. The accumulated electrons in the $2pz$ orbital are active as a result of the small electronegativity of boron, and therefore become the HOMO electrons in B-CNTs (**Fig. 6C**), suggesting boron doping plays the crucial role in achieving advanced metal-free ORR catalyst. Although the performance of B-CNTs is not yet as good as the commercial Pt/C catalyst (20 wt.% and 40 wt.% Pt loading, **Fig. 6B**), the proportional relationship between ORR performance and boron content suggests the great potential of B-CNTs for further improvement. **(ii) Sulfur doped CNTs (S-CNTs).** S-CNTs are another interesting type of non-Pt catalysts for enhancing ORR. S-CNTs were synthesized by directly annealing oxidized CNTs and benzenedithiol (BDT) under a N_2 atmosphere for ORR in alkaline medium.[96] Experimental results indicate that S-CNTs prepared at 900 ^{o}C using the CNTs/BDT mass ratio of 1:2 exhibit much higher diffusion-limiting current and the more positive onset potential for ORR than those prepared using 1:1 and 1:3 under the same condition. The onset potential of S-CNTs (-0.082 V *vs.* Ag/AgCl) is slightly negative to Pt/C (20 wt.% Pt loading, -0.02 V *vs.* Ag/AgCl), suggesting the excellent ORR electrocatalytic performance of S-CNTs. Similar to the metal-free N-CNTs,[95, 104, 105, 107] B-CNTs and S-CNTs both show smaller crossover effect and better long-term operation stability than the Pt/C catalyst (20 wt.% Pt loading) in alkaline electrolyte.
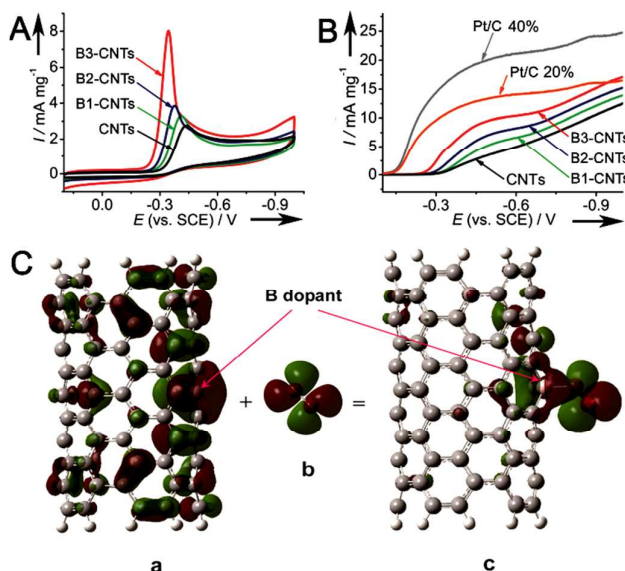

Fig. 6 (A) CV curves of CNTs and different B-CNTs in O_2-saturated 1 M NaOH electrolyte at a scan rate of 50 mV s^{-1}. (B) LSV curves of CNTs, different B-CNTs and commercial Pt/C electrocatalysts in O_2-saturated 1 M NaOH electrolyte at a scan rate of 10 mV s^{-1} and a rotation speed of 2500 rpm. (C) Important molecular orbitals involved in the O_2 adsorption on B-CNTs (5,5). (a) spin-down HOMO-1 of B-CNTs (5,5). (b) LUMO of the triplet O_2. (c) spin-down HOMO-2 of O_2-B-CNTs(5,5). (Adapted with permission from Ref [102] Copyright 2011 Wiley-VCH Verlag GmbH & Co.)

2.2.2 Multiple heteroatoms-co-doped CNTs

Besides the single heteroatom-doped CNTs, multiple heteroatoms (such as boron and nitrogen,[103] phosphorus and nitrogen,[101] sulfur and nitrogen,[97, 242] nitrogen, sulfur and fluorine[98] or silicon and nitrogen[137])-co-doped CNTs exhibit significantly improved ORR due to their synergistic coupling

effect between different heteroatoms that can facilitate the electrocatalytic reduction of oxygen.[10, 11]

Boron and nitrogen co-doped CNTs (BN-CNTs). Vertically aligned CNTs were first used as the advanced carbon nanomaterials support to achieve the co-doping concept for enhancing ORR.[103] By the pyrolysis of melamine diborate, the vertically aligned BN-CNTs with a fairly uniform length of ~15 μm was prepared on SiO_2/Si substrate (**Fig. 7A**). Among the chemically bonded carbon, boron, and nitrogen atoms in vertically aligned BN-CNTs, the carbon content (85.5 %) dominates over boron (4.2 %) and nitrogen (10.3 %). The high carbon content in vertically aligned BN-CNTs ensures high conductivity for electrochemical applications, while the presence of boron and nitrogen can significantly enhance the ORR activity. The LSV curves in **Fig. 7B** show the vertically aligned CNTs support two-step reaction pathway for ORR at around -0.28 and -0.65 V (*vs.* SCE). Vertically aligned B-CNTs shows a similar profile to vertically aligned CNTs, but with an overall better ORR activity (a more positive onset potential and higher current density), which was attributed to the facilitated chemisorption of O_2 by boron doping.[243, 244] For vertically aligned N-CNTs and vertically aligned BN-CNTs, they show a single-step platform, indicating a four-electron ORR process. In particular, the half-wave potential of the vertically aligned BN-CNTs (-0.25 V *vs.* SCE) is much more positive than that of vertically aligned B-CNTs (-0.5 V *vs.* SCE) and vertically aligned N-CNTs (-0.3 V *vs.* SCE). These clearly indicate that boron and nitrogen co-doping significantly improves the electrocatalytic activity of CNTs due to a synergetic effect arising from co-doping of CNTs with both boron and nitrogen atoms. As is known, the nitrogen is an electron-rich dopant (with an electron lone pair) but boron is an electron-deficient one (without electron lone pair). Due to the compensation effect between the electron-rich and electron-deficient dopants, the two cases may exist, which can impact the conjugation system in very different ways: i) boron and nitrogen are bonded together, and ii) boron and nitrogen locate separately, corresponding to totally different electronic structures. Based on this hypothesis, two kinds of boron and nitrogen co-doped CNTs [bonded boron and nitrogen (B-N-CNTs) or separated boron and nitrogen (B-CNTs-N)] were synthesized by different procedures.[99] For B-N-CNTs, the deterioration of ORR performances with increasing B/N ratio indicates that the bonded boron and nitrogen contribute little to the ORR activity (**Fig. 7C**). In contrary, the B-CNTs-N can boost the ORR catalytic ability with increasing B/N ratio (**Fig. 7D**). DFT calculations demonstrate the HOMO plot shows a weak interaction between O_2 and the B-N-CNTs with little charge transferred to O_2, leading to low ORR activity (**Figs. 7E-F**). To further understand such phenomena, the second-order orbital perturbation analysis was applied on both situations. For B-N-CNTs, the lone-pair electrons from nitrogen dopant are largely neutralized by the vacant orbital of boron dopant, and few electrons or vacant orbitals are left to conjugate with the carbon π system. With little conjugation, the activation of carbon π electrons can hardly occur. By contrast, the situation for the B-CNTs-N is totally different. The separation of boron

from nitrogen prevents the neutralization between the electron donor (nitrogen) and acceptor (boron), making CNTs have excellent ORR activity (synergetic effect).
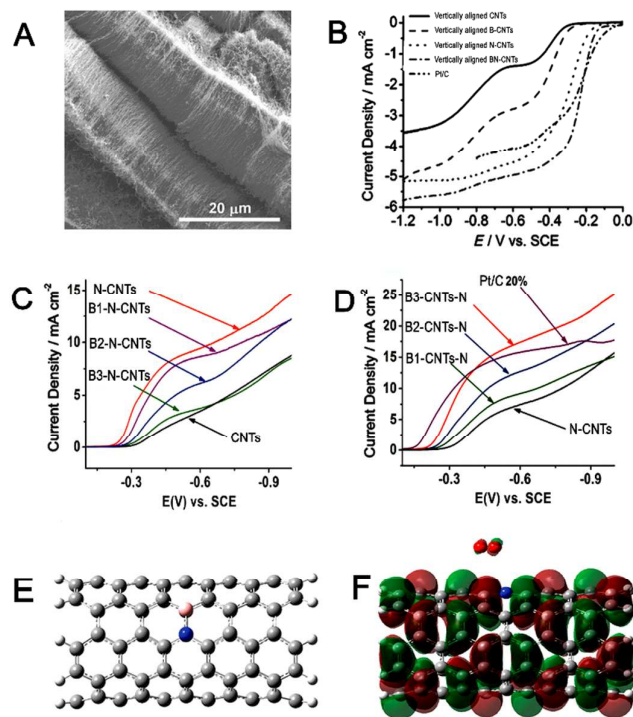

Fig. 7 (A) SEM image of vertically aligned BN-CNTs. (B) LSV curves of various catalysts in O_2-saturated 0.1 M KOH electrolyte at a scan rate of 10 mV s^{-1} and a rotation rate of 1000 rpm. (C) LSV curves of different vertically aligned BN-CNTs and CNTs in O_2-saturated 1 M NaOH electrolyte at a scan rate of 50 mV s^{-1}. The B/N ratio order: B3-N-CNTs > B2-N-CNTs > B1-N-CNTs. (D) LSV curves of N-CNTs, different BN-CNTs and commercial Pt/C electrocatalyst in O_2-saturated 1 M NaOH electrolyte at a scan rate of 10 mV s^{-1} and a rotation speed of 2500 rpm. The B/N ratio order: B3-CNTs-N > B2-CNTs-N > B1-CNTs-N. (E) Bonded B and N co-doped CNTs (5,5). (F) HOMO plot of the corresponding O_2 adsorption configuration (isodensity value of 0.007 au). N, blue; B, pink; C, black; H, gray; O, red. (Parts A-B adapted with permission from Ref [103] Copyright 2011 Wiley-VCH Verlag GmbH & Co. Parts D-F adapted with permission from Ref [99] Copyright 2013 American Chemical Society.)

Followed by B,N co-doping concept for ORR, several groups have tried to co-dope with the combination of various dual elements (*e.g.*, phosphorus and nitrogen,[101] sulfur and nitrogen,[242] and silicon and nitrogen[137]) into CNTs for further optimizing ORR performance. **Phosphorus and nitrogen co-doped CNTs (NP-CNTs).** An injection-assisted CVD method was recently used to make NP-CNTs.[101] Owing to the synergetic effect arising from co-doping CNTs with both phosphorus and nitrogen, the resultant NP-CNTs show a significantly enhanced electrocatalytic activity toward ORR with respect to CNTs doped by phosphorus or nitrogen only. **Sulfur and nitrogen co-doped CNTs (NS-CNTs).** In addition to NP-CNTs, NS-CNTs were synthesized by annealing a mixture of N-CNTs and sulfur.[242] The onset potential of NS-CNTs for ORR is almost the same as that of Pt/C catalyst (20 wt.% Pt loading), and more positive than that of N-CNTs in alkaline medium, suggesting that NS-CNTs exhibit excellent performance in alkaline medium, which is due to the co-doping of sulfur and nitrogen has changed the

chemical environment, making the graphitic nitrogen species more preferable for ORR. The NS-CNTs with enhanced ORR performance can also be made by ball-milling CNTs with thiourea, followed by thermal treatment.[97] Such incorporation of sulfur and nitrogen took place in defect sites of CNTs. When the graphitic structure of CNTs collapses, the amount of nitrogen actually incorporated into the C-C network can be increased by co-doping with sulfur. The ORR activity of NS-CNTs increases with the increasing content of heteroatoms, both in acid and alkaline media. As a consequence, co-doping with nitrogen and sulfur results in more active electrocatalyst for ORR in acid media as sulfur promotes the incorporation of surface nitrogen. **Silicon and nitrogen co-doped CNTs (NSi-CNTs).** Co-doping concept has also been well demonstrated on NSi-CNTs for promoting ORR. With the help of CVD technology, NSi-CNTs were synthesized by Liu, Peng and co-workers (**Fig. 8A**).[137] In alkaline media, the onset potential of NSi-CNTs (-0.02 V vs. Ag/AgCl) is slightly lower than that of commercial Pt/C catalyst, 47.6 wt.% Pt loading, (-0.001 V *vs.* Ag/AgCl) (**Fig. 8B**). Theoretical calculations indicate that compared to single heteroatom-doped or un-doped counterparts, silicon and nitrogen co-doping changes the O_2 chemisorption mode from the usual end-on adsorption to a relatively easy side on adsorption onto material surface, making the electrons considerably easy to be excited and transferred to O_2, (**Figs. 8C-8F**). **Nitrogen, sulfur and fluorine co-doped CNTs (FNS-CNTs).** In addition to dual doping onto CNTs, more recently, the research interest has moved to dope three kinds of elements (*i.e.*, nitrogen, sulfur and fluorine) into CNTs surface for further optimizing ORR, by first the adsorption of heteroatoms-containing ionic liquids on the walls of CNTs, followed by carbonization (**Fig. 9A**).[98] The resultant FNS-CNTs display one of the best performances among heteroatom-doped nanocarbon electrocatalysts in terms of half-wave potential and kinetic current density. The four-electron selectivity and the exchange current density of the FNS-CNTs are comparable to those of the Pt/C electrocatalyst (20 wt.% Pt loading). Furthermore, an alkaline fuel cell that employs FNS-CNTs as the cathode electrocatalyst shows very high current and power densities (**Fig. 9B**).

2.3 Heteroatom-Doped 2D Graphene (GN)

GN is a 2D monolayer of carbon atoms parked into a dense hexagonal network structure,[245] and can be considered as the basic building block for graphitic materials of all dimensions because it can be wrapped up into 0D C_{60}, rolled into 1D CNTs, or stacked into 3D graphite.[192, 220] Since the substance was first isolated in 2004,[245] GN has been attracting considerable attention owing to its fascinating physical and chemical properties and the explosive interests from experimentalists and theoreticians.[246, 247] GN exhibits remarkable electronic, optical, thermal and mechanical properties.[192, 248-253] These attractive properties generate huge interest to explore the potential applications of biomedicine,[254, 255] reinforced composites,[256] electronics and transparent electrodes for displays, solar cells,[257-260] and especially metal-free ORR catalysts.[8, 42, 55-58, 168-173, 176]
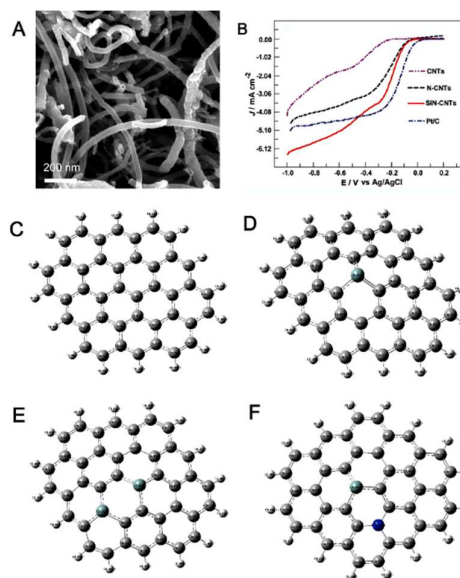

Fig. 8 (A) SEM image of SiN-CNTs. (B) LSV curves of CNTs, N-CNTs, SiN-CNTs and Pt/C in O_2-saturated 0.1 M KOH solution. The net charge distributions of C, Si and N atoms in pure GN (C), Si-doped GN with one silicon (D) or two silicon atoms (E) and Si, N-co-doped GN (F). (Adapted with permission from Ref [137] Copyright 2015 Royal Chemical Society.)
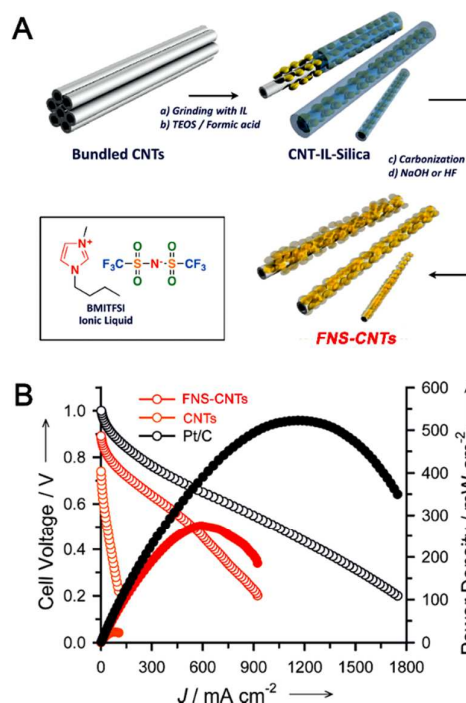

Fig. 9 (A) Synthesis of the FNS-CNTs. (B) The performance of MEAs that employ FNS-CNTs, CNTs, or Pt/C as the cathodes in alkaline fuel cells at 50 ^{o}C; open and closed circles correspond to the cell voltages and power densities, respectively. (Adapted with permission from Ref [98] Copyright 2014 Wiley-VCH Verlag GmbH & Co.)

2.3.1 Single heteroatom-doped GN

Nitrogen-doped GN (N-GN). In 2010, the first example on the use of N-GN as metal-free electrocatalysts for ORR was demonstrated by Liu, Dai and co-workers.[133] In this work, the

N-GN was synthesized by CVD of methane in the presence of ammonia. The resultant N-GN film can be readily etched off from the substrate by dissolving the residual Ni electrocatalyst layer in HCl,[261] allowing the freestanding N-GN sheets to be transferred onto different substrates suitable for subsequent electrochemical investigation (**Fig. 10A**). The catalytic current density at the N-GN is found to be ~3 times higher than that of the Pt/C (20 wt.% Pt loading) over a large potential range in air-saturated 0.1 M KOH solution (**Fig. 10B**). The electron transfer number *per* oxygen molecule at N-GN electrode is 3.6-4 at the potential ranging from -0.4 to -0.8 V (*vs.* Ag/AgCl). Later, with the help of nanocasting technology, the N-GN sheets with the size between 200 nm to several micrometers and the thickness of ~18 nm were obtained.[130] This material exhibits a one step, four-electron transfer pathway with a high kinetic current density of 7.3 mA cm^{-2}, which is superior to that of the Pt/C catalyst with 20 wt.% Pt loading (5.4 mA cm^{-2}). Further studies reveal that both the electrical conductivity and the content of pyridinic nitrogen are two vital factors for achieving high-performance nitrogen-doped carbon nanomaterials for ORR as they have a huge impact on the electron transfer to electrodes and oxygen reduction at active sites. More recently, the N-GN sheets, derived from polyacrylonitrile brush[118] with high nitrogen doping content of up to 11.2 wt.% and high specific surface area of up to 217 m^2 g^{-1} show the four-electron transfer mechanism for ORR with higher kinetic limiting current and diffusion limiting current density than the commercially available Pt/C electrocatalyst (20 wt.% Pt loading) in alkaline medium. A more interesting N-GN with size-defined mesopores (**Fig. 10C**) was recently synthesized by employing a GN/silica nanosheet template.[114] The N-GN sheets with the nitrogen doping content of 3.5% have a lot of 22 nm mesopores on their surface, providing much more active sites for boosting ORR. The ORR results show that the N-GN sheets with mesopores exhibit a diffusion-limiting current approaching that of Pt/C (20 wt.% Pt loading, 5.45 *vs.* 5.78 mA cm^{-2}), and even a more positive onset and half-wave potential [-0.01 and -0.11 V *vs.* reversible hydrogen electrode (RHE)] than those of Pt/C in alkaline medium (**Fig. 10D**). Around the same time, an eco-friendly method based on silica-protected pyrolysis process was developed to prepare N-GN sheets with binary mesopores at 2.1 and 7.5 nm, allowing to facilitate O$_2$ and electrolyte diffusion onto the catalyst surface.[119] The onset potential of ORR at GN commences around -0.22 V (*vs.* Ag/AgCl), whereas the onset potential at N-GN sheets with binary mesopores shifts positively to -0.13 V with the limiting diffusion current density at -0.70 V being ~1.5 times larger than that of GN. **N-GN quantum dots.** Besides the mesoporous N-GN, N-GN quantum dots are also very promising for ORR. The synthesis of N-GN quantum dots with the nitrogen/carbon atomic ratio of 4.28% has been demonstrated through the electrochemical etching of filtration-formed GN film in acetonitrile containing nitrogen-containing tetrabutylammonium perchlorate (TBAP).[205] The diameter of the N-GN quantum dots is ~2-5 nm (**Fig. 10E**). The GN was further employed to support N-GN quantum dots for promoting ORR. In alkaline solution, the ORR onset potential of

N-GN quantum dots supported on GN was at ~-0.16 V (*vs.* Ag/AgCl) with a reduction peak at ~-0.27 V (**Fig. 10F**), which is close to those of the Pt/C electrocatalyst, indicating an optimized catalytic ability of N-GN quantum dots for ORR. Later, by the hydrothermal treatment of willow leaves, the N-GN quantum dots with the height of ~1-4 nm and the nitrogen/carbon atomic ratio of 4.28% were synthesized.[262] Though such N-GN quantum dots exhibit more negative onset and half-wave potentials (-0.002 and -0.244 V *vs.* Hg/HgO) than those of Pt/C, 20 wt.% Pt loading (0.07 and -0.129 V) in alkaline medium, it still shows a four-electron process for ORR over a wide potential range. Recent studies try to understand the effect of the size of N-GN quantum dots on ORR performance, showing that the N-GN quantum dots with the smaller size led to a more negative onset potential and a lower ORR current.[128] This can be explained by the smaller-size N-GN quantum dots have the elevated HOMO level, which makes the electrons harder to be excited and transfer to O$_2$, hence hinders the ORR.
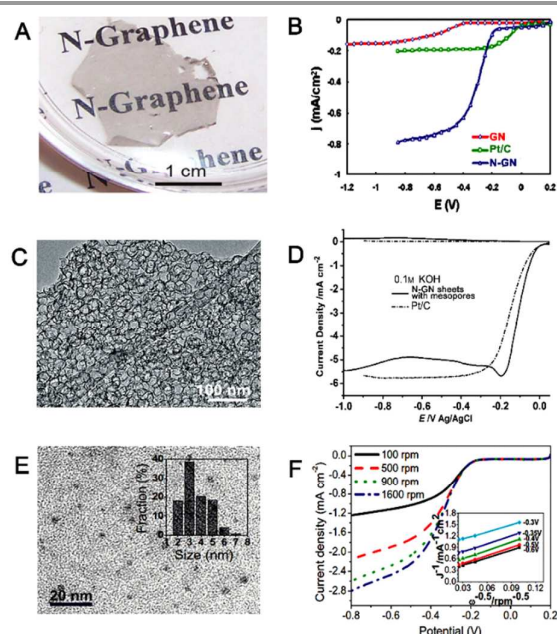

Fig. 10 (A) A digital photo image of a transparent N-GN film floating on water. (B) LSV curves of GN (red line), Pt/C (green line), and N-GN (blue line) in air-saturated 0.1 M KOH. Electrode rotating rate: 1000 rpm. Scan rate: 0.01 V s^{-1}. Mass$_{(GN)}$ = Mass$_{(Pt/C)}$ = Mass$_{(N-GN)}$ = 7.5 μg. (C) TEM image of N-GN with mesopores. (D) LSV curves of N-GN with mesopores and Pt/C in O$_2$-saturated 0.1 M KOH at a scan rate of 10 mV s^{-1} with the rotation rate of 1600 rpm. (E) TEM image of N-GNQDs. (F) LSV curves of N-GN quantum dots in O$_2$-saturated 0.1 M KOH with different speeds. The *inset* shows the Koutecky-Levich plots derived from the LSV measurements. (Parts A-B adapted with permission from Ref [133] Copyright 2010 American Chemical Society. Parts A-D adapted with permission from Ref [114] Copyright 2014 Wiley-VCH Verlag GmbH & Co. Parts E-F adapted with permission from Ref [205] Copyright 2012 American Chemical Society.)

Besides the N-GN, different single heteroatom (such as sulfur,[109, 120, 123, 124] iodine,[121, 122] chlorine[121] or bromine[121])-doped GN were also found to be good candidates as the effective metal-free electrocatalysts for ORR. **Sulfur doped GN (S-GN).** The edge-selectively S-GN sheets were first synthesized by a simple *yet* efficient dry ball-milling graphite in

the presence of sulfur.[120] The limiting current density for ORR of edge-selectively S-GN sheets (4.47 mA cm^{-2}) approaches 93.4% (4.79 mA cm^{-2}) of commercial Pt/C (20 wt.% Pt loading) in O_2-saturated 0.1 M KOH solution (**Fig. 11A**). The first-principle study by DFT methods on the electronic structure of edge-selectively S-GN sheets suggest that the catalytic activity of the doped GN is closely related to spin and charge distributions on the graphitic framework. Sulfur, covalently bound to the zigzag and armchair edges of GN, can induce both charge and spin densities on the GN. As a result, those carbon atoms with high positive charge and spin densities can serve as active sites for promoting the catalytic activity. Furthermore, the sulfur atom itself is also an active site for ORR, since the charge density of sulfur at the zigzag edge is increased as high as 0.22 (circle in **Fig. 11B**). Furthermore, the study of the HOMO and the LUMO distributions on GN suggests that the HOMO and LUMO are strongly polarized by the covalently bonded sulfur atoms at the edge of GN (**Fig. 11C**). These polarized zones should serve as the active sites for ORR. Besides the ball-milling method,[120] several other approaches were also reported for S-GN synthesis. The prominent examples include the successful fabrication of S-GN with sulfur content of 1.53% by directly annealing GO and benzyl disulfide in argon,[123] the synthesis of S-GN with high surface area *via* the thermal reaction between GO and the H_2S guest gas at high temperature,[124] the use of a green and cost-effective method for preparing S-GN achieved by the continuous charge/discharge cycling of GN-sulfur composites in lithium-sulfur batteries,[109] the synthesis of crumpled and sheet-like S-GN *via* magnesiothermic reduction based on the low-cost, nontoxic CO_2 and Na_2SO_4 as the carbon and sulfur sources, respectively. All the above S-GNs show enhanced ORR activity with nearly four-electron transfer pathway. **Iodine, chlorine or bromine-doped GN (I-GN, Cl-GN or Br-GN).** In addition, I-GN, Cl-GN or Br-GN sheets were also explored as effective electrocatalysts for ORR, showing that they can be doped into GN nanosheets by a special designed method. The obtained I-GN, Cl-GN or Br-GN nanosheets shows the remarkable electrocatalytic activities toward ORR in alkaline medium.[121] First-principle density-functional calculations reveal that the edges of halogenated GN have favorable binding affinity with oxygen molecule, and the O-O bond strengths are weakened as a result of the halogenation-induced charge transfer (**Figs. 11D-E**), being in good agreement with the experimental observations.[122] **Boron, phosphorous or oxygen-doped GN (B-GN, P-GN or O-GN).** By combining the experimental data and DFT calculations, Qiao and co-workers systematically investigated the nature and origin of ORR activity of a series of heteroatom (N, B, P, O or S)-doped GN catalysts.[263] The results predict that the electrocatalytic ORR performance of an ideal heteroatom-doped GN possesses the exchange current density of 2.1 × 10 µA cm^{-2}, onset potential of 0.33 V (*vs.* normal hydrogen electrode, NHE) and an almost 100% 4-electron pathway selectivity, which are comparable with or even better than those of the state-of-the-art Pt catalyst. These combined computational and experimental studies reveal the nature of

ORR electrocatalysis for GN-based materials, paving the new way to the molecular design of highly efficient GN-based metal-free catalysts with their ORR performance surpassing that of the state-of-the-art Pt catalyst.
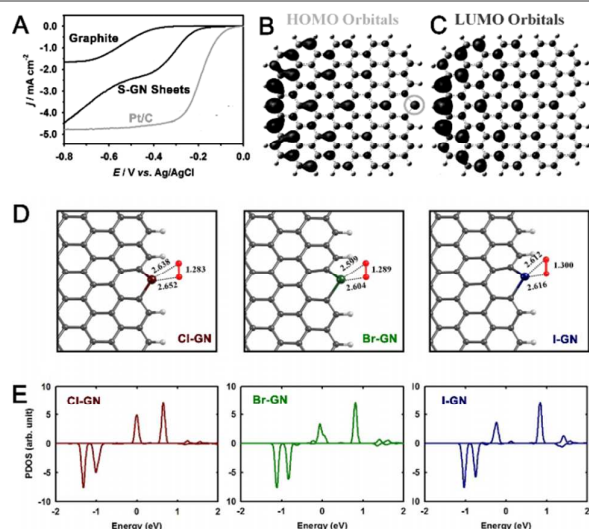

Fig. 11 (A) LSV curves of the graphite, S-GN and Pt/C electrodes in O_2-saturated 0.1 M KOH solution at a scan rate of 10 mV s^{-1} and a rotation rate of 1600 rpm. (B) HOMO distribution of S-GN. (C) LUMO distribution of S-GN. (D) The optimized O_2 adsorption geometries onto Cl-GN, Br-GN and I-GN, in which halogen is covalently linked to two sp^2 carbons. (E) The projected density of electronic states onto O_2: (d) Cl-GN; (e) Br-GN; (f) I-GN for the cases of corresponding (a), (b), and (c), respectively. (Parts A-C adapted with permission from Ref [120] Copyright 2013 Wiley-VCH Verlag GmbH & Co. Parts D-E adapted with permission from Ref [121] Copyright 2013 Nature Publishing Group.)

2.3.2 Multiple heteroatoms-co-doped GN

Co-doping of two different elements into GN is one of the unique approaches to achieve the effective earth-abundant materials for ORR. **Sulfur and nitrogen co-doped GN (NS-GN).** NS-GN was synthesized by annealing a mixture of GO and poly[3-amino-5-mercapto-1,2,4-triazole] composite.[116] Due to the synergistic effect between sulfur and nitrogen, the half-wave potential of NS-GN is comparable to that of Pt/C (20 wt.% Pt loading), and the limiting current density of NS-GN sheets even surpasses that of Pt/C (20 wt.% Pt loading) at -0.28 V (*vs.* SCE) in alkaline solution. The electron-transfer number for NS-GN sheets is close to 3.6 at the potentials ranging from -0.5 to -0.7 V (*vs.* SCE), suggesting that the ORR process mainly proceeds *via* a four-electron pathway. With a similar annealing method but changing the sulfur precursor to dipyrrolemethane[108] or ethylene glycol[112], NS-GNs can be also prepared and exhibit a remarkable electrocatalytic activity towards the ORR, further supporting the conclusion that co-doping of sulfur and nitrogen can make ORR catalysts more effective.[108, 112] This co-doping concept has been extended to other two multielement-doped GN for highly efficient non-noble metal catalysts for ORR. **Boron and nitrogen co-doped GN (BN-GN).** For example, BN-GN has been prepared by simple thermal annealing of GO in the presence of boric acid and ammonia for producing the efficient ORR electrocatalyst.[126] The half-wave potential of BN-GN sheets ($B_{12}C_{77}N_{11}$ in the work) for ORR is at ~-0.25 V (*vs.* SCE) in 0.1 M

KOH solution, which is close to that of the Pt/C (20 wt.% Pt loading, **Fig. 12A**). The first-principle calculations were performed to better understand the origin of high catalytic capability of BN-GN (**Fig. 12B**). As is known, a small HOMO-LUMO gap implies the low kinetic stability and high chemical reactivity because the smaller energy gap means that the state of the GN is energetically favorable to add electrons to a high-lying LUMO and to extract electrons from a low-lying HOMO, and thus the facile formation of activated complexes for any potential reaction.[264] Compared to pure GN, the substitution of carbon by boron and nitrogen leads to a smaller HOMO-LUMO energy gap. However, overdoping of B and N can lead to a significant increase in the HOMO-LUMO energy gap. As a result, $B_{38}C_{28}N_{34}H_{26}$ has the highest HOMO-LUMO energy gap.[126, 265] Recently, more efforts have been invested to design more complex BN-GN sheets with mesopores for providing more active sites to boost ORR.[113] One interesting example is that the mesoporous BN-GN was made by annealing the GO-based polyaniline nanosheets functionalized with boronic acid followed by CO_2 activation. Benefiting from their high surface area (363 m^2 g^{-1}), unique 2D structure, and high heteroatoms-doping contents (5.4wt.% boron and 5.3wt.% nitrogen), the mesoporous BN-GN exhibits excellent ORR activity in alkaline

media with a half-wave potential (-0.27 V *vs.* Ag/AgCl), close to that of Pt/C, 20 wt.% Pt loading (-0.18 V *vs.* Ag/AgCl). BN-GN quantum dots also exhibit great potential in enhancing ORR due to their nanoscaled size compared to BN-GN as well as the synergetic effect between boron and nitrogen. In order to demonstrate this concept, NS-GN quantum dots were prepared with an electrochemical etching method[111] and the combustion flame technique,[110] respectively. As expected, these two kinds of NS-GN quantum dots show high catalytic activities for the ORR in alkaline medium. **Phosphorous, sulfur and nitrogen co-doped GN (NPS-GN).** Recently, NPS-GN, prepared by employing thiourea as a single source of nitrogen and sulfur, and triphenylphosphine as phosphorous precursors, has been considered to be a more effective system for further boosting ORR.[115] Additional phosphorous doping causes a remarkable synergistic effect on binary NS-GN sheets by generating active phosphorous-nitrogen species. The optimized NPS-GN exhibits excellent ORR activity, which is ~2 times better than that of binary NS-GN sheets, and ~5 times better than that of single phosphorous-doped GN sheets. The catalytic activity of the ternary-doped GN sheets is superior than the Pt/C catalyst (20 wt.% Pt loading) in alkaline medium.
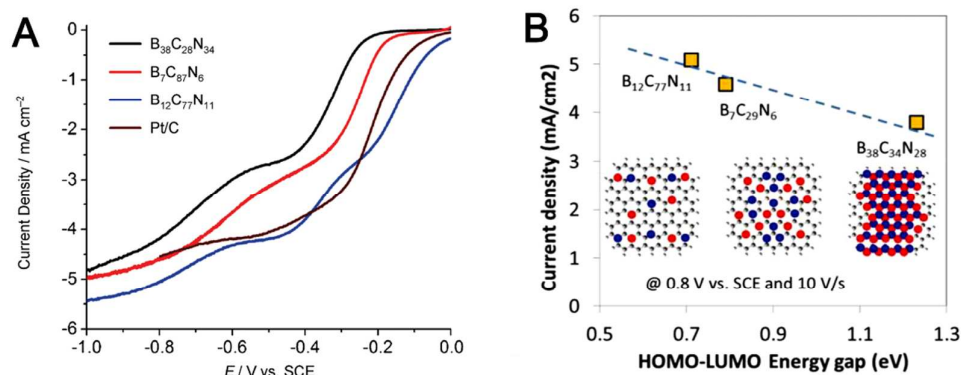

Fig. 12 (A) LSV curves of BN-GN with different compositions and Pt/C catalyst in O_2-saturated 0.1 M KOH solution. (B) Experiment ORR activities *vs.* DFT-predicated HOMO-LUMO energy gap for BN-GN. (Adapted with permission from Ref [126] Copyright 2012 Wiley-VCH Verlag GmbH & Co.)

2.4 Heteroatom-Doped 3D Carbon Nanomaterials

Till now, various heteroatom-doped 3D carbon nanomaterials were reported for the effective oxygen reduction.[8, 42, 55-58, 93, 134-173, 176, 194-196, 206, 207, 209, 212, 214] To clarify the information and make this section easy to follow and understand, **Table 1** summarizes the related heteroatom-doped 3D carbon nanomaterials for ORR, which are discussed in this section below.

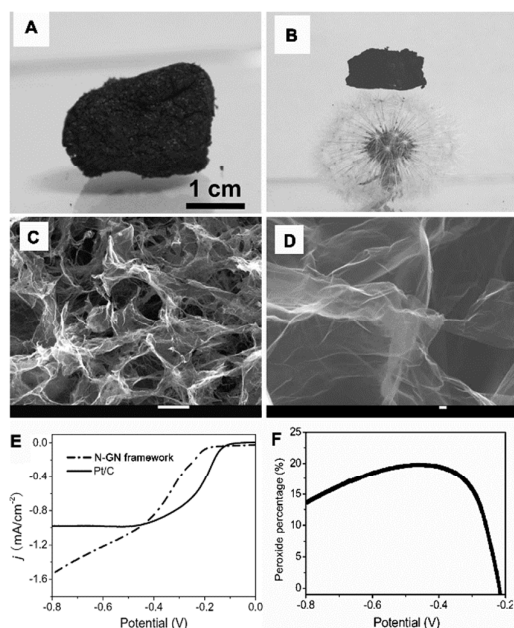### 2.4.1 Single heteroatom-doped 3D carbon nanomaterials

2.4.1.1 N-GN-based 3D nanomaterials

There are several different designs on N-GN-based 3D nanomaterials for promoting ORR. **(i) N-GN framework.** A versatile, ultralight 3D N-GN framework has recently made for enhancing ORR because it has the obvious merits in fire resistance, ultra-low density (~2.1 mg cm^{-3}) as well as the unique 3D pore-rich structure with maximum access to the nitrogen sites within highly exposed GN (**Figs. 13A-D**).[160] In 0.1

M KOH solution, the onset potential for ORR on GN framework (~-0.18 V *vs.* Ag/AgCl) is slightly lower than that on the Pt/C catalyst with 20 wt.% Pt loading (**Fig. 13E**). The electron-transferred number *per* oxygen molecule involved in ORR is determined to be ~3.7, indicating the ORR proceeds *via* a nearly four-electron pathway. In addition, the peroxide yield on GN framework is less than 20 % in all the potential range and decreases to 13 % at -0.8 V (**Fig. 13F**). These results indicate that the N-GN framework is indeed a promising metal-free electrocatalyst for ORR in an alkaline solution. **(ii) Nanoporous N-GN.** A nanoporous Ni-based CVD method to synthesize free-standing 3D nanoporous N-GN sheets with tunable pore sizes (**Fig. 14A**).[151] The optimized 3D nanoporous N-GN sheets show the onset potential of ~-0.08 V (*vs.* Ag/AgCl) and the kinetic current density of 8.2 mA cm^{-2} at -0.40 V (*vs.* Ag/AgCl) (higher than that of Pt/C, 5.4 mA cm^{-2} under the same potential) in alkaline media (**Figs. 14B-C**). Such excellent electrochemical activity for ORR is attributed to the unique

physicochemical properties of free-standing 3D nanoporous N-GN sheets including the high electrical conductivity of GN and the 3D nanostructure fully exploiting the intrinsic large effective surface area for high catalytic efficiency made by the open porosity. **(iii) Mesoporous N-GN.** In 2014, a mesoporous N-GN was successfully prepared by directly annealing the pre-synthesized GO-polydopamine.[117] The content of carbon, nitrogen, and oxygen in the obtained N-GN sheets is 88.8%, 3.2% and 8.0%, respectively. The resulting mesoporous N-GN shows the onset potential of -0.06 V (*vs.* Hg/Hg$_2$Cl$_2$) *vs.* -0.20 V at GN for ORR, which is closer to that of the commercial Pt/C with unmentioned wt.% Pt loading (0.10 V). **(iv) N-GN/N-CNTs composite.** A facile solution self-assembly method was demonstrated to 3D N-GN/N-CNTs composite by heating the mixture of GN, CNTs and melamine (as a nitrogen-rich source) at 900 °C under an Ar atmosphere.[145] SEM and TEM images indicate that CNTs and GN sheets combine together and they are well linked together. By taking advantage of the abundant highly active sites from N-GN and the 3D conductive network from N-CNTs for efficient mass and electron transport, the N-GN/N-CNTs composite in alkaline medium demonstrates their potential as low-cost efficient ORR electrocatalyst. **(v) N-GN foams.** 3D porous N-GN foams were prepared by using silica spheres as hard temperature.[166] With a 3D macroporous morphology and high surface area for both enhanced electrolyte-electrode interactions and electrolyte-reactant diffusion, the 3D porous N-GN foams exhibit both remarkable ORR activity and long-term stability in both alkaline and acidic solutions, and their ORR activity is even better than that of the Pt-based electrocatalyst in alkaline medium


Fig. 13 (A and B) Photographs of the as-prepared superlight N-GN framework, and one with a piece of N-GN framework size of 1.8 cm x 1.1 cm x 1.2 cm standing on a dandelion. (C and D) SEM images of N-GN framework. Scale bars: (C) 10 mm, (D) 100 nm. (E) LSV curves of N-GN framework and Pt/C in O$_2$-saturated 0.1 M KOH solution. (F) The curve of peroxide yield on the N-GN framework electrode. (Adapted with permission from Ref [160] Copyright 2012 Wiley-VCH Verlag GmbH & Co.)

Nitrogen-doped 3D porous carbons. (i) Nitrogen-doped 3D ordered mesoporous carbons (N-OMCs). N-OMCs were first fabricated on the basis of a metal-free nanocasting technology with SBA-15 as the template and N,N'-bis(2,6-diisopropyphenyl)-3,4,9,10-perylenetetracarboxylic diimide as the source of both carbon and nitrogen.[167] Being similar with the ordered mesoporous carbons (OMCs), the N-OMCs with N doping amount of 2.7% exhibit the 2D hexagonal arrangements as well as the high BET surface area (510 cm^2 g^{-1}) and total pore volume (0.61 cm^3 g^{-1}). The onset potential of N-OMCs for ORR in alkaline medium is -0.13 V (*vs.* Ag/AgCl), which is nearly the same with that of the commercial Pt/C catalyst (20 wt.% Pt loading). The calculated kinetic current density of N-OMCs at 0.35 V (9.15 mA cm^{-2}) is more than twice as high as that of commercially Pt/C catalyst with 20 wt.% Pt loading (4.44 mA cm^{-2} at 0.35 V). These suggest the superior ORR activity of N-OMCs. Later, another novel N-OMCs with both higher surface areas (up to 1500 m^2 g^{-1}) and higher nitrogen content (12 wt.%) were synthesized for further enhancing ORR by the use of ionic liquids and nucleobases as the source of carbon and nitrogen.[165] The onset potential for ORR on the N-OMCs is 0.035 mV (*vs.* Ag/AgCl) in alkaline medium, corresponding to an overpotential ~0.025 V higher than the commercial Pt/C catalyst (20 wt.% Pt loading). In acid electrolyte, N-OMCs exhibit an onset potential at 0.573 V (*vs.* Ag/AgCl) and an overpotential of 0.197 V as compared with Pt/C catalyst (20 wt.% Pt loading). Recently, to improve the ORR activity of nitrogen-doped carbon-based semiconductor (*i.e.*, graphitic-C$_3$N$_4$, g-C$_3$N$_4$), an electron-conductive material of OMCs was applied as a support for the g-C$_3$N$_4$ catalyst.[164] Compared with mesoporous g-C$_3$N$_4$ and the mixed g-C$_3$N$_4$+OMCs, the obtained composite of g-C$_3$N$_4$@OMCs exhibit the enhanced electron transfer efficiency with lower onset potential and higher ORR current density (**Fig. 15A**). To better understand the effect of OMCs on the ORR activity of g-C$_3$N$_4$@OMCs, the first-principle calculations were applied. As shown in **Fig. 15B(a)**, the free energy plots of ORR and optimized configurations of adsorbed species on the g-C$_3$N$_4$ surface with zero, two, and four-electron participation are demonstrated as paths I, II, and III. The free energy of each proposed ORR state, including the initial reactant O$_2$ adsorbed g-C$_3$N$_4$ (O$_2$@g-C$_3$N$_4$), intermediate product OOH$^-$ on g-C$_3$N$_4$ (OOH@g-C$_3$N$_4$), and final product OH$^-$ in the solution with pristine g-C$_3$N$_4$ (OH$^-$/g-C$_3$N$_4$). As illustrated in path I, oxygen cannot be reduced spontaneously on the pristine g-C$_3$N$_4$ surface without the electron participation (**Fig. 15B(b)**) due to the existence of two insurmountable barriers in the free energy plot at the states of intermediate and final products. Since g-C$_3$N$_4$ is a semiconductor, as illustrated in **Fig. 15B(c)**, the active sites facilitating ORR on g-C$_3$N$_4$ are limited to very narrow zones of the electrode-electrolyte-gas three-phase boundaries. One effective way to increase the number of electrons accumulated on the g-C$_3$N$_4$ surface is adding an electron-conductive material as a support for the g-C$_3$N$_4$. Predictably, as shown in **Fig. 15B(d)**, the active sites facilitating ORR on g-C$_3$N$_4$ with a conductive support can spread over the whole surface of the electrocatalyst due to the increased

electron transfer efficiency in the composite, which in turn facilitates an efficient four-electron transfer process for ORR. Therefore, the ORR active sites on g-C3N4 with a conductive support (*e.g.*, OMCs) can spread over the whole surface of the catalyst due to the increased electron transfer efficiency in the composite, which in turn facilitates an efficient four-electron pathway. **(ii) Nitrogen-doped 3D mesoporous carbon cubes (N-mesoporous carbon cubes).** 3D hollow-structured N-mesoporous carbon cubes were first synthesized through a magnesium thermal reduction approach in CO_2.[143] One important feature of N-mesoporous carbons cubes for ORR is economical and applicable to large-scale synthesis. Although the onset potential of N-mesoporous carbon cubes was lower than that of the commercial Pt/C (20 wt.% Pt loading) in 0.1 M KOH solution, they encouragingly show the comparable limit current density with the Pt/C catalyst (20 wt.% Pt loading). **(iii) Nitrogen-doped 3D nanoporous carbons (N-nanoporous carbons).** A new type of 3D N-doped nanoporous carbon was made by a hydrothermal treatment of plant *Typha orientalis* at 180 ^{o}C for 12 h, followed by annealing them in NH_3 atmosphere at 800 ^{o}C.[157] Due to their high BET surface area (898 m^2 g^{-1}), abundant pores, high content of nitrogen atom

(9.1 at.%), and 3D interpenetrated network structure, the N-nanoporous carbon exhibits similar catalytic activity for ORR as compared to the commercial Pt/C (20 wt.% Pt loading) catalyst in alkaline media, and show excellent catalytic ability in acidic media. **(iv) Nitrogen-doped 3D hierarchically porous carbons (N-hierarchically porous carbons).** By using polydopamine (PDA)-modified mixed cellulose ester filter film as a sole template, N-hierarchically porous carbon with hierarchical micro-, meso-, and macroporosity in one structure was constructed.[153] Such unique structure leads to a super-high surface area of 2191 cm^2 g^{-1}. After being further stimulated by KOH activation, the N-hierarchically porous carbon shows a nearly equal ORR activity to the Pt/C catalysts (20 wt.% Pt loading) in alkaline solution. The ORR catalytic activity of N-hierarchically porous carbons is among the highest reported activities of metal-free nitrogen-doped carbon nanoelectrocatalysts. **(v) Other N-porous carbons based nanomaterials.** Following different protocols, various 3D porous nitrogen-doped carbons with their unique physicochemical properties were also synthesized, all of which show the outstanding activities for ORR in alkaline medium.[138, 141, 148]

Table 1 Summary of heteroatom-doped 3D carbon nanomaterials reported for ORR

Element			Nanomaterial	Reference
Single heteroatom-doped	N-doped	N-GN-based nanomaterials	N-GN framework	160
			Nanoporous N-GN	151
			Mesoporous N-GN	117
			N-GN/N-CNTs composite	145
			N-GN foams	166
		Nitrogen-doped porous carbons	N-OMCs	167
			N-mesoporous carbon cubes	143
			N-nanoporous carbons	157
			N-hierarchically porous carbons	153
			Other N-porous carbons based nanomaterials	138, 141, 148
		Other kinds of nitrogen-doped carbon nanomaterials	N-carbon nanofibers aerogel	266
			N-carbon capsules	159
			N-carbon nanocages	163
			N-carbon nanospheres	154
			N-carbon nanoleaf networks	142
	Other single element-doped		P-OMCs	161
			Se-GN/Se-CNTs networks	162
Multiple heteroatoms-co-doped	N and S co-doped	N and S co-doped porous carbons-based nanomaterials	NS-porous carbons	155
			NS-trimodal porous carbons	149
			NS-mesoporous carbons	140
			Mesoporous NS-GN	127
			NS-GN sheets-mesoporous carbon composite	147
			NS-GN nanomesh foams	144
	N and P co-doped		NP-mesoporous carbons foams	135
			P-carbon nitride-carbon fibers papers	136
	N, S and O co-doped		NOS-OMCs	156
			NPS-porous carbons	150
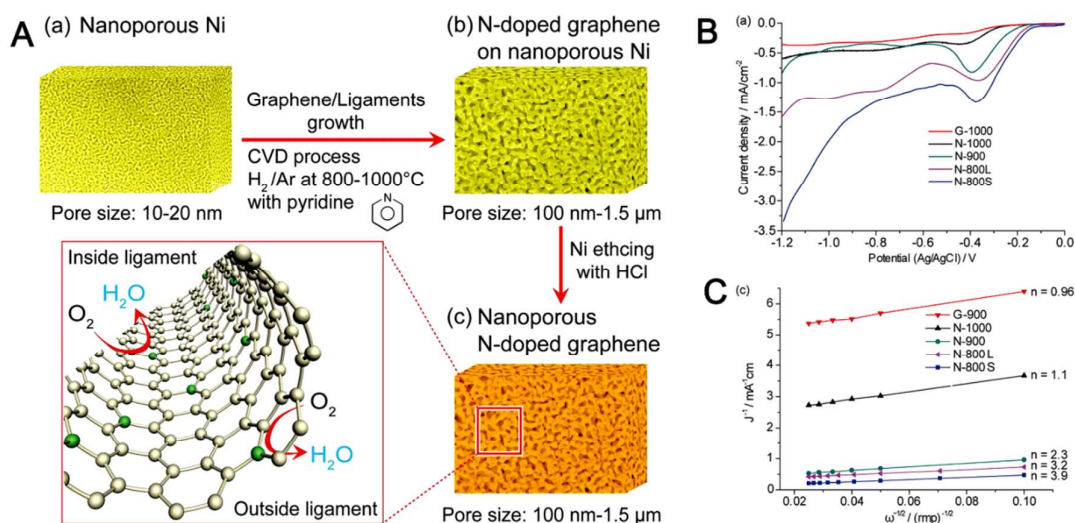
Fig. 14 (A) Schematic illustration of the preparation process of 3D nanoporous N-GN (a-c); and the ORR catalyzed by 3D nanoporous N-GN. (B) LSV curves of 3D nanoporous N-GN grown at different CVD temperatures and un-doped nanoporous GN. G-1000: 3D un-doped nanoporous GN deposited at 1000 °C; N-1000: 3D nanoporous N-GN deposited at 1000 °C; N-900: 3D nanoporous N-GN deposited at 900 °C; N-800L: 3D nanoporous N-GN deposited at 800 °C for longer time; N-800S: 3D nanoporous N-GN deposited at 800 °C for shorter time. (C) Koutecky-Levich plots at -0.40 V with the electron transport number (*n*) *per* oxygen molecule. (Adapted with permission from Ref [151] Copyright 2014 Wiley-VCH Verlag GmbH & Co.)
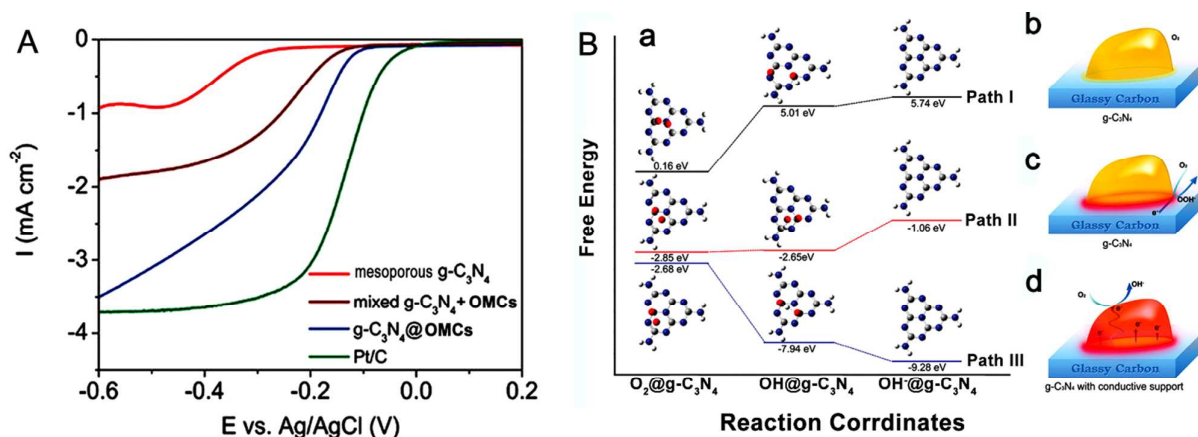
Fig. 15 (A) LSV curves of various electrocatalysts at 1500 rpm in O_2-saturated 0.1 M KOH solution. (B) (a) Free energy plots of ORR and optimized configurations of adsorbed species on the g-C_3N_4 surface with zero, two, and four electron participation demonstrated as paths I, II, and III. Energy levels are not drawn to scale. Gray, blue, red, and white small spheres represent C, N, O, and H, respectively. (b-d) Schemes of ORR's pathway on pristine g-C_3N_4 without electron participation, pristine g-C_3N_4 with two-electron participation, and g-C_3N_4/conductive support composite with 4e$^-$ participation, respectively (red areas represent the active sites facilitating ORR). (Adapted with permission from Ref [165] Copyright 2011 American Chemical Society.)

2.4.1.2 Other kinds of nitrogen-doped 3D carbon nanomaterials

In addition to N-GN-based 3D nanomaterials and nitrogen-doped 3D porous carbons discussed above, different types of nitrogen-doped 3D carbon nanomaterials also show superior ORR activity. **(i) Nitrogen-doped 3D carbon nanofibers aerogel (N-carbon nanofibers aerogel).** A highly active 3D N-carbon nanofibers aerogel, prepared by direct pyrolysis of a mass-producible biomass of bacterial cellulose, and followed by NH_3 activation, was first used as an advanced metal-free electrocatalyst for ORR.[266] The prepared N-carbon fiber aerogel exhibits the high density of N-containing active sites of 5.8 at.% and high BET surface area of 916 m^2 g^{-1}, resulting in

the excellent ORR activity (half-wave potential of 0.80 V *vs.* RHE), and excellent electrochemical stability (only 20 mV negative shift of half-wave potential after 10000 potential cycles) in alkaline media. Importantly, when used as a cathode electrocatalyst of Zn-air battery, the N-carbon fibers aerogel exhibits high voltages of 1.34 and 1.25 V at the discharge current densities of 1.0 and 10 mA cm^{-2}, respectively, which are highly comparable with the state-of-the art Pt/C electrocatalyst (20 wt.% Pt loading), indicating the great potential of this metal-free electrocatalyst as a promising alternative to the Pt/C (20 wt.% Pt loading) for alkaline fuel cells and metal-air batteries. However, due to the very low amount of nitrogen in the raw material of bacterial cellulose,

additional ammonia gas annealing step is required to introduce more nitrogen into the material in order to realize the excellent ORR performance. To simplify the synthesis process, the prawn shells with high nitrogen content were applied as the raw material instead of bacterial cellulose to produce the N-carbon nanofiber aerogel.[139] By this way, only one-step pyrolysis of carbonization is required to get the 3D N-carbon fibers aerogel. Such 3D N-carbon fibers aerogel exhibits high N doping level of 5.9%, and high surface area of 526 m^2 g^{-1}. As an electrocatalyst, the resultant 3D N-carbon fibers aerogel exhibits superior electrocatalytic activity towards ORR with a more positive ORR onset potential, better stability and high resistance to crossover effect compared to the commercial Pt/C (unmentioned wt.% Pt loading). **(ii) Nitrogen-doped 3D carbon capsules (N-carbon capsules). Combining the** solvothermal reaction with the carbonization was used to make the N-carbon capsules with nitrogen content (~13 at.%) and high BET surface area of ~595 m^2 g^{-1} using melamine and glyoxal as precursors.[159] In alkaline medium, the electron-transfer number *per* oxygen molecule of ORR at the applied potential between -0.50 and -0.80 V (vs. Ag/AgCl) on N-carbon capsules is 3.7, indicating a predominant oxygen reduction process of four-electron pathway. Specially, the measured H_2O_2 yield for highly N-carbon capsules was below 16%, similar to that of the commercial Pt/C (12 wt.% Pt loading), indicating the electron-transfer number of ~4 as well. Such excellent ORR activity can be due to the large surface area and the high-level nitrogen doping of N-carbon capsules. Later the same group reported another kind of N-carbon capsules with bamboo-like CNTs whiskers.[152] Due to the combined the advantageous features of high surface area of 985 m^2 g^{-1}, abundant active sites (from the structural defects of the pore edges and bamboo-shaped CNTs and nitrogen doping) and easy access to medium and favorable mass transport, N-carbon capsules exhibit the same onset potential as that of the Pt/C (20 wt.% Pt loading), but higher reaction current density in O_2-saturated 0.1 M KOH solution. **(iii) Nitrogen-doped 3D carbon nanocages (N-carbon nanocages).** By the use of an *in-situ* generated MgO template method and pyridine as the precursor, N-carbon nanocages with high specific surface area of 1393 m^{-2} g^{-1} and high nitrogen content (~10%) were produced.[163] In O_2-saturated 0.1 M KOH electrolyte, the electron-transfer number *per* oxygen molecule (3.27 at -0.5 V *vs.* Ag/AgCl) and the onset potential (-0.13 V) of N-CNs for ORR are comparable to the Pt/C electrocatalyst, 20 wt.% Pt loading, (3.92 at -0.5 V *vs.* Ag/AgCl and -0.03 V) but the diffusion-limiting current of N-carbon nanocages is higher than that of Pt/C electrocatalyst (20 wt.% Pt loading)**. (iv) Nitrogen-doped 3D carbon nanospheres (N-carbon nanospheres).** Using the fermented rice as the raw resource, a green approach was developed to synthesize N-carbon nanospheres,[154] which have very high specific surface areas of 2105.9 m^2 g^{-1}, high porosity of 1.14 cm^3 g^{-1} and higher nitrogen content of 6.2 at.%. Although the onset potential of N-carbon nanospheres (-0.06 V *vs.* Hg/HgO) is slightly lower than that of Pt/C (20 wt.% Pt loading), its onset potential is positively shifted compared with that of the directly carbonized products of unfermented rice and

fermented rice. In addition, N-carbon nanospheres exhibit the four-electron process for ORR with long-term stability and excellent resistance to crossover effects and CO poisoning. **(v) Nitrogen-doped 3D carbon nanoleaf networks (N-carbon nanoleaf networks).** A simple method was used to construct N-carbon nanoleaf networks by using CNTs as a single precursor.[142] The resultant N-carbon nanoleaf networks can act as ORR electrocatalysts with superb electrocatalytic activity. The excellent ORR activity is attributed to the synergistic effect of the N-doped, nanoporous structure, structural integrity, high surface area (380-497 m^2 g^{-1}) and good conductivity (up to 112 S m^{-1}), originating from the unique bridged structure of the CNTs and graphene nanoribbons (GNRs), ensuring the rapid electron transfer and mass.
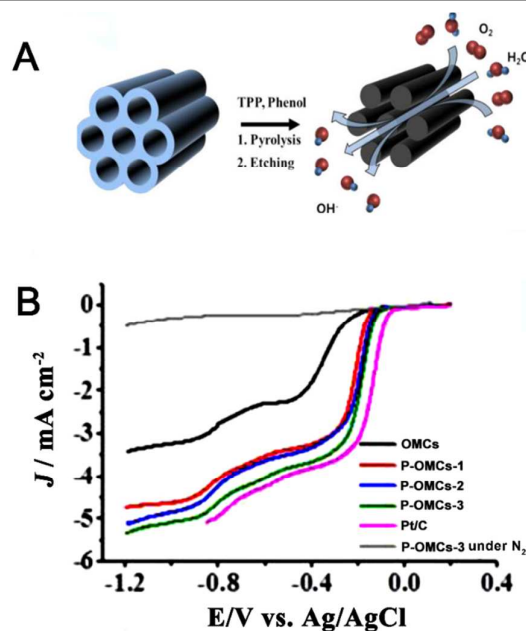

Fig. 16 (A) Schematic illustration on the preparation of P-OMCs. (B) LSV curves for OMCs, P-OMCs-1 (P-OMCs with the length of 1.5 μm and the thickness of 0.2 μm), P-OMCs-2 (P-OMCs with the length of 1.0 μm and the thickness of 0.4 μm), P-OMCs-3 (P-OMCs with the length of 0.7 μm and the thickness of 0.6 μm) and Pt/C on a glassy carbon rotating disk electrode in O_2-saturated 0.1 M KOH solution at a scan rate of 10 mV s^{-1}. LSV curve for P-OMCs-3 on a glassy carbon rotating disk electrode in N_2-saturated 0.1 M KOH solution at a scan rate of 10 mV s^{-1}. (Adapted with permission from Ref [161] Copyright 2012 American Chemical Society.)

Other important elements have also been explored to dope 3D carbon nanomaterials for ORR. **Selenium-doped 3D CNTs-GN networks (Se-GN/Se-CNTs networks).** One interesting example is Se-GN/Se-CNTs networks by directly annealing CNTs, GN and diphenyl diselenide in Ar.[162] The obtained Se-GN/Se-CNTs exhibit slightly negative onset potential and higher current density (at -0.9 V *vs.* Ag/AgCl) compared with the Pt/C electrocatalyst (47.6 wt.% Pt loading), suggesting that doping Se into 3D carbon nanomaterials can provide a good opportunity for boosting ORR. This is because that selenium has an evidently larger atomic size than carbon, the introduction of selenium atoms into carbon materials may

cause higher strain at their edges, thus facilitating charge localization and associated chemisorption of oxygen. **Phosphorus-doped 3D OMCs (P-OMCs).** In 2012, P-OMCs with different lengths were synthesized using a metal-free nanocasting method of SBA-15 mesoporous silica as template and triphenylphosphine and phenol as phosphorus and carbon sources, respectively (**Fig. 16A**).[161] Experimental results indicate the P-OMCs with shorter length (0.7 μm) exhibit higher ORR performance compared to those of longer channels (1.0 and 1.5 μm) in alkaline medium, which is likely because O_2 molecules have less resistance in shorter channels. The onset potential and the limiting current at P-OMCs with the channel length of 0.7 μm are both comparable with those at Pt/C (20 wt.% Pt loading) in O_2-saturated 0.1M KOH solution (**Fig. 16B**). Later, on the basis of the principle that P-OMCs with short mesochannels can greatly improve the ORR activity mentioned above,[161] the same concept was further extended to fabricate a kind of thin disk-type or plate-type P-OMCs with shorter mesochannels for ORR,[146] which outperforms P-OMCs with the channel length of 0.7 μm.[161]
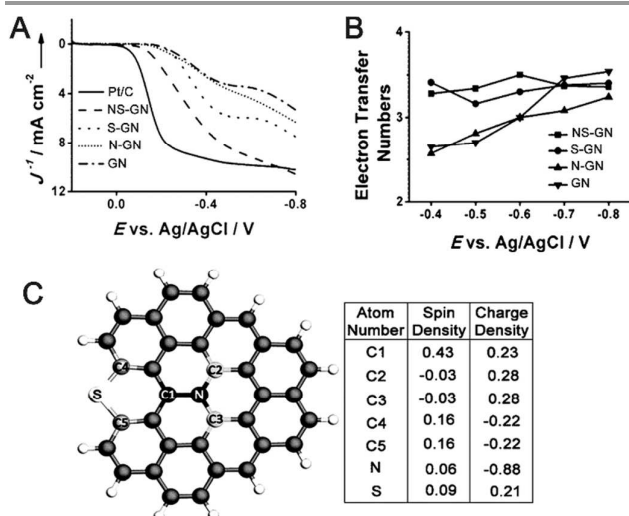

Fig. 17 (A) LSV curves of mesoporous NS-GN, mesoporous S-GN, mesoporous N-GN, mesoporous GN and Pt/C at 1600 rpm. (B) Electron-transfer numbers as a function of the overpotential of different samples. (C) Spin and charge density of GN network dual-doped by N and S. C1 has very high spin density, C2 and C3 have high positive charge density, and C4 and C5 have moderately high positive spin densities. (Adapted with permission from Ref [127] Copyright 2012 Wiley-VCH Verlag GmbH & Co.)

2.4.2 Multiple heteroatoms-co-doped 3D carbon nanomaterials

2.4.2.1 Nitrogen and sulfur co-doped 3D porous carbons-based nanomaterials.

(i) Hierarchical nitrogen and sulfur co-doped porous carbons (NS-porous carbons). A green approach was used to prepare NS-porous carbon with hierarchical-porous structure and high surface area by using organic ionic liquid as nitrogen, sulfur and carbon sources and the eutectic salt as template.[155] The onset potential for optimized NS-porous carbon is close to that of the Pt/C electrocatalyst (20 wt.% Pt loading), but its current density is higher than that of the Pt/C electrocatalyst (20 wt.% Pt loading). The DFT calculations reveal that the dual doping of nitrogen and sulfur atoms lead to the redistribution of spin and

charge densities, which may be responsible for the formation of a large number of carbon atom active sites. **(ii) NS-trimodal porous carbons.** A self-sponsored co-doping approach to facilely control the doping of nitrogen and sulfur into graphitic carbon network structure has been recently demonstrated,[149] in which the required carbon and dopant (nitrogen and sulfur) sources are self-sponsored by a sole precursor (1-allyl-2-thiourea) without the need for the catalysts. The optimized NS-porous carbons with the large BET surface area of 572 m^2 g^{-1} and trimodal pore (*i.e.*, microporous, mesoporous and macroporous) structure possesses an onset potential of -0.035 V for ORR, almost identical to that of commercial Pt/C (unmentioned wt.% Pt loading). The excellent ORR activity of NS-porous carbons can be attributed to the synergistic effect caused by sulfur, nitrogen heteroatoms doping as well as the presence of macropores in the trimodal-porous network. **(iii) Nitrogen and sulfur co-doped 3D mesoporous carbons (NS-mesoporous carbons).** By using honeysuckles as the single precursor, an economic strategy has been explored for the preparation of NS-mesoporous carbon with the specific surface area of 802.8 m^2 g^{-1}, the mesopore size of ~4.1 nm, and the nitrogen and sulfur contents of 1.95 at.% and 0.75 at.%.[140] In alkaline medium, the onset potential of NS-mesoporous carbon for ORR is 0.046 V (*vs.* Hg/HgO), similar to that of Pt/C (20 wt.% Pt loading). The electron transfer number *per* oxygen molecule of NS-MCs at -0.3 V (*vs.* Hg/HgO) is 3.60, demonstrating that the ORR proceeds on NS-mesoporous carbons *via* a four-electron pathway. **(iv) Mesoporous NS-GN.** In 2012, a one-step doping/annealing process was designed to prepare the mesoporous NS-GN with benzyl disulfide and melamine as sulfur and nitrogen precursors, respectively.[127] The thickness of the NS-GN sheets is 1-1.5 nm, indicating 3-6 carbon atomic layers. The mesoporous size of NS-GN is 10-40 nm. The NS-GN displays a very high ORR onset potential of -0.06 V (*vs.* Ag/AgCl), close to that of commercial Pt/C, 20 wt. % Pt loading (-0.03 V *vs.* Ag/AgCl) and much more positive than those of N-GN, S-GN, or GN (~-0.18 V *vs.* Ag/AgCl) in alkaline medium (**Fig. 17A**). Also, the electron-transfer number *per* oxygen molecule is between 3.3 and 3.6 over the potential range from -0.4 to -0.8 V (*vs.* Ag/AgCl, **Fig. 17B**), suggesting a four-electron process for ORR. These indicate that this material has clearly better catalytic performance, which further supports the proposed synergistic effect caused by dual sulfur and nitrogen doping. The DFT calculations reveal that the synergistic performance enhancement results from the redistribution of spin and charge densities brought about by the dual doping of sulfur and nitrogen atoms (**Fig. 17C**). **(v) Nitrogen and sulfur co-doped 3D graphene sheets-mesoporous carbon (NS-GN sheets-mesoporous carbon) composite.** NS-mesoporous carbons-GN sheets with the BET surface area of 281 m^2 g^{-1} were synthesized by using nano-casting technology with mesoporous silica/GN nanosheets as hard templates, and cystine as heteroatom and carbon precursors.[147] Though the ORR activity of NS-GN-mesoporous carbons composite in alkaline medium is not as good as the Pt/C (20 wt.% Pt loading), it shows the outstanding long-term stability, superior to the Pt/C electrocatalyst. **(vi) Nitrogen**

and sulfur co-doped GN nanomesh foams (NS-GN nanomesh foams). A kind of 3D NS-GN nanomesh foams, composed of GN sheets with in-plane nanopores, was synthesized by Zhao *et al.*.[144] With hierarchical pore arrangement, favorable mass transport and the richly available GN edges, the 3D NS-GN nanomesh foams exhibit a comparable onset potential of ~0.04 V (*vs.* Ag/AgCl) but higher limiting current for ORR in alkaline medium compared to the Pt/C catalyst (20 wt.% Pt loading, ~ 0.05 V *vs.* Ag/AgCl).
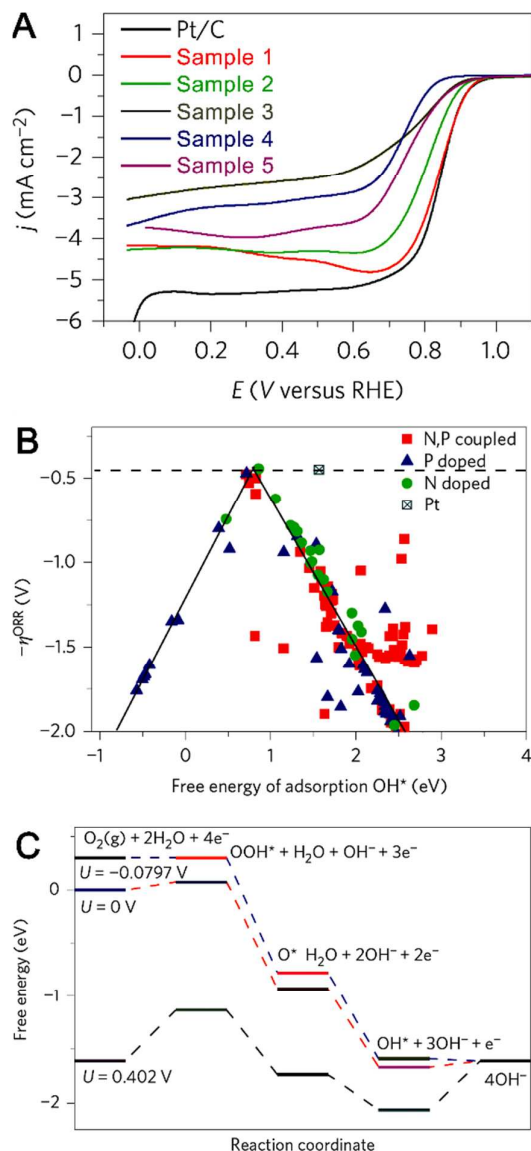
Fig. 18 (A) LSV curves for NP-mesoporous carbons foams synthesized under different conditions and Pt/C in O_2-saturated 0.1 M KOH solution at the scan rate of 5 mV s^{-1} and the rotating rate of 1,600 rpm. Sample 1: NP-mesoporous carbons foams heated at 1000 ^{o}C; Sample 2: NP-mesoporous carbons foams heated at 1100 ^{o}C; Sample 3: NP-mesoporous carbons foams heated at 900 ^{o}C; Sample 4: NP-carbons heated at 1000 ^{o}C; Sample 5: N-porous carbon foams heated at 900 ^{o}C. (B) ORR volcano plots of overpotential (η) versus adsorption energy of O* and the difference between the adsorption energy of O* and OH*, respectively, for N-doped, P-doped and N,P-co-doped GN. (C) Schematic energy profiles for the ORR pathway on N,P co-doped GN in

alkaline media. (Adapted with permission from Ref [135] Copyright 2015 Nature Publishing Group.)

2.4.2.2 Nitrogen and phosphorus co-doped NP-mesoporous carbons foams (NP-mesoporous carbons foams).

In another case, nitrogen and phosphorus co-doped 3D foams have been designed to enhance ORR. 3D NP-mesoporous carbons foams with the large surface area of 1548 m^2 g^{-1} was made by simply pyrolysing polyaniline aerogels obtained from a template-free polymerization of aniline in the presence of phytic acid.[135] As shown in **Fig. 18A**, a reduction potential similar to that of the commercial Pt/C catalyst (20 wt.% Pt loading) was observed at the optimized NP-mesoporous carbons foams for ORR in alkaline medium, suggesting their high electrocatalytic activity. Furthermore, the onset potential of 0.94 V (*vs.* RHE), the half-wave potential of 0.85 V (*vs.* RHE) and the limiting current of NP-mesoporous carbons foams are comparable to those of Pt/C (20 wt.% Pt loading). Theoretical calculations indicate that in alkaline media, the calculated activation energy for the rate-limiting step of the Langmuir–Hinshelwood mechanism is ~0.5 eV for NP-GN, which is lower than those of N-GN (~0.56-0.62 eV) and Pt(111) surface (0.55 eV) (**Figs. 18C-D**). Thus, the 3D NP-MCs foams possess ORR activities comparable to, or even better than that of Pt in alkaline media. **Phosphorus-doped graphitic carbon nitride on 3D carbon fibers papers (P-carbon nitride-carbon fibers papers).** Recently, one interesting 3D nanostructure of P-carbon nitride consisting of thin nanosheets directly grown on carbon fibers papers exhibits high activity and stability in ORR.[136] The P-carbon nitride-carbon fibers papers affords an onset potential of 0.94 V (*vs.* RHE) and a half-wave potential of 0.67 V (*vs.* RHE) for ORR in alkaline medium, which are close to those of Pt on carbon fibers papers (the onset potential of 0.99 V *vs.* RHE and the half-wave potential of 0.80 V *vs.* RHE), and better than those observed for the phosphorus-free counterpart P-carbon nitride-carbon fibers papers (the onset potential of 0.90 V *vs.* RHE and the half-wave potential of 0.63 V *vs.* RHE). Furthermore, the P-carbon nitride on CFPs exhibits a Tafel slope value of 122.3 mV decade^{-1} in ORR region, much lower than that of P-carbon nitride-carbon fibers papers (135.7 mV decade^{-1}), suggesting its favorable reaction kinetics.

**2.4.2.3 Nitrogen, sulfur and oxygen co-doped 3D ordered mesoporous carbons (NOS-OMCs).**

NOS-OMCs with hexagonal mesostructures were prepared *via* a nanocasting method using SBA-15 mesoporous silica as a template and glucosamine, p-toluenesulfonic acid, and sucrose as sources of carbon as well as dopants.[156] The triple-doped NOS-OMCs electrocatalyst displays the best ORR activity compared to the dual-doped (NO-OMCs and OS-OMCs) and monodoped O-OMCs in acidic medium. Interestingly, the work functions of these heteroatom-doped OMCs, measured by Kelvin probe force microscopy, display a strong correlation with the activity and reaction kinetics for the ORR. **Nitrogen, phosphorus, and sulfur co-doped 3D porous carbons (NPS-porous carbons).** 3D NPS-porous carbons were synthesized using metal-organic frameworks as a template and dicyandiamide, triarylphosphine and dimethyl sulfoxide as

nitrogen, phosphorus, and sulfur precursors.[150] The electron-transfer number *per* oxygen is 3.5-3.9 from -0.4 to -0.9 V (vs. Ag/AgCl) in alkaline medium, suggesting a favorable four-electron pathway of the ORR. The kinetic limiting current density of NPS-porous carbons at -0.6 V (*vs.* Ag/AgCl) is up to ~11.6 mA cm^2, which is 1.2 times higher than that of the Pt/C catalyst (20 wt.% Pt loading). The excellent electrocatalytic activity of NPS-porous carbons should be attributed to the three reasons below. (i) Due to the different electronegativities between the doped heteroatoms (*e.g.*, N: 3.04, P: 2.19, S: 2.58) and the carbon atoms (C: 2.55), the electroneutrality of the doped carbon framework is broken to explore a higher number of active sites, facilitating the adsorption of O_2 and significantly enhancing the rate of the overall ORR process. (ii) The changed asymmetric spin density of heteroatoms in NPS-porous carbons can effectively weak the O-O bonding to provide more active sites and enhance the ORR activity of carbon materials. (iii) The pore structures of NPS-porous carbons are changed owing to the heteroatoms doping. The product with different active sites and increasing

percentage of mesopores has remarkable influences on the ORR activity.

3. Engineering Noble-Metal-Free Transition Metal-based NPs/Carbon Nanomaterials Composites for ORR

Besides the heteroatom-doped carbon nanomaterials, advanced carbon nanomaterials functionalized with transition metal-based NPs is another kind of interesting noble-metal-free electrocatalysts displaying high ORR activities.[77, 78, 81-87, 89-92] By introducing carbon nanomaterials with different dimensions into transition metal-based NPs, the functionalization of transition metal-based NPs on carbon nanomaterials exhibits higher ORR activity and stability compared to their unsupported counterparts. The interesting and powerful synergetic effect between the carbon nanomaterials with large surface area/stable structure and the transition metal-based NPs with high ORR electrocatalytic activities can be the main reason, leading to the superior electrocatalytic performance for ORR.[77, 78, 81-87, 89-92, 174, 175]
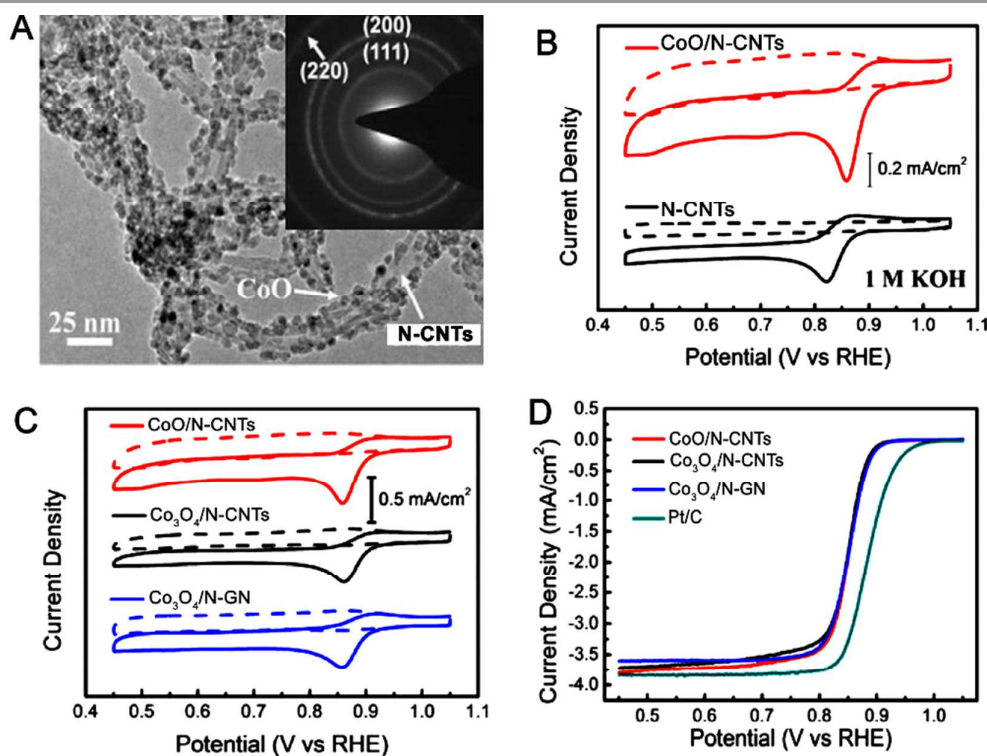
Fig. 19 (A) TEM image of the CoO/N-CNTs hybrid. *Inset* shows an electron diffraction pattern of the hybrid. The inside circle corresponds to graphite (002) from CNTs. (B) CVs of CoO/N-CNTs and N-CNTs in O_2-saturated (solid line) or N_2-saturated (dash line) 1 M KOH. (C) CV curves of different materials in O_2-saturated (solid line) or N_2-saturated (dash line) 1 M KOH. (D) ORR polarization curves of CoO/N-CNTs, Co_3O_4/N-CNTs, Co_3O_4/N-GN and Pt/C in O_2-saturated (solid line) or N_2-saturated (dash line) 1 M KOH at a sweep rate of 5 mV s^{-1} and rotation rate of 1600 rpm. (Adapted with permission from Ref [82] Copyright 2012 Nature Publishing Group.)

3.1 Transition Metal-Based NPs on 1D Carbon Nanomaterials

Cobalt(II) oxide NPs on 1D N-CNTs (CoO/N-CNTs). A two-step method combining the direct growth of nanocrystals on CNTs and the gas-phase annealing in a NH3 atmosphere has been

used to prepare 5 nm CoO/N-CNTs hybrids (Fig. 19A).[82] Herein, cobalt oxide was in the form of CoO due to thermal annealing in the reducing NH3 environment, confirmed by X-ray diffraction (XRD). The amount of CoO and nitrogen in CoO/N-CNTs is ~67wt.% by thermogravimetric analysis (TGA) and

~2.5at.% by XPS, respectively. The CoO/N-CNTs hybrid shows an ORR onset potential of 0.93 V (vs. RHE) and a peak potential of 0.86 V (vs. RHE) in 1 M KOH, much more positive than those of the pure N-CNTs (**Fig. 19B**). Both the ORR onset and the peak potentials of CoO/N-CNTs hybrid are similar to those of the hydrothermally derived Co_3O_4/N-CNTs and Co_3O_4/N-GN hybrids (**Fig. 19C**). Rotating disk electrode measurements indicate that CoO/N-CNTs, Co_3O_4-N-CNTs and Co_3O_4-N-GN hybrids exhibit very similar LSV curves with similar half-wave potential, about 35 mV more negative than Pt/C electrocatalyst (20 wt.% Pt loading, **Fig. 19D**). These indicate that these materials contain similar active sites in nature for ORR. However, the CoO/N-CNTs hybrid affords higher peak current density by ~30% than the other two hybrids in CV curves, suggesting that the CoO/N-CNTs hybrid contains a larger number of effective or accessible ORR active sites. The average electron transfer number *per* oxygen molecule is ~3.9 for CoO/N-CNTs. The hydrothermally synthesized Co_3O_4/N-CNTs hybrid shows an ORR activity similar to that of the CoO/N-CNTs hybrid, suggesting both of these hybrids favor a four-electron reduction pathway for ORR. **Manganese-cobalt oxide on 1D N-CNTs ($MnCo_2O_4$/N-CNTs).** A simple and scalable method was used for the synthesis of spinel $MnCo_2O_4$ NPs partially embedded in N-CNTs ($MnCo_2O_4$/N-CNTs, **Fig. 20A**) by oxidative thermal scission.[81] $MnCo_2O_4$/N-CNTs exhibits superior ORR performance to N-CNTs, as indicated by the ORR polarization curves in **Fig. 20B**, a more positive onset potential and higher disk current, lower H_2O_2 yield, and higher electron transfer number *per* oxygen molecule.

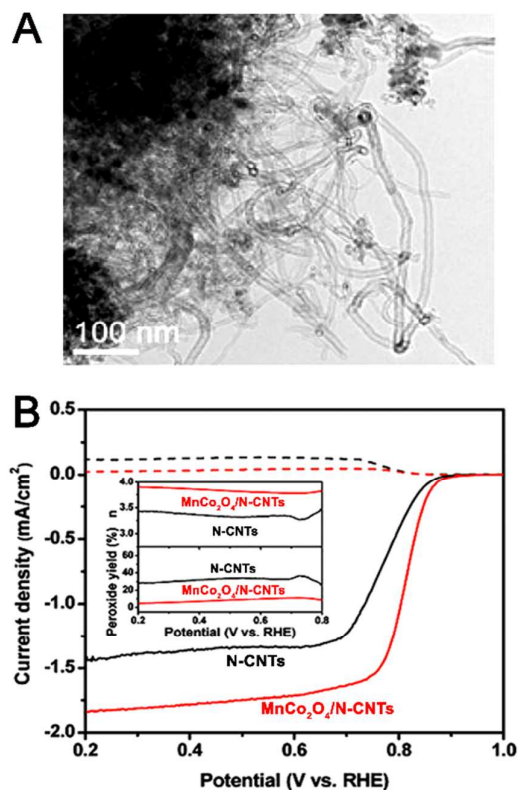**Fig. 20** (A) TEM image of MnCo2O4/N-CNTs. (B) ORR polarization curves of MnCo2O4/N-CNTs and N-CNTs. Inset: peroxide yield and electron transfer number per oxygen molecule at various potentials. (Adapted with permission from Ref [81] Copyright 2014 American Chemical Society.)

3.2 Transition Metal-based NPs on 2D Carbon Nanomaterials

Cobalt-Cobalt(II) Oxide Core-Shell NPs on 2D GN (Co/CoO-GN). In transition metal-based NPs-GN catalyst systems, transition metal-based NPs were often deposited directly onto GN surfaces through *in situ* chemical depositions.[88, 89, 267] Despite the fact that the depositions led to a tight NPs-GN contact, NPs prepared from these methods lack the desired size and morphology control, thereby making it difficult to tune the GN-metal oxide NPs interaction for better catalyst performance.[87, 88] Recently, Guo *et al.* demonstrated a direct solution-phase-based self-assembly approach based on the sonication of the pre-synthesized Co/CoO NPs hexane with GN DMF solution to deposit preformed monodisperse Co/CoO core/shell NPs on the surface of GN (**Fig. 21A**). The obtained Co/CoO-GN showed much enhanced catalysis for ORR in alkaline medium, thus indicating the interaction between Co/CoO and GN can indeed be tuned to enhance NPs catalysis.[87] Compared to GN and Co/CoO-Ketjen carbons, the Co/CoO-GN shows much enhanced catalytic activity for ORR (**Fig. 21B**). Their ORR activity depends on the CoO thickness with 1 nm CoO shell showing the maximum activity. The work demonstrates the importance of Co/CoO dimension and G as a support in tuning electrocatalysis for efficient ORR. The optimized Co/CoO-GN have a comparative activity and better stability than the commercial Pt/C (20 wt.% Pt loading) and may serve as a promising alternative to Pt/C catalyst (20 wt.% Pt loading) for ORR in alkaline solutions (**Figs. 21C-D**). In addition to transition metal-based NPs-GN, such tune concept can be also realized between metal oxide and other kinds of carbon nanomaterials, which will be discussed in *Section 3.3*.
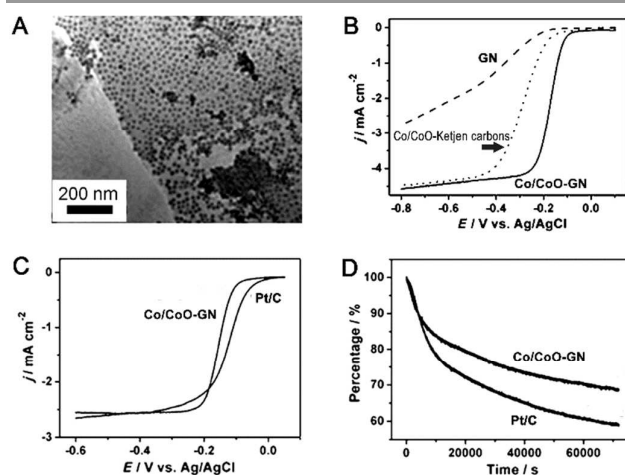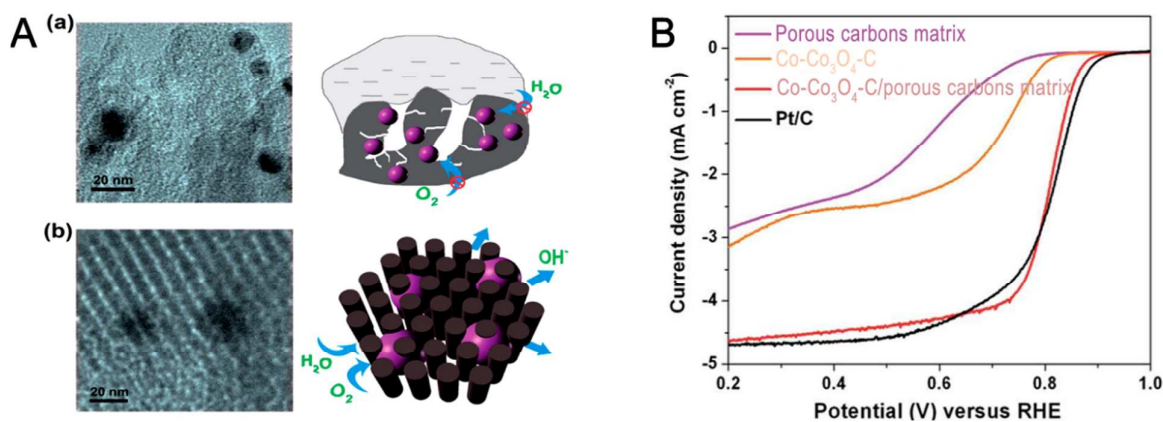

Fig. 21 (A) TEM image of GN-Co/CoO. (B) ORR polarization curves of GN, Co/Co-Ketjen carbons, and Co/Co-GN in O_2-saturated 0.1 M KOH solution at the scan rate of 10 mV s^{-1} and the rotation rate of 1600 rpm. ORR polarization curves of the Co-CoO/GN and Pt/C electrocatalyst in O_2-saturated 0.1 M KOH solution at the scan rate of 10 mV s^{-1} and the rotation rate of 400 rpm. (D) The chronoamperometric responses of Co-CoO/GN and Pt/C at -0.3 V (*vs.* Ag/AgCl) in O_2-saturated 0.1 M KOH solution at the

rotation rate of 200 rpm. (Adapted with permission from Ref [87] Copyright 2012 Wiley-   VCH Verlag GmbH & Co.)
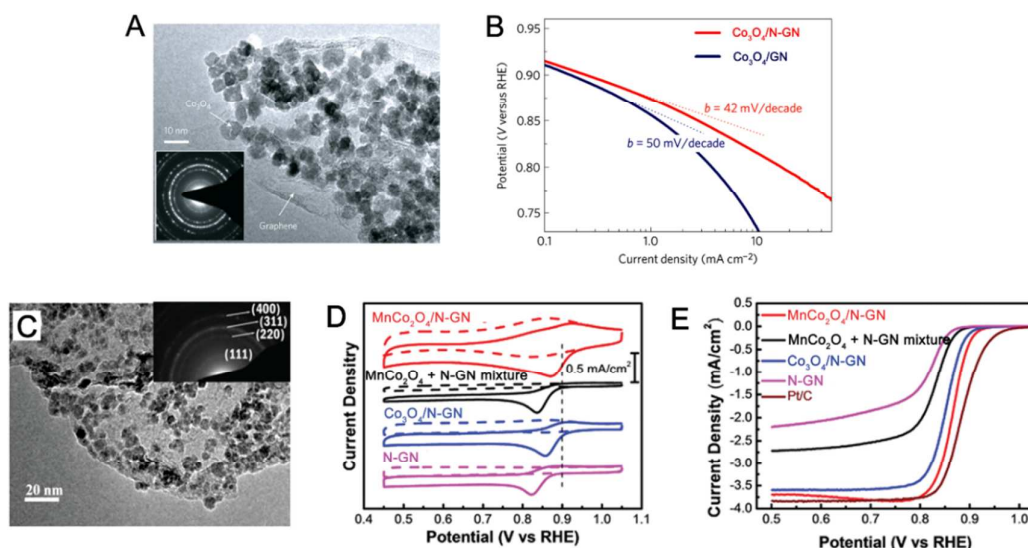
Fig. 22 (A) TEM image of Co_3O_4/N-GN. *Inset* shows an electron diffraction pattern of the hybrid. (B) Tafel plots of Co_3O_4/N-GN and Co_3O_4/GN hybrids for ORR in alkaline medium. (C) TEM image of $MnCo_2O_4$/N-GN. (D) CV curves of $MnCo_2O_4$/N-GN, $MnCo_2O_4$ + N-GN mixture, Co_3O_4/N-GN, and N-GN in O_2-saturated (solid line) or N_2-saturated (dash line) 1 M KOH. (E) ORR polarization curves of $MnCo_2O_4$/N-GN, $MnCo_2O_4$ + N-GN mixture, Co_3O_4/N-GN, N-GN and Pt/C in O_2-saturated 1 M KOH at a sweep rate of 5 mV s^{-1} and rotation rate of 1600 rpm. (Parts A-B, adapted with permission from Ref [89] Copyright 2011 Nature Publishing Group. Parts C-E, adapted with permission from Ref [86] Copyright 2012 American Chemical Society.)

Fig. 23 (A) The concept of the design of (a) Co-Co_3O_4-C and (b) Co-Co_3O_4-C/porous carbons matrix for promoting ORR. TEM image of Co-Co_3O_4-C/porous carbons matrix. (B) ORR polarization curves of different materials in O_2-saturated 0.1 M KOH solution at the scan rate of 10 mV s^{-1} and the rotation rate of 1600 rpm. (Adapted with permission from Ref [90] Copyright 2015 Royal Chemical Society.)

Cobalt(II,III) oxide NPs on 2D N-GN (Co_3O_4/N-GN). In 2011, Liang et al. synthesized Co3O4/N-GN in solution by the growth of Co3O4 NPs onto nitrogen doped GN.[89] The size of Co3O4 in Co3O4/N-GN is ~4-8 nm (Fig. 22A). Control experiment verifies that nitrogen-dopants were onto reduced GO sheets not Co3O4 NPs. The half-wave potential of Co3O4/N-GN for ORR in alkaline medium was 0.83 V, similar to that of the commercial Pt/C, 20 wt.% Pt loading (0.86 V vs. RHE) and more positive than that of Co3O4-GN (0.79 V vs. RHE). The electron transfer number per oxygen molecule of Co3O4/N-GN is ~4.0 at 0.60-0.75 V. Excellent ORR activity of the Co3O4/N-GN

hybrid electrocatalyst was also gleaned from the much smaller Tafel slope of 42 mV decade-1 at low over-potentials than that measured with Co3O4/GN hybrid (54 mV decade-1) in 0.1 M KOH (Fig. 22B). The bond formation between Co3O4 and N-GN and changes in the chemical bonding environment for C, O and Co atoms in the hybrid material are probably responsible for the synergistic ORR catalytic activity. **Manganese-cobalt oxide on 2D N-GN ($MnCo_2O_4$/N-GN).** In order to further tune and optimize the ORR performance of transition metal/N-GN hybrid system,[89] binary MnCo2O4 NPs were also deposited on the surface of N-GN (**Fig. 22C**) through

Mn cation substitution for ORR following the similar chemical synthesis.[86]. In 1 M KOH, the ORR onset potential and peak potential of $MnCo_2O_4$/N-GN were 0.95 and 0.88 V (vs. RHE) (**Figs. 22D-E**), respectively, ~20 mV more positive than those of Co_3O_4/N-GN. This suggests that Mn substitution in the cobalt oxide-N-GN hybrid can further enhance the ORR catalytic activity. XPs results reveal that the superior ORR activity of $MnCo_2O_4$/N-GN is attributed to the covalent coupling of the $MnCo_2O_4$ NPs with N-GN.

Cobalt-Cobalt(II, III) oxide-carbon bishell nanoparticles encapsulated into 3D porous carbons matrix (Co-Co_3O_4-C/porous carbons matrix). As we discussed above, the ORR activity of transition metal-based NPs-GN can be optimized by tuning their interaction between the NPs and GN. In addition to 2D GN, such tune concept can also happen between the metal oxide NPs and 3D carbon nanomaterials. For example, Zou, Guo and co-workers tuned the interaction between electrochemical active transition metal-based NPs and carbon supports for further enhancing the ORR activity.[90] In order to demonstrate such concept, herein, a metal-organic frameworks (MOFs) can be used as a kind of precursor to *in situ* encapsulate Co-Co_3O_4-C NPs into a highly ordered porous carbons matrix.[90] Previously, Co_3O_4 has proved to be ORR active but suffers from low electrical conductivity and low stability.[85, 89] In this work, the organic ligands from MOFs were transformed into porous graphitic carbon, which could *in situ* wrap the metal oxide NPs, resulting in the fancy Co-Co_3O_4-C core-bishell nanostructure. The key part of this work is that they create a very strong interaction/contact between the metal oxide and the carbon shell linked to the porous carbons matrix, which is very important for not only enhancing the electron transfer between NPs and the porous carbons matrix (enhancing the ORR activity), but also making the NPs hard to detach from the porous carbons matrix support (enhancing the ORR stability) (**Fig. 23A**). It is found that in alkaline medium, Co-Co_3O_4-C/porous carbons matrix shows much higher activity for ORR with an onset potential of 0.93 V (vs. RHE) and a half-wave potential of 0.81 V (vs. RHE), very close to those of the Pt/C catalyst with 20 wt.% Pt loading (**Fig. 23B**).

3.3 Transition Metal-Based NPs on 3D Carbon Nanomaterials

Co-Mo nitride supported on 3D N-carbon nanocages (CoMoN/N-carbon nanocages). By combining the merits of the high activity of cobalt nitride and the superb stability of molybdenum nitride, the alloyed CoMoN NPs supported on N-carbon nanocages demonstrates high activity and stability for ORR in acidic medium.[83] Such CoMoN/N-carbon nanocages were prepared through a two-step process.[83] The N-carbon nanocages were first prepared by an *in situ* MgO template method at high temperature. The CoMoN/N-carbon nanocages hybrid electrocatalysts were further synthesized by a convenient impregnation [mixing the N-carbon nanocages suspension in deionized water with cobalt nitrate ($Co(NO_3)_2·6H_2O$) and ammonium molybdate ($(NH_4)_6Mo_7O_{24}·4H_2O$)] and nitridation method (pyrolysis under NH_3 atmosphere). The experimental results show that in O_2-saturated 0.5 M H_2SO_4, the ORR peaks appear at 0.316 V (*vs.* RHE) for MoN/N-carbon nanocages, 0.621 V for $Co_{0.50}Mo_{0.50}N_y$/N-carbon nanocages, and 0.626 V for $Co_{5.47}$N/N-carbon nanocages, respectively (**Fig. 24A**). The corresponding onset potentials are ~0.630, ~0.808, and ~0.810 V (*vs.* RHE), respectively. These mean that the reduction and onset potentials of $Co_{0.50}Mo_{0.50}N_y$/N-carbon nanocages for ORR are both higher than those of $Co_{5.47}$N/N-carbon nanocages and MoN/N-carbon nanocages, suggesting the synergetic effects between Co and Mo. The onset potential for the $Co_{0.50}Mo_{0.50}N_y$/N-carbon nanocages (~0.808 mV *vs.* RHE) is only ~0.147 V lower than that of the Pt/C catalyst with 20 wt.% Pt loading (**Fig. 24B**). The electron transfer number *per* oxygen molecule and the corresponding H_2O_2 yield during the ORR are calculated to be ~3.75 ± 0.10 and ~12.6% in the range of 0.05-0.60 V (*vs.* RHE), indicating a dominant four-electron process. The long-term ORR stability results show the optimized bimetallic CoMoN/N-carbon nanocages electrocatalysts exhibit the best stability with a decrease of ~16% after 100 h of testing, much smaller than the ~36% decrease for $Co_{5.47}$N/N-carbon nanocages and ~75% for Pt/C with 20 wt.% Pt loading (**Fig. 24C**).
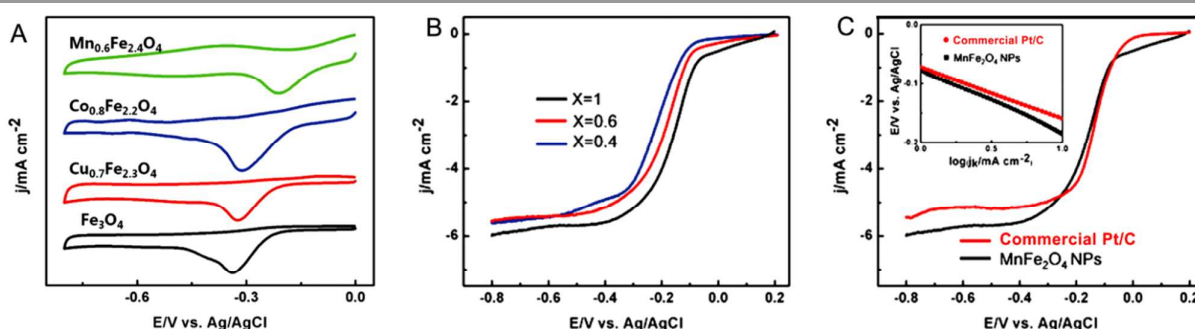
Fig. 24 (A) CVs of CoMoN/N-carbon nanocages, $Co_{0.50}Mo_{0.50}N_y$/N-carbon nanocages and $Co_{5.47}$N/N-carbon nanocages in N_2-saturated and O_2-saturated 0.5 M H_2SO_4 solution. (B) LSV curves of N-carbon nanocages, MoN, $Co_{5.47}$N, and $Co_{0.50}Mo_{0.50}N_y$ in O_2-saturated 0.5 M H_2SO_4 solution at a rotating speed of 1600 rpm. The LSV test of Pt/C was performed in O_2-saturated 0.1 M $HClO_4$ at a rotating speed of 1600 rpm. (C) Chronoamperometric responses of different materials except Pt/C for 100 h in O_2-saturated 0.5 M H_2SO_4 solution under magnetic stirring. The corresponding test for the Pt/C was performed in O_2-saturated 0.1 M $HClO_4$. Applied potential: 0.2 V (*vs.* Ag/AgCl). (Adapted with permission from Ref [83] Copyright 2015 Wiley-VCH Verlag GmbH & Co.)

Journal Name

ARTICLE

Nickel-iron incorporated 3D nitrogen-doped mesoporous carbons (FeNi/N-mesoporous carbons). The synergetic effects from multiple active sites for ORR also happen on FeNi/N-mesoporous carbons.[91] In the synthesis strategy, mesoporous SBA-15 was selected as the support and further decorated by nitrogen-doped nanocarbons that acted as the nanoreactor for the *in situ* growth of well-dispersed alloy NiFe alloy NPs. Although the FeNi/N-mesoporous carbons showed a slightly higher onset potential than the Pt/C (10 wt.% Pt loading), the former manifests several distinct advantages over the Pt/C catalyst such as better tolerance, higher durability and cheaper price. The high ORR activity of FeNi/N-mesoporous carbons should be attributed to the uniformly dispersed FeNi-alloy NPs in the nanochannels of the ordered porous structure, making the catalytic sites readily accessible for electroactive substances. Furthermore, because the FeNi/N-mesoporous carbons were produced by annealing at a high temperature, and the active sites were embedded in nanochannels of the porous structure and further protected by a layer of nanocarbon. Such particular structures make the above materials show long-term stability for ORR.

4. Engineering Stable Noble-Metal-Free Fe₃C-Based NPs/Carbon Nanomaterials Composites for ORR

Carbon nanomaterials functionalized with stable Fe$_3$C-Based NPs are considered as a kind of more novel catalyst for ORR in both acid and alkaline solution.[182, 200, 202] Those catalysts with little nitrogen or metallic functionality on their surface exhibit very high activity and stability towards the ORR.[202] Recent researches suggest that the inner Fe$_3$C NPs which are protected by outer graphitic layers play a synergetic role in activating the outer graphitic layers towards ORR.[202] These make carbon nanomaterials functionalized with Fe$_3$C-based NPs to be the good candidates for the future active and stable ORR electrocatalysts.

4.1 Fe₃C-based NPs on 1D Carbon Nanomaterials

4.1.1 Fe-Fe₃C modified on Nitrogen-enriched 1D carbon nanorods (N-Fe-Fe₃C/carbon nanorods)

1D N-Fe-Fe$_3$C/carbon nanorods were synthesized by annealing the mixture of NH$_2$CN and FeCl$_3$ at 750 °C (**Fig. 25A**).[198] **Fig. 25B** presents the Fe$_3$C/carbon nanorods with a distinctive core-shell structure. In 0.1 M pH 7.0 phosphate buffered solution, the kinetic current density of N-Fe-Fe$_3$C/carbon nanorods at 0 V (26.89 mA cm^{-2}) was almost twice higher than that of the commercial Pt/C (10 wt.% Pt loading, 14.20 mA cm^{-2}), suggesting the markedly improved dynamics of N-Fe-

Fe$_3$C/carbon nanorods for ORR. An H-type microbial fuel cells (MFCs) was further set up to study the possibility of using N-Fe-Fe$_3$C/carbon nanorods as an alternative cathode electrocatalyst to Pt/C with 10 wt.% Pt loading (**Fig. 25C**). The N-Fe-Fe$_3$C/carbon nanorods-based MFCs generate an average power output density of 0.18 W m^{-3}, three times higher than the average power output (0.054 W m^{-3}) in the Pt/C (10 wt.% Pt loading)-based MFCs (**Fig. 25D**). Furthermore, the N-Fe-Fe$_3$C/carbon nanorods-based MFCs display a charge transfer resistance of 8.9 Ω, much lower than that of the Pt/C (10 wt.% Pt loading)-based MFCs (25.7 Ω), suggesting that the N-Fe-Fe$_3$C/carbon nanorods-based MFCs possess a superior catalytic performance for ORR. Polarization tests show both MFCs present a comparable open circuit voltage of around 0.82 V (**Fig. 25E**). However, the N-Fe-Fe$_3$C/carbon nanorods-based MFCs achieved a maximum power density of 4.20 W m^{-3} and a short-circuit current density of 25.39 A m^{-3}, higher than those of the Pt/C (10 wt.% Pt loading)-based MFCs (3.98 W m^{-3} and 21.23 A m^{-3}, respectively) (**Fig. 25E**).
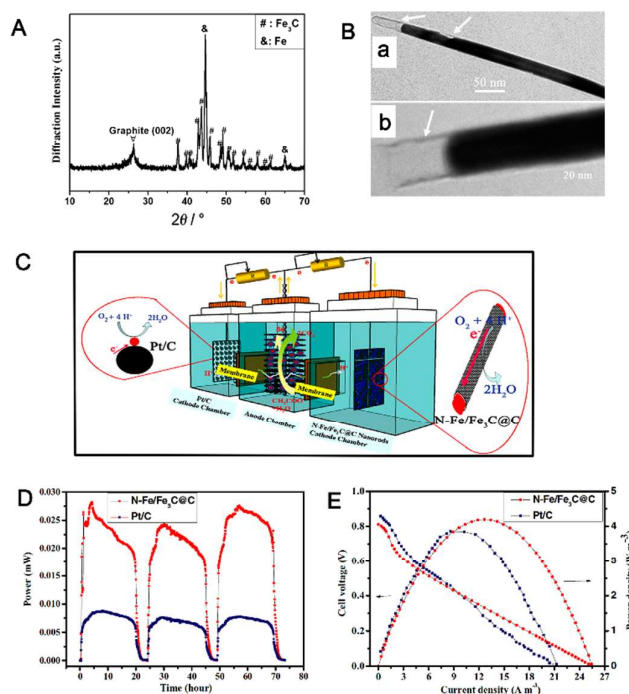
Fig. 25 (A) XRD patterns of N-Fe-Fe$_3$C/carbon nanorods. (B) TEM images of a single N-Fe-Fe$_3$C/carbon nanorods with close-end graphite shell (a) and single N-Fe-Fe$_3$C/carbon nanorods with open-end graphite shell (b). (C) Schematic diagram of the designed MFC with two testing cathode chambers sharing the same anode. N-Fe/Fe$_3$C@C nanorods in the figure are the N-Fe-Fe$_3$C/carbon nanorods. (D) The output power density with R$_{ex}$ loading of 1 Ω in N-Fe-Fe$_3$C/carbon nanorods-based MFCs and Pt/C-based MFCs (E) MFCs polarization and power density curves with N-Fe-Fe$_3$C/carbon nanorods and Pt/C

cathodes. N-Fe/Fe$_3$C@C nanorods in the figure are the N-Fe-Fe$_3$C/carbon nanorods. (Adapted with permission from Ref [198] Copyright 2012 Wiley-VCH Verlag GmbH & Co.)

4.1.2 Fe$_3$C on 1D CNTs (Fe$_3$C/CNTs)

To further explore more active non-noble metal catalysts for ORR, Fe$_3$C/CNTs hybrids were prepared by annealing a mixture of Pluronic P123 [i.e., Poly(ethylene glycol)-block-poly(propylene glycol)-block-poly(ethylene glycol)], melamine, and Fe(NO$_3$)$_3$ at 800 °C in N$_2$.[199] TEM result (**Fig. 26A**) shows that the Fe-based (NPs are distributed either at the tip or inside of CNTs with the diameter of 50-110 nm. The lattice distance of 0.21 nm in HRTEM image (**Fig. 26B**) corresponds to the (211) crystal planes of the Fe$_3$C phase. XRD pattern of Fe$_3$C/CNTs hybrids shows the peaks located at 37.8°, 43.9°, 45.0°, 46.0°, 49.2, and 54.5°, corresponding to Fe$_3$C crystal structure (**Fig. 26C**). Fe$_3$C/CNTs show much higher electrocatalytic activity toward ORR than the commercial Pt/C (20 wt.% Pt loading), as indicated by their 49 mV more positive half-wave potential than that of the commercial Pt/C (**Fig. 26D**). Rotating ring-disk electrode test results reveal that the H$_2$O$_2$ yield at Fe$_3$C-CNTs is below 7.7% within the potential range between 0.3 and 0.9 V (*vs.* RHE) in alkaline medium, corresponding to a high electron-transfer number of 3.99. Such negligible H$_2$O$_2$ yield clearly confirms the extremely high

ORR electrocatalytic efficiency at the Fe$_3$C/CNTs hybrids. The Tafel slope (91.2 mV decade^{-1}) of Fe$_3$C/CNTs is closed to that of Pt/C with 20 wt.% Pt loading (84.8 mV decade^{-1}), suggesting a good kinetic process of Fe$_3$C/CNTs for ORR in alkaline medium. They also show very high stability for ORR with no shift in ORR polarization curve after 3000 cycles between 0.364 to 0.964 V (**Figs. 26E**). While there is a 23 mV loss of half-wave potential for the Pt/C electrocatalyst (20 wt.% Pt loading) under the same conditions (**Figs. 26F**). In addition, the Fe$_3$C/CNTs electrocatalyst is also active for ORR in acidic solution. The onset potential of Fe$_3$C/CNTs for ORR in acidic solution is closed to that of Pt/C with 20 wt.% Pt loading (**Fig. 26G**). The H$_2$O$_2$ yield on the Fe$_3$C/CNTs electrocatalyst in acidic solution is below 4.1% between 0.25 V and 0.6 V (vs. RHE), revealing a four-electron-pathway dominated ORR process. The kinetic currents show a Tafel slope of 134 mV decade^{-1} at low overpotentials, close to 108.5 mV decade^{-1} for the Pt/C. The Fe$_3$C/CNTs electrocatalyst also shows superior stability for ORR than the Pt/C electrocatalyst, as revealed by a much lower ORR polarization curve change on Fe$_3$C-CNTs than on the Pt/C electrocatalyst (**Figs. 26H-I**). The above characteristics make Fe$_3$C/CNTs one of the best non-noble-metal electrocatalysts ever reported for ORR in both alkaline and acidic medium.
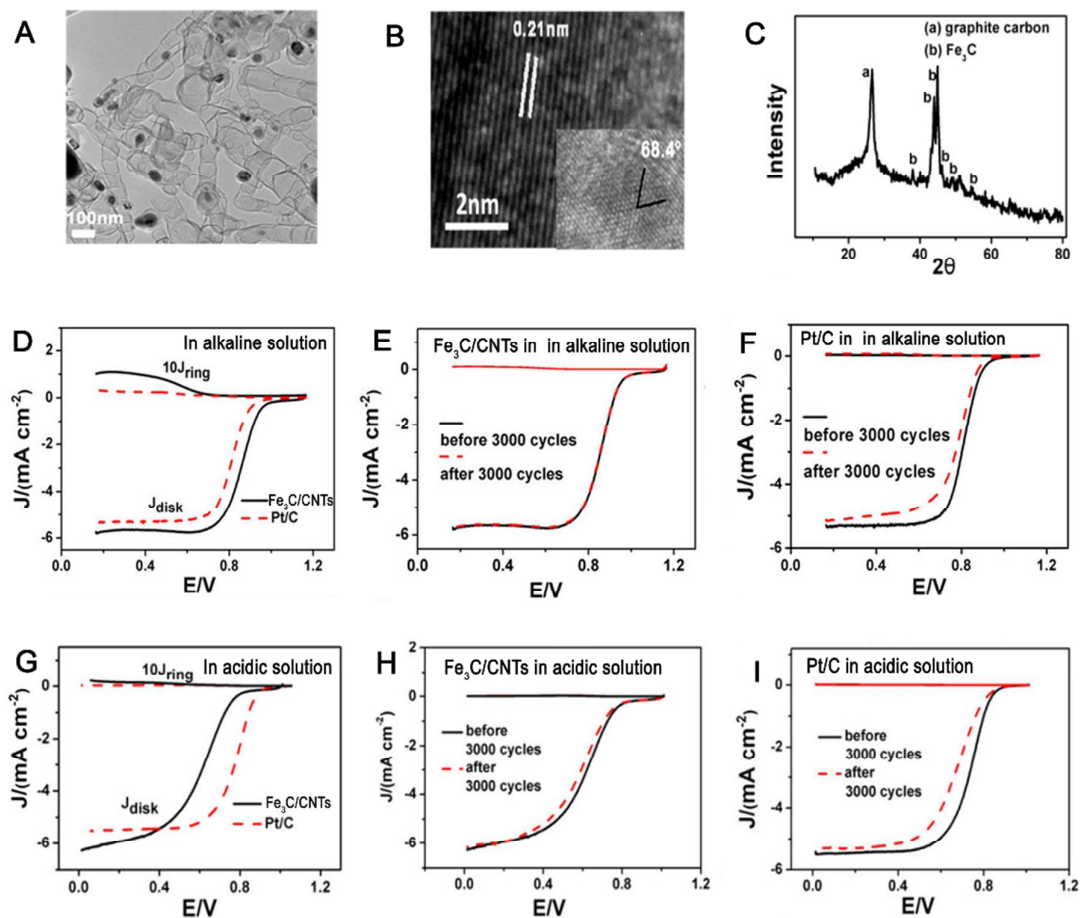
Fig. 26 TEM (A), HRTEM images (B) and XRD pattern (C) of Fe_3C/CNTs. (D) Rotating ring-disk electrode voltammograms of Fe_3C/CNTs in O_2-saturated 0.10 M KOH solution at the scan rate of 5 mV s^{-1} and the rotation rate of 1600 rpm. (E) LSV curves of Fe_3C/CNTs for ORR in O_2-saturated 0.10 M KOH solution before and after 3000 cycles. (F) LSV curves of Pt/C for ORR in O_2-saturated 0.10 M KOH solution before and after 3000 cycles. (Adapted with permission from Ref [199] Copyright 2015 American Chemical Society.)

### 4.2 Fe$_3$C-Based NPs on 2D Carbon Nanomaterials

Based on their previous work for Fe_3C-based carbon hollow sphere electrocatalyst,[202] Xing, Li and co-workers further reported the direct fabrication of 2D functionalized few-layer GN sheets (*i.e.*, Fe_3C/GN sheets) by one-step high-temperature autoclave synthesis (**Fig. 27A**).[200] In alkaline medium, the ORR activity of Fe_3C/GN sheets is close to that of Pt/C (20 wt.% Pt loading) (**Fig. 27C**). The rotating ring-disk electrode analysis discloses that this peroxide yield on Fe_3C/GN sheets corresponds to an electron-transfer number of 3.7. The stability of the Fe_3C/GN sheets and Pt/C electrocatalyst is assessed by the chronoamperometric test; the Fe_3C/GN sheets exhibit a slow attenuation and high current retention (70%) after 16 h (**Fig. 27D**). In comparison, the Pt/C electrocatalyst (20 wt.% Pt loading) shows a much faster current decrease with only 58% retention after 16 h (**Fig. 27D**). Considering the similar encapsulation structure and the nitrogen doping level of Fe_3C/GN sheets with the hollow sphere electrocatalyst previously reported,[202] the Fe_3C/GN sheets electrocatalyst should have a similar ORR mechanism, that is, the synergetic effect between protective GN sheets and the encapsulated Fe_3C nanoparticles may be responsible for the high ORR activity and stability of the Fe_3C/GN sheets electrocatalyst.

4.3 Fe$_3$C-Based NPs on 3D Carbon Nanomaterials

4.3.1 N-Doped Fe-Fe$_3$C on 3D carbon foams (N-Fe-Fe$_3$C/carbon foams)

In 2013, Lee *et al.* produced N-Fe-Fe_3C/carbon foams starting with the commercially available melamine foams.[201] XRD analysis indicates that metallic Fe, Fe_3C, and graphitic carbon co-exist (**Fig. 28A**), and the well-defined crystalline phase has a lattice fringe with a *d* spacing of 0.184 nm, consistent with the (221) plane of Fe_3C (**Fig. 28B**). Although the onset and the half potentials of N-Fe-Fe_3C/carbon foams for ORR are both lower than those at Pt/C electrocatalyst with 20 wt.% Pt loading,

their current density is even slightly higher than that for Pt/C electrocatalyst at high overpotentials (**Fig. 28C**). The number of electrons transferred on N-Fe-Fe_3C/carbon foams is determined to be ~3.7 to 3.85 (at the potentials between -0.1 V and -0.7 V *vs.* Hg/HgO) in 0.1 M KOH, suggesting that it is an efficient four-electron transfer pathway. The stability tests reveal that the Fe-Fe_3C/carbon foams degrade in a slower rate than the Pt/C catalyst (**Fig. 28D**).
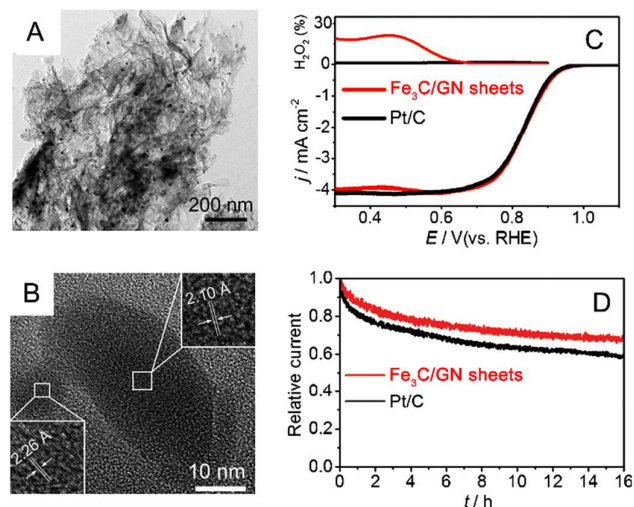
Fig. 27 (A) TEM and (B) HRTEM images of Fe_3C/GN sheets. (C) ORR polarization plots (bottom) and H_2O_2 yield plots (top) measured with Fe_3C/GN sheets and Pt/C electrocatalyst on rotating ring-disk electrode at 900 rpm in O_2-saturated 0.1 M KOH. The scan rate was 10 mV s^{-1}. (D) Chronoamperometric responses of Fe_3C/GN sheets and Pt/C electrocatalyst at 0.8 V (*vs.* RHE) on rotating disk electrode at 1000 rpm in O_2-saturated 0.1 M KOH solution. (Adapted with permission from Ref [200] Copyright 2014 Wiley-VCH Verlag GmbH & Co.)
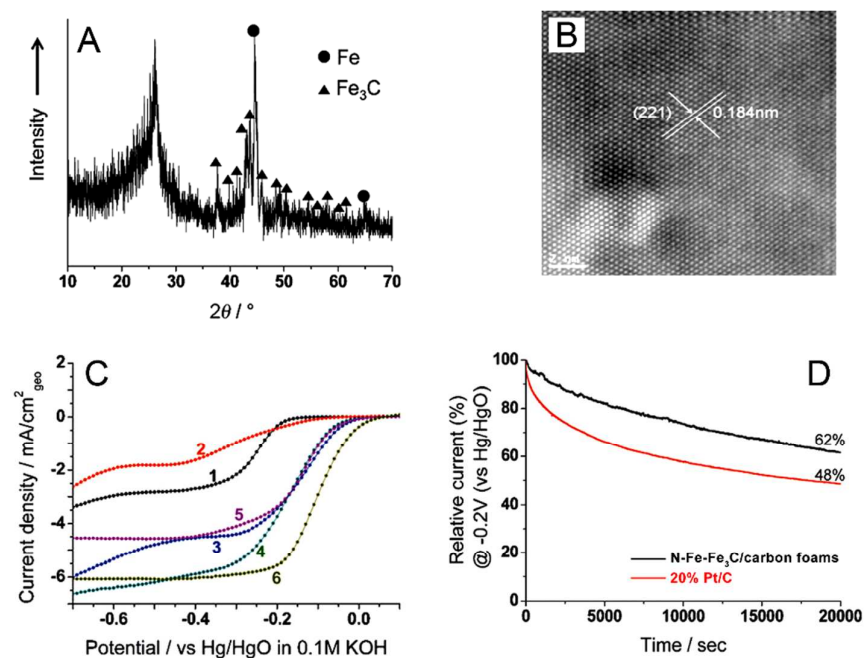
Fig. 28 (A) XRD and (B) HRTEM image of N-Fe-Fe₃C/carbon foams. (C) LSV curves of pure Ketjen black (1), carbonized melamine foam (2), a physical mixture of Fe/Fe₃C melamine and Ketjen black (3), N-Fe-Fe₃C/carbon foams (4), 9.55 mg$_{Pt}$ cm^{-2} (5), and 28.6 mg$_{Pt}$ cm^{-2} (6) in O₂-saturated 0.1 M KOH at the rotation rate of 2000 rpm. Non-precious-metal electrocatalyst loadings were 0.286 mg$_{cat}$ cm^{-2}. (D) Chronoamperometric responses of N-Fe-Fe₃C/carbon foams and Pt/C in O₂-saturated 0.1 M KOH solution at -0.2 V (*vs.* Hg/HgO) and 1600 rpm. (Adapted with permission from Ref [201] Copyright 2013 Wiley-VCH Verlag GmbH & Co.)

4.3.2 Fe₃C on 3D nitrogen and iron co-doped carbonized nanoscale MOFs (Fe₃C/N-Fe-carbonized MOFs)

Monodisperse nanoscale N-Fe-carbonized MOFs containing Fe₃C NPs can be used as an advanced template for making a new kind of Fe₃C/ N-Fe-carbonized MOFs with the specific surface area of 326 m² g^{-1} and the uniform pore size of ~3.8 nm for boosting ORR.[204] The amorphous carbon matrix, the embedded Fe₃C, graphite carbon, and Fe particles, are discerned by the HRTEM images (**Figs. 29A-C**). In alkaline electrolyte, Fe₃C/N-Fe-carbonized MOFs exhibit the ORR onset potential of 1.03 V *vs.* RHE, which is slightly positive than that of the commercial Pt/C with 20 wt.% Pt loading (1.01 V *vs.* RHE) (**Fig. 29D**). The transferred electron number *per* oxygen molecule for Fe₃C/ N-Fe-carbonized MOFs is calculated to be approximately 3.97 over the potential range from 0.55 to 0.73 V (*vs.* RHE). The rotating ring-disk electrode measurement further proves that there is negligible ring current, and the transferred electron number *per* oxygen molecule calculated from the LSV curves is about 3.98 over the potential range from 0.16 to 0.76 V (*vs.* RHE). These experimental results demonstrate that the four-electron process is the dominating pathway for ORR at the N-Fe-Fe₃C/carbonized MOFs.

Furthermore, the current density of the Fe₃C/N-Fe-carbonized MOFs shows a much slower decay than that of the Pt/C (**Fig. 29E**). About 21% loss of the current density is occurred at the Fe₃C/N-Fe-carbonized MOFs after 40000 s, whereas the corresponding current loss at the Pt/C under the same condition is as high as 47%. This result exemplifies that the Fe₃C/N-Fe-carbonized MOFs electrocatalyst is more stable than the commercial Pt/C electrocatalyst. Furthermore, alkaline direct methanol fuel cells based on Fe3C/N-Fe-carbonized MOFs and Pt/C (20 wt.% Pt loading) are constructed for the comparative performance evaluation (Fig. 29F) under the identical conditions. The open circuit voltage for the alkaline direct methanol fuel cells equipped with the N-Fe-Fe3C/carbonized MOFs cathode (3 mg cm-2 electrocatalyst) is as high as 0.81 V, which is higher than 0.74 V for the cell equipped with the Pt/C cathode (3 mg cm-2 electrocatalyst), indicating better methanol tolerance of the N-Fe-Fe₃C/carbonized MOFs for ORR. Furthermore, the peak power density and current density reach 22.7 mW cm^{-2} and 93.9 mA cm^{-2} at the cathode with the Fe₃C/N-Fe-carbonized MOFs electrocatalyst, respectively, which are about 1.7 times and 1.4 times higher than those of the Pt/C cathode.
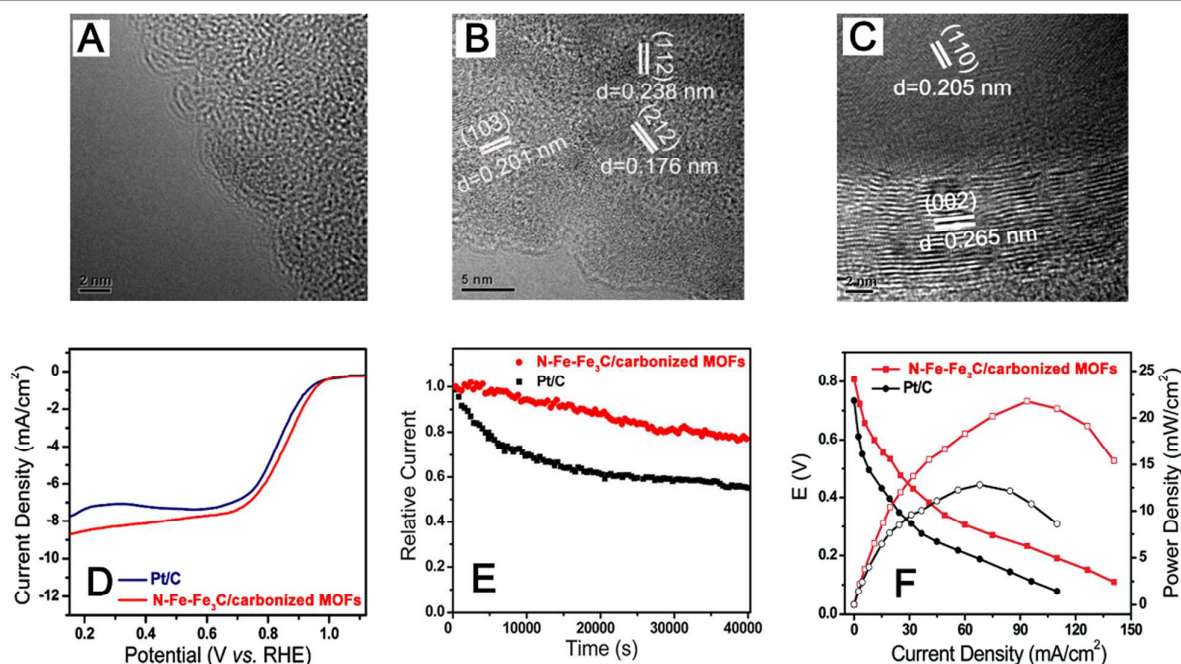
Fig. 29 HRTEM images of (A) amorphous carbon, (B) Fe₃C and (C) Fe@C in Fe₃C/N-Fe-carbonized MOFs. (D) LSV curves of Fe₃C/N-Fe-carbonized MOFs and Pt/C in O₂-saturated 0.1 M KOH at a rotation rate of 1600 rpm. (E) Chronoamperometric responses of Fe₃C/N-Fe-carbonized MOFs and Pt/C at 0.84 V (*vs.* RHE) for 40000 s in O₂-saturated 0.1 M KOH. (F) Alkaline direct methanol fuel cells single-cell performance constructed with Fe₃C/N-Fe-carbonized MOFs and Pt/C at 60 °C under the same condition. (Adapted with permission from Ref [204] Copyright 2014 American Chemical Society.)

4.3.3 Fe₃C on 3D carbon microspheres (Fe₃C/carbon microspheres)

Despite Fe₃C-based materials show obvious advantage in enhancing ORR, the role of the Fe₃C phase in ORR catalysis is not clearly understood,[202] probably because previous reported Fe₃C-based materials were a mixture of several phases consist of carbon-coated Fe₃C in different scales, bare Fe₃C, and metallic Fe particles, making them difficult to conclude the role of the Fe₃C phase in the ORR. More critically, the possible use of the Fe₃C-based electrocatalysts in acidic media is apparently out of question as the carbide will dissolve in acid. To mitigate these issues, the novel hollow microspheres comprising uniform Fe₃C NPs encased by graphitic layers were prepared through one-step high-pressure pyrolysis using ferrocene and cyanamide as precursors.[202] The Fe₃C/carbon microspheres are hollow with a diameter of 400 - 500 nm and a shell thickness of ~60 nm (**Fig. 30A**). HRTEM images (**Fig. 30B**) and XRD pattern confirm the presence of Fe₃C phase in Fe₃C/carbon microspheres. The unique chemical stability provided by Fe₃C/carbon microspheres leads to excellent ORR stability in acidic media (**Fig. 30D**). In 0.1 M HClO₄, the ORR polarization curve of Fe₃C/carbon microspheres exhibits a half-wave potential of ~0.73 V *vs.* RHE, ~0.1 V lower than that of Pt/C, 20 wt.% Pt loading (**Fig. 30D**). The H₂O₂ yield is found to be less than 8 % at the potential between 0.1 and 0.8 V (*vs.* RHE) and

decreases to ~6% at potentials below 0.6 V (*vs.* RHE), indicating a four-electron pathway dominated ORR process. To further investigate the ORR mechanism of Fe₃C/carbon microspheres, a destructive test is conducted by ball-milling to destroy the protective carbon shells of Fe₃C/carbon microspheres around the carbide nanoparticles. After the milling, the Fe₃C NPs are exposed and therefore largely removed in hot acid during the following leaching. As expected, the obtained Fe₃C/carbon microspheres-BL loses the ORR catalytic activity (**Fig. 30E**). Therefore, the very high activity of Fe₃C/carbon microspheres in acid solution is resulting from the encased carbide NPs activate the surrounding graphitic layers (**Fig. 30C**), making the outer surface of the carbon layer much more active for ORR. At the same time, another kind of noble-metal-free Fe₃C-based NPs/carbon nanomaterial composites (*i.e.*, Fe₃C/porous carbons) were fabricated by annealing the Fe(NO₃)₃ impregnated filter paper.[203] The electron-transferred number *per* oxygen molecule on Fe₃C/porous carbons is ~3.82 - 3.97, and the H₂O₂ yield is below 17.3% over the potential range of -0.2 to -0.65 V (*vs.* Ag/AgCl) in alkaline medium, suggesting their superior electrocatalytic ORR activity. Fe₃C/porous carbons also show higher stability for ORR than the Pt/C.

Journal Name

ARTICLE
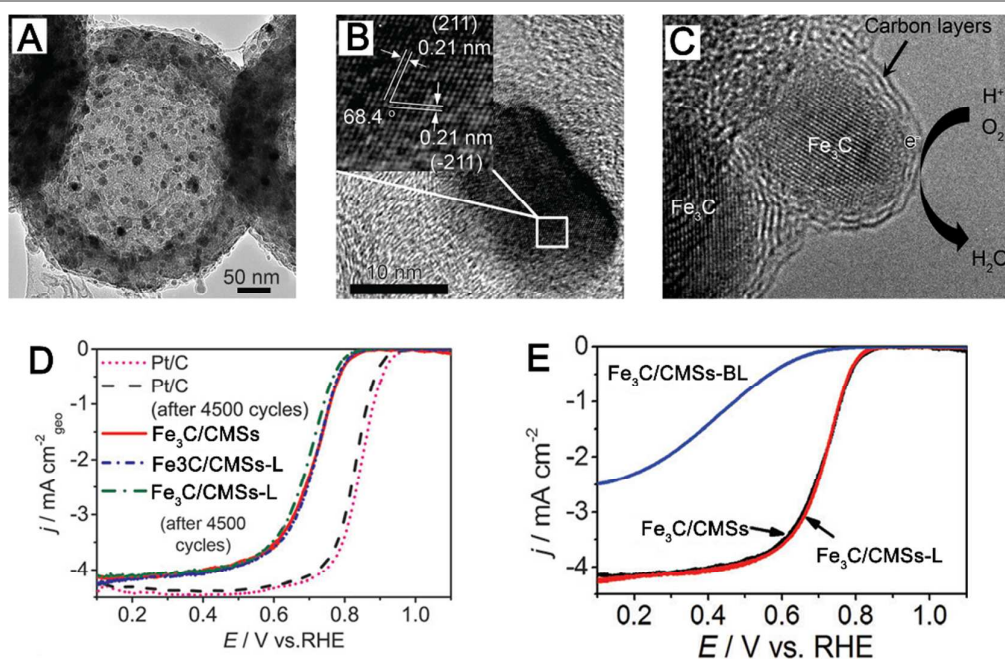
Fig. 30 (A-C) TEM images of Fe₃C/carbon microspheres. (D) LSV curves of Fe₃C/carbon microspheres, Fe₃C/carbon microspheres-L and Pt/C in O₂-saturated 0.1 M HClO₄ before and after 4500 potential cycles at the scan rate of 10 mV s⁻¹ and the rotating speed of 900 rpm. Potential cycling was carried out between 0.6 and 1.0 V (*vs.* RHE) in N₂-saturated 0.1 M HClO₄. (E) LSV curves of Fe₃C/carbon microspheres, Fe₃C/carbon microspheres-L, and Fe₃C/carbon microspheres-BL in O₂-saturated 0.1 M HClO₄. (Adapted with permission from Ref [202] Copyright 2014 Wiley-VCH Verlag GmbH & Co.)

4.3.4 Fe-N decorated CNTs grown on hierarchically porous carbon (Fe-N-CNTs-OPCs)

As discussed above, Fe₃C-based NPs on 3D carbon nanomaterials with different structures have been recently reported, such as foams,[201] MOFs,[204] and microspheres.[202] However, the ORR performance of these composites still can hardly match that of Pt/C (20 wt.% Pt loading) in the terms of ORR onset potential and current density.[268] Recently, by exploring a simple, low-cost and eco-friendly bottom-up route, Qiao and co-workers developed a novel 3D porous Fe-N-C hybrid material (*i.e.*, Fe-N-CNTs-OPCs), composed of hierarchically ordered porous carbons (OPCs) microblocks interlinked *via in situ* grown CNTs, for effectively catalyzing ORR.[268] SEM image (**Fig. 31A**) shows that ordered macropores are ~200 nm in diameter, and large amounts of entangled CNTs clusters are observed on OPCs microblocks, interlinking them into a network. HRTEM images reveal that the iron NPs are found to be encapsulated either inside each compartment of the bamboo-structure or on the tip of CNTs (*inset of* **Fig. 31A**). Energy-dispersive X-ray spectroscopy (EDS) elemental mapping shows the homogeneous distribution of C, N, and O elements on both OPCs and CNTs in Fe-N-CNTs-OPCs (**Fig. 31E**).

Apart from the intensive Fe signals from the iron particles, Fe species were also detected on other sections where no Fe particles were observed. Such finely dispersive Fe species could possibly bond with the neighboring C or N atoms, which is believed to be highly active for ORR. In alkaline solution, the Fe-N-CNTs-OPCs displays a positive ORR onset potential within 18 mV close to that of Pt/C with 20 wt.% Pt loading at low over-potential (**Fig. 31B**). This has rarely been achieved and is even more positive than those of some recently reported carbon nanomaterials-based noble-metal-free ORR electrocatalysts.[8, 42, 55-58, 168-176, 182, 194-196, 214, 267, 269-271] Furthermore, the Fe-N-CNTs-OPCs exhibits less than 1% of peroxide yield, corresponding to an electron transfer number up to 3.99 (**Fig. 31C**), which confirms their extremely high ORR efficiency through the high efficient 4-electron pathway. In contrast, the sample without *in situ* formed CNTs (*i.e.*, Fe decorated ordered porous carbon with only non-graphitized hollow carbon nanofibers, Fe-N-CNFs-OPCs) shows higher peroxide yield and lower efficiency (2-electron ORR pathway) (**Fig. 31C**). It should be noteworthy that the cost economy of Fe-N-CNTs-OPCs is far more economical than the commercial Pt/C (columns with color) by giving out a significantly higher

ORR activity *per* cost unit, due to its much lower price for synthesis (**Fig. 31D**), suggesting the extremely promising potential for the commercial ORR application in alkaline medium.
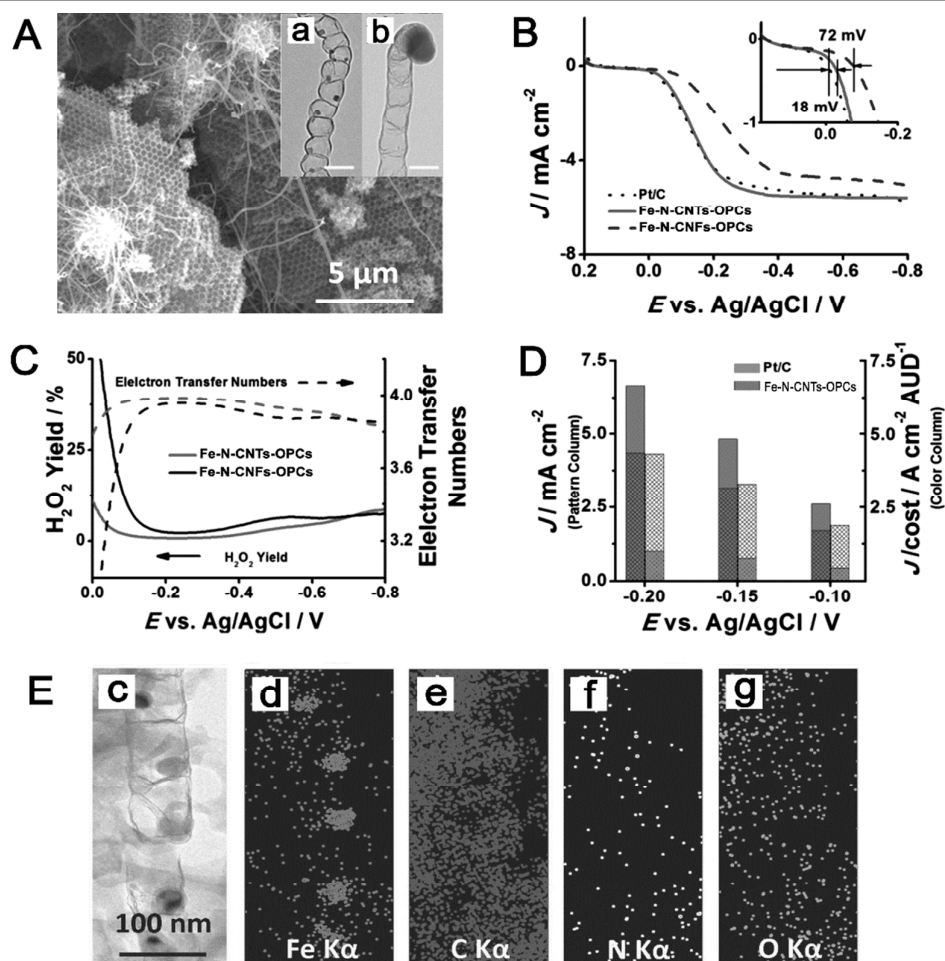
Fig. 31 (A) SEM image of Fe-N-CNTs-OPCs. *Inset*: TEM images of Fe-N-CNTs-OPCs (a, b). (B) ORR polarization curves of Pt/C (20 wt.% Pt loading), Fe-N-CNTs-OPCs and Fe-N-CNFs-OPCs in O_2-saturated 0.1 M KOH solution at the scan rate of 5 mV s^{-1} and the rotation rate of 1600 rpm. (C) Peroxide yield (solid) and electron transfer numbers (dash) for Fe-N-CNTs-OPCs and Fe-N-CNFs-OPCs. (D) ORR current (pattern column) and the corresponding cost-efficiency (color column) of Pt/C (20 wt.% Pt loading), Fe-N-CNTs-OPCs at different potentials. (E) TEM image and corresponding elemental mappings of the same area of Fe-N-CNTs-OPCs. (Adapted with permission from Ref [268] Copyright 2014 Wiley-VCH Verlag GmbH & Co.)

4.3.5 Fe-N doped graphitic carbon bulbs (Fe-N-GCBs)

To further reduce the cost of the ORR catalysts, Qiao's group fabricated Fe-N-GCBs by critically select the cheap and self-made Prussian blue as the only precursor. Importantly, the pyrolysis temperature of PB can be as low as 550 °C, avoiding some severe drawbacks including the loss of doped nitrogen which is essential to ORR and the origin of high cost of the final product during the high temperature synthesis. In alkaline electrolyte, the ORR onset potential of the Fe-N-GCBs is slightly higher than that of Pt/C though the peroxide production of the Fe-N-GCBs is a little bit higher than that of Pt/C. In the acid electrolyte, the performance of the Fe-N-GCBs is to some extent lower than that of Pt, but not too far behind it. The peroxide ratio of the Fe-N-GCBs is also very low (<4%). According to Gasteiger's benchmark, the volumic current of a non-Pt catalyst should be at least 1/10 of the Pt/C for economic viability in fuel cell applications.[40] In the acid electrolyte, the current density of the Fe-N-GCBs at 0.8 V (*vs.* RHE) is about 1/4 of Pt/C. Assuming that the density of the material is 1/2 of the Pt/C, the volumic current density of the material is 1/8 of Pt/C, which is above the benchmark. These make Fe-N-GCBs to be one of the promising and economical catalysts for ORR in both alkaline and acid media.

5. Conclusions and Perspectives

This review provides a summary of the recent development of advanced carbon nanomaterials with different dimensions as the support of heteroatoms, transition metals-based NPs and especially Fe_3C-based NPs for the rational design of high-efficiency carbon nanomaterials-based noble-metal-free oxygen reduction electrocatalysts. Single heteroatom (*e.g.*, N, B, S, I, Cl, Br, Se and P) or multiple heteroatoms (*e.g.*, BN, NP, NS, NSi, FNS, NPS and NPS) doping of different carbon

nanomaterials shows promising electrocatalytic activity because they exhibit comparable or even higher electrocatalytic activity, longer-term stability, and greater tolerance against fuel crossover and carbon monoxide poisoning than the commercially available Pt/C. Transition metal-based NPs (*e.g.*, CoO, MnCo$_2$O$_4$, Co-CoO, Co$_3$O$_4$, CoMoN, Co-Co$_3$O$_4$-C and FeNi) couple with advanced carbon nanomaterials have exhibited remarkable electrocatalytic performance (higher activity and stability) for ORR as compared to their unsupported counterparts. Superior ORR activity is attributed to the synergetic effect between the advanced carbon nanomaterials and transition metal-based NPs; the graphitic shell with little nitrogen and metallic functionality and the inner core of Fe$_3$C-based NPs exhibit high activity and stability towards the ORR. Such synergetic effect in activating the outer graphitic layers towards ORR makes carbon nanomaterials functionalized with Fe$_3$C-based NPs a novel class of ORR electrocatalyst operating in both alkaline and acidic media.

Although considerable progress has been made in the development of high-efficiency carbon nanomaterials-based noble-metal-free ORR electrocatalysts, the development of ultimate materials for commercial ORR electrocatalysts remains a challenge.

Metal-free heteroatom-doped carbon nanomaterials for ORR. **(i) Metallic impurities *vs.* heteroatoms doping for ORR.** It was found that the metallic impurities present in CNTs play an important role in enhancing the electrocatalytic activity of CNTs on different analytes,[272-282] such as oxygen.[283] In particular, recent results have shown that even "impurities of impurities" on the level of tens of atoms have the direct influence on electrochemistry of CNTs[282, 284, 285] Also, the researchers believe that metal impurities are very often present within GN materials, and such residual impurities result in a significant alteration of the electrochemical behavior of the materials.[286-290] Some recent heteroatom-doped GN materials as "metal-free" electrocatalysts, initially prepared by Hummers method,[291] for ORR suffer from contamination of manganese besides other impurities.[292] In order to clarify the electroactive sites of heteroatom doped-CNTs, a new method was proposed to synthesize the truly metal-free N-CNTs.[104] Owing to the metal-free growth, the observed electrocatalytic activity toward ORR of the newly produced N-CNTs can be exclusively attributed to the incorporation of nitrogen in the CNTs structure, which is a solid evidence that nitrogen doping dramatically enhances the electrocatalytic activity of CNTs for ORR.[104] It is reasonable to believe that the electron-accepting ability of the nitrogen atoms have created net positive charge on adjacent carbon atoms to attract electrons from the anode for facilitating ORR.[107] However, regarding that a plenty of metal-free heteroatom-doped carbon nanomaterials are derived from the carbon materials produced on using metal catalysts; therefore, it would be prudent to discuss the ORR mechanisms of these "metal-free" heteroatom-doped carbon materials. **(ii) The effect of single type of heteroatom functionality on ORR.** In most cases, there are different types of heteroatom

functionalities existing in single heteroatom-doped carbon nanomaterials,[89-146, 148-163, 197] making it hard to determine the effect of single type of heteroatom on ORR. Identified by XPS, a mixture of pyridinic N, pyrrolic N and/or graphitic N was usually found in N-doped carbon nanomaterial.[89-146, 148-163, 197] One point is that graphitic N, which are far from N-GN sheet edges, are active sites for ORR whereas those that are close to the edges are less active.[293] Conversely, another viewpoint is that only pyridinic N next to the zigzag edge can facilitate O$_2$ adsorption for enhancing ORR whereas the graphite N inside the GN domain does not contribute to the ORR activity.[294] Another study by the combination of theoretical calculations and experiments indicates that O$_2$ can be activated on both graphitic N and pyridinic N species.[295] Such controversy indicates that though elaborate experiments and careful theoretical calculations were executed, different groups/researches gave different explanations for the effect of single type heteroatom on ORR, and the exact mechanisms remain unclear.[104, 107-110] In order to solve this problem, Li *et al.* prepared several kinds of N-GN quantum dots molecules with the exactly known structures/functional groups by the organic synthesis. They solidly prove that the N-GN quantum dots with the smaller size lead to a more negative onset potential and a lower ORR current,[128] considered as a kind of more direct and efficient way to determine the exact effect of single type heteroatom on ORR. We believe in the future the researchers will be able to directly compare the ORR performance between the molecules with and without nitrogen (heteroatom) incorporation or with different nitrogen functional groups. We trust that with the progress of the processing technology, especially the advanced organic synthesis allowing us to prepare nitrogen doped graphenes, the mechanism of effect of single type of heteroatom functionality on ORR will be finally be realized and such understanding will benefit the development of ORR electrocatalysts with optimized performance. **(iii) Surface area *vs.* surface active sites/defects for ORR.** In most cases, larger surface area of the electrocatalysts would result in more active sites/defects, leading to better ORR activity (*i.e.*, larger current density and/or lower overpotential). But meanwhile, large amounts of active sites/defects on surface may also lower material conductivity and reduce the ORR performance, accordingly. Therefore the balance between the surface area (active sites/defects) and material conductivity is another important factor in optimizing the heteroatom-doped carbon nanomaterials with high ORR activities. **(iv) Alkaline medium *vs.* acidic medium for ORR.** Up to now, a huge amount of heteroatom-doped carbon nanomaterials were reported to exhibit high ORR performance. Quite a few of them even show better activities than the commercial Pt/C. The majority of those materials are operated in alkaline condition, which is probably because most heteroatom-doped carbon nanomaterials suffer from the low electrocatalytic activity or poor durability in acidic media. However, compared with alkaline media, the acidic media is commonly used in commercial proton exchange membrane fuel cells. Thus, the development of the metal-free heteroatom-doped carbon

nanomaterials with superior ORR activities in acidic media is highly desired. And exploring the exact mechanisms of these nanomaterials being operated in both alkaline and acidic media and developing electrocatalyst materials/structure that are robust in acid media is crucial for achieving high-performance, metal-free ORR electrocatalysts for future commercial applications.

Noble-metal-free transition metal-based NPs-carbon nanomaterials composites for ORR. **Alkaline medium _vs._ acidic medium for ORR.** Introducing noble-metal-free transition metal-based NPs into or onto carbon nanomaterials can lead to further improved ORR performance due to the synergetic effect between the advanced carbon nanomaterials and transition metal-based NPs. However, the current ORR activities of most these transition metal-based NPs functionalized onto or into carbon nanomaterials are still lower than that of the commercial Pt/C electrocatalysts operated in both alkaline and acidic media. Especially, the inherent drawbacks of the low conductivity of transition metal-based NPs and their poor stability in acid medium may limit the commercial application as the noble-metal-free electrocatalysts for ORR. Therefore, we believe that seeking transition metal NPs incorporated into carbon-based nanomaterials/structures with superior ORR activities (higher activity and stability) than the commercial Pt/C operated in both alkaline and acidic media is within reach. Investigating and understanding the fundamental mechanism of the stability of transition metal-based NPs on carbon nanomaterials surface and the electronic interactions between these NPs and carbon nanomaterials would be very helpful to realize such goal.

Noble-metal-free, Fe_3C-based NPs/carbon nanomaterials composites for ORR. **The working mechanism for ORR.** Hu _et al._ claimed the possible ORR mechanisms by performing control experiments on carbon nanomaterials functionalized with Fe_3C NPs as follow:[202] (1) the encased carbide NPs activate the surrounding graphitic layers, making the outer surface of the carbon layer much more active for ORR; (2) the surrounding graphitic layers can protect NPs from being etched in alkaline or acidic media, resulting in very stable ORR response. However, the control experiments do not fully support the hypothesis as the nitrogen content of Fe_3C/carbon microspheres is 0.5 wt.% (as estimated by XPS) and there are still plenty of iron atoms in these electrocatalysts, making it difficult to determine whether FeN_x sites play a role in Fe_3C/carbon microspheres catalysis.[182]

Other critical points are: **(i) The Pt/C target.** To evaluate the ORR performance of new materials, the commercially available Pt/C was often selected as the reference for comparison purpose. Till now, the Pt/C with different Pt contents have been used, such as the Pt/C with 10 wt.% Pt loading,[91, 198] 12 wt.% Pt loading,[159] 20 wt.% Pt loading,[82, 90, 107] 40 wt.% Pt loading,[102] 47.6 wt.% Pt loading,[137] and even unmentioned wt.% Pt loading.[117, 139, 149] However, in most cases, different Pt loadings can definitely lead to different performances (_e.g._, half-wave potentials and diffusion limiting currents) for ORR under the same loading amount of catalysts.[102] This means that it is very possible that the ORR

activity of the new nanomaterial is better than that Pt/C with lower wt.% Pt loading but worse than that of Pt/C with higher wt.% Pt loading. In order to strictly claim whether the ORR performance of one material is better, comparable or worse than Pt/C, it is critical to setup a standard protocol or specifically point out which kind of Pt/C is applied in the conclusive sentences. **(ii) Environmental/experimental conditions.** The activity of materials for ORR may show obvious differences under different environmental/experimental conditions. For example, the diffusion limiting current at Pt/C (20 wt.% Pt loading) obtained from Los Alamos National Laboratory (Los Alamos, NM U.S.) is lower than that from Technical University of Denmark (Lyngby, Denmark) or Changchun Institute of Applied Chemistry (Changchun, China),[200] which could be most likely due to the much higher elevation (i.e., lower atmospheric pressure and accordingly lower oxygen concentration in the base solution) of Los Alamos, New Mexico State, U.S. (~7355 feet = ~2242 m) compared to Lyngby, Denmark (~82 feet = ~25 m) or Changchun, China (~730 feet = ~222 m). Therefore, it is almost necessary to give detailed information on the environmental/experimental parameters, especially the elevation, humidity or atmospheric pressure.

This review aims to provide an update on the emerging growth of studies of the carbon nanomaterials-based noble-metal-free ORR electrocatalysts in recent years, with special emphasis on the phenomenological knowledge and the topics under debate. And it will also appeal to the scientific communities who are interested in the general areas of physical chemistry, electrochemistry, nanomaterials and nanotechnology, electrochemical energy storage, and electroanalysis. We look forward to the bright future of carbon nanomaterials-based noble-metal-free ORR electrocatalysts and are keen to see breakthroughs in the understanding of the nature of the ORR on these noble-metal-free electrocatalysts. We hope that the coming groundbreaking advancements will bring forward conceptually different scope to this active area.

Acknowledgements
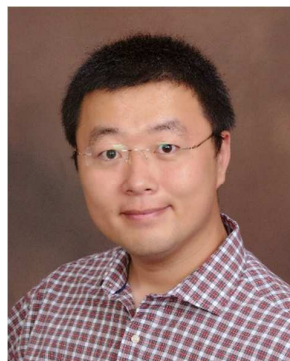
Ming Zhou is currently a Professor at Northeast Normal University (NENU). He received B.S. (2004) and M.S. (2007, Prof. Liping Guo's group) from NENU and Ph.D (2011, Prof. Shaojun Dong's group) from Changchun Institute of Applied Chemistry. Then, he did postdoctoral work with Prof. Joseph Wang at University of California, San Diego (2011), Prof. Liming Dai at Case Western Reserve University (2012), Prof. Bo Zhang at University of Washington (2013-2014), and Dr. Hsing-Lin Wang at Los Alamos National Laboratory (2015). He has published >40 papers with >2800 citations (H-index: 25). His research interests include nanomaterials for analysis and energy applications.

Hsing-Lin Wang is now a senior scientist, team leader and project leader in Physical Chemistry and Spectroscopy group, Chemistry Division, Los Alamos National Laboratory. He received his Ph.D. in Chemistry in 1992 from University of South Florida. Then, he moved to University of Pennsylvania as Postdoctoral Fellow from 1993-1995. He came to Los Alamos National Laboratory as a Postdoctoral Fellow in 1995 and became a Scientist in 1998. He has publishes over 160 papers with >6200 citations (H-index: 38) and 19 issued patents. His research interests include the synthesis, processing and applications of organic molecules and nanomaterials.

Shaojun Guo is currently a Professor of Materials Science and Engineering, and Energy&Resources Engineering, College of Engineering, Peking University. He received his BSc in chemistry from Jilin University (2005) and Ph. D from Chinese Academy of Sciences (2011). He did his postdoctoral research at Brown University (2011-2013), worked as Oppenheimer Distinguished Fellow at Los Alamos National Laboratory (2013-2015). In both 2014 and 2015, he was selected as World Highly Cited Researchers by Thomson Reuters. He has published over 150 papers with >10000 citations (H-index: 54). His research interests are in engineering nanocrystals for catalysis, renewable energy, optoelectronics and biosensors.

Notes and references

1   J. Liu, H. Mooney, V. Hull, S. J. Davis, J. Gaskell, T. Hertel, J. Lubchenco, K. C. Seto, P. Gleick, C. Kremen and S. Li, *Science*, 2015, **347**.
2   A. L. Alm, *Science*, 1981, **211**, 1379-1385.
3   *Nature*, 2010, **463**, 26-32.
4   A. S. Arico, P. Bruce, B. Scrosati, J.-M. Tarascon and W. van Schalkwijk, *Nat. Mater.*, 2005, **4**, 366-377.
5   G. Ren, G. Ma and N. Cong, *Renew. Sust. Energ. Rev.*, 2015, **41**, 225-236.
6   J. Wang, H. L. Xin and D. Wang, *Part. Part. Syst. Charact.*, 2014, **31**, 515-539.
7   H. Chang and H. Wu, *Energy Environ. Sci.*, 2013, **6**, 3483-3507.
8   Q. Li, R. Cao, J. Cho and G. Wu, *Adv. Energy Mater.*, 2014, **4**, 1301415.
9   T. M. Guer, *Chem. Rev.*, 2013, **113**, 6179-6206.
10   M. Liu, R. Zhang and W. Chen, *Chem. Rev.*, 2014, **114**, 5117-5160.
11   M. M. Nasef, *Chem. Rev.*, 2014, **114**, 12278-12329.
12   W. Wang, C. Su, Y. Wu, R. Ran and Z. Shao, *Chem. Rev.*, 2013, **113**, 8104-8151.
13   H. Zhang and P. K. Shen, *Chem. Soc. Rev.*, 2012, **41**, 2382-2394.
14   Z. Chen, D. Higgins, A. Yu, L. Zhang and J. Zhang, *Energy Environ. Sci.*, 2011, **4**, 3167-3192.
15   R. Devanathan, *Energy Environ. Sci.*, 2008, **1**, 101-119.
16   A. Hawkes, I. Staffell, D. Brett and N. Brandon, *Energy Environ. Sci.*, 2009, **2**, 729-744.
17   W. R. Grove, *Philosophical Magazine Series 3*, 1838, **13**, 430-431.
18   C. F. Schœnbein, *Philosophical Magazine Series 3*, 1839, **14**, 43-45.
19   M. Warshay and P. R. Prokopius, 1989.
20   K. A. Burke, Fuel cells for space science applications, 1st International Energy Conversion Engineering Conference, 2003.
21   R. Cohen, Gemini fuel cell system, Proc. 20th Power Sources Conf., May 1966.
22   M. Winter and R. J. Brodd, *Chem. Rev.*, 2004, **104**, 4245-4270.
23   M. Zhou and S. Dong, *Acc. Chem. Res.*, 2011, **44**, 1232-1243.
24   S. Calabrese Barton, J. Gallaway and P. Atanassov, *Chem. Rev.*, 2004, **104**, 4867-4886.
25   J. A. Cracknell, K. A. Vincent and F. A. Armstrong, *Chem. Rev.*, 2008, **108**, 2439-2461.
26   G. T. R. Palmore and G. M. Whitesides, *Enzymatic conversion of biomass for fuels production*, 1994, **566**, 271-290.
27   B. E. Logan, B. Hamelers, R. Rozendal, U. Schröder, J. Keller, S. Freguia, P. Aelterman, W. Verstraete and K. Rabaey, *Environ. Sci. Technol.*, 2006, **40**, 5181-5192.
28   M. Zhou, Y. Du, C. Chen, B. Li, D. Wen, S. Dong and E. Wang, *J. Am. Chem. Soc.*, 2010, **132**, 2172-2174.
29   M. Zhou and J. Wang, *Electroanalysis*, 2012, **24**, 197-209.
30   M. Zhou, C. Chen, Y. Du, B. Li, D. Wen, S. Dong and E. Wang, *Lab Chip*, 2010, **10**, 2932-2936.
31   M. Zhou, N. Zhou, F. Kuralay, J. R. Windmiller, S. Parkhomovsky, G. Valdés-Ramírez, E. Katz and J. Wang, *Angew. Chem. Int. Ed.*, 2012, **51**, 2686-2689.
32   C.-H. Cui and S.-H. Yu, *Acc. Chem. Res.*, 2013, **46**, 1427-1437.
33   S. Guo and E. Wang, *Acc. Chem. Res.*, 2011, **44**, 491-500.
34   A. Rinaldi, B. Mecheri, V. Garavaglia, S. Licoccia, P. Di Nardo and E. Traversa, *Energy Environ. Sci.*, 2008, **1**, 417-429.
35   Z. Zhang, J. Liu, J. Gu, L. Su and L. Cheng, *Energy Environ. Sci.*, 2014, **7**, 2535-2558.
36   C.-J. Zhong, J. Luo, P. N. Njoki, D. Mott, B. Wanjala, R. Loukrakpam, S. Lim, L. Wang, B. Fang and Z. Xu, *Energy Environ. Sci.*, 2008, **1**, 454-466.
37   H.-J. Choi, S.-M. Jung, J.-M. Seo, D. W. Chang, L. Dai and J.-B. Baek, *Nano Energy*, 2012, **1**, 534-551.
38   J. N. Tiwari, R. N. Tiwari, G. Singh and K. S. Kim, *Nano Energy*, 2013, **2**, 553-578.
39   B. C. H. Steele and A. Heinzel, *Nature*, 2001, **414**, 345-352.
40   H. A. Gasteiger, S. S. Kocha, B. Sompalli and F. T. Wagner, *Appl. Catal., B*, 2005, **56**, 9-35.
41   A. C. Chen and P. Holt-Hindle, *Chem. Rev.*, 2010, **110**, 3767-3804.
42   Y. Nie, L. Li and Z. Wei, *Chem. Soc. Rev.*, 2015, **44**, 2168-2201.
43   S. Guo, S. Zhang and S. Sun, *Angew. Chem. Int. Ed.*, 2013, **52**, 8526-8544.

44   Y. Bing, H. Liu, L. Zhang, D. Ghosh and J. Zhang, *Chem. Soc. Rev.*, 2010, **39**, 2184-2202.

45   B. E. Hayden, *Acc. Chem. Res.*, 2013, **46**, 1858-1866.

46   N. S. Porter, H. Wu, Z. Quan and J. Fang, *Acc. Chem. Res.*, 2013, **46**, 1867-1877.

47   G. Wu and P. Zelenay, *Acc. Chem. Res.*, 2013, **46**, 1878-1889.

48   J. Wu and H. Yang, *Acc. Chem. Res.*, 2013, **46**, 1848-1857.

49   A. Chen and P. Holt-Hindle, *Chem. Rev.*, 2010, **110**, 3767-3804.

50   N. Kakati, J. Maiti, S. H. Lee, S. H. Jee, B. Viswanathan and Y. S. Yoon, *Chem. Rev.*, 2014, **114**, 12397-12429.

51   Y.-J. Wang, D. P. Wilkinson and J. Zhang, *Chem. Rev.*, 2011, **111**, 7625-7651.

52   Y. Xu and B. Zhang, *Chem. Soc. Rev.*, 2014, **43**, 2439-2450.

53   H. You, S. Yang, B. Ding and H. Yang, *Chem. Soc. Rev.*, 2013, **42**, 2880-2904.

54   A. Manthiram, A. V. Murugan, A. Sarkar and T. Muraliganth, *Energy Environ. Sci.*, 2008, **1**, 621-638.

55   Y. Zheng, Y. Jiao, M. Jaroniec, Y. Jin and S. Z. Qiao, *Small*, 2012, **8**, 3550-3566.

56   M. Zhang and L. Dai, *Nano Energy*, 2012, **1**, 514-517.

57   L. Yang, Y. Zhao, S. Chen, Q. Wu, X. Wang and Z. Hu, *Chinese J. Catal.*, 2013, **34**, 1986-1991.

58   J. Liu, P. Song, Z. Ning and W. Xu, *Electrocatalysis*, 2015, **6**, 132-147.

59   N. Alonso‑Vante, *ChemPhysChem*, 2010, **11**, 2732-2744.

60   Y. Shao, G. Yin and Y. Gao, *J. Power Sources*, 2007, **171**, 558-566.

61   K. Sasaki, M. Sao and R. Adzic, *"Dissolution and Stability of Platinum in Oxygen Cathodes" in Polymer Electrolyte Fuel Cell Durability*, Springer Science, New York, 2009.

62   R. Borup, J. Meyers, B. Pivovar, Y. S. Kim, R. Mukundan, N. Garland, D. Myers, M. Wilson, F. Garzon, D. Wood, P. Zelenay, K. More, K. Stroh, T. Zawodzinski, J. Boncella, J. E. McGrath, M. Inaba, K. Miyatake, M. Hori, K. Ota, Z. Ogumi, S. Miyata, A. Nishikata, Z. Siroma, Y. Uchimoto, K. Yasuda, K.-i. Kimijima and N. Iwashita, *Chem. Rev.*, 2007, **107**, 3904-3951.

63   *See the website on Fuel Cell System Cost - 2013: http://www.energy.gov/sites/prod/files/2014/03/f11/13012_fuel_cell_system_cost_2013.pdf.*

64   *See the website on Fuel Cell Technical Team Roadmap: http://energy.gov/sites/prod/files/2014/02/f8/fctt_roadmap_june2013.pdf.*

65   Y. Hu, J. O. Jensen, W. Zhang, S. Martin, R. Chenitz, C. Pan, W. Xing, N. J. Bjerrum and Q. Li, *J. Mater. Chem. A*, 2015, **3**, 1752-1760.

66   K. Sasaki, H. Naohara, Y. Cai, Y. M. Choi, P. Liu, M. B. Vukmirovic, J. X. Wang and R. R. Adzic, *Angew. Chem. Int. Ed.*, 2010, **49**, 8602-8607.

67   F. De Bruijn, V. Dam and G. Janssen, *Fuel cells*, 2008, **8**, 3-22.

68   H. Chen, P. Pei and M. Song, *Appl. Energy*, 2015, **142**, 154-163.

69   A. Kannan, A. Kabza and J. Scholta, *J. Power Sources*, 2015, **277**, 312-316.

70   S. Chen, H. A. Gasteiger, K. Hayakawa, T. Tada and Y. Shao-Horn, *J. Electrochem. Soc.*, 2010, **157**, A82-A97.

71   P. J. Ferreira, G. J. la O', Y. Shao-Horn, D. Morgan, R. Makharia, S. Kocha and H. A. Gasteiger, *J. Electrochem. Soc.*, 2005, **152**, A2256-A2271.

72   M. K. Debe, A. K. Schmoeckel, G. D. Vernstrom and R. Atanasoski, *J. Power Sources*, 2006, **161**, 1002-1011.

73   G. J. Acres, *J. Power Sources*, 2001, **100**, 60-66.

74   C. Morrill, Apollo fuel cell System, Proceedings of the 19th Power Sources Conference, Atlantic City, NJ, 1965.

75   E. M. Cortright, *Apollo Expeditions to the Moon: The NASA History*, Courier Corporation, 2012.

76   G. Hoogers, *Fuel cell technology handbook*, CRC press, 2014.

77   S. Guo, D. Li, H. Zhu, S. Zhang, N. M. Markovic, V. R. Stamenkovic and S. Sun, *Angew. Chem. Int. Ed.*, 2013, **52**, 3465-3468.

78   S. Guo and S. Sun, *J. Am. Chem. Soc.*, 2012, **134**, 2492-2495.

79   S. Guo, S. Zhang, D. Su and S. Sun, *J. Am. Chem. Soc.*, 2013, **135**, 13879-13884.

80   S. Zhang, X. Zhang, G. Jiang, H. Zhu, S. Guo, D. Su, G. Lu and S. Sun, *J. Am. Chem. Soc.*, 2014, **136**, 7734-7739.

81   A. Zhao, J. Masa, W. Xia, A. Maljusch, M.-G. Willinger, G. Clavel, K. Xie, R. Schlögl, W. Schuhmann and M. Muhler, *J. Am.*

82   *Chem. Soc.*, 2014, **136**, 7551-7554.

Y. Liang, H. Wang, P. Diao, W. Chang, G. Hong, Y. Li, M. Gong, L. Xie, J. Zhou, J. Wang, T. Z. Regier, F. Wei and H. Dai, *J. Am. Chem. Soc.*, 2012, **134**, 15849-15857.

83   T. Sun, Q. Wu, R. Che, Y. Bu, Y. Jiang, Y. Li, L. Yang, X. Wang and Z. Hu, *ACS Catal.*, 2015, **5**, 1857-1862.

84   R. Zhang and W. Chen, *J. Mater. Chem. A*, 2013, **1**, 11457-11464.

85   Y. Liang, Y. Li, H. Wang and H. Dai, *J. Am. Chem. Soc.*, 2013, **135**, 2013-2036.

86   Y. Liang, H. Wang, J. Zhou, Y. Li, J. Wang, T. Regier and H. Dai, *J. Am. Chem. Soc.*, 2012, **134**, 3517-3523.

87   S. Guo, S. Zhang, L. Wu and S. Sun, *Angew. Chem. Int. Ed.*, 2012, **51**, 11770-11773.

88   H. Wang, Y. Liang, Y. Li and H. Dai, *Angew. Chem. Int. Ed.*, 2011, **50**, 10969-10972.

89   Y. Liang, Y. Li, H. Wang, J. Zhou, J. Wang, T. Regier and H. Dai, *Nat. Mater.*, 2011, **10**, 780-786.

90   W. Xia, R. Zou, L. An, D. Xia and S. Guo, *Energy Environ. Sci.*, 2015, **8**, 568-576.

91   S. Ci, S. Mao, Y. Hou, S. Cui, H. Kim, R. Ren, Z. Wen and J. Chen, *J. Mater. Chem. A*, 2015, **3**, 7986-7993.

92   H. Zhu, S. Zhang, Y.-X. Huang, L. Wu and S. Sun, *Nano Lett.*, 2013, **13**, 2947-2951.

93   S. Gao, X. Wei, H. Fan, L. Li, K. Geng and J. Wang, *Nano Energy*, 2015, **13**, 518-526.

94   F. Gao, G.-L. Zhao, S. Yang and J. J. Spivey, *J. Am. Chem. Soc.*, 2013, **135**, 3315-3318.

95   J. Shui, M. Wang, F. Du and L. Dai, *Science Advances*, 2015, **1**, e1400129.

96   W. Li, D. Yang, H. Chen, Y. Gao and H. Li, *Electrochim. Acta*, 2015, **165**, 191-197.

97   C. Domínguez, F. J. Pérez-Alonso, S. A. Al-Thabaiti, S. N. Basahel, A. Y. Obaid, A. O. Alyoubi, J. L. Gómez de la Fuente and S. Rojas, *Electrochim. Acta*, 2015, **157**, 158-165.

98   Y. J. Sa, C. Park, H. Y. Jeong, S.-H. Park, Z. Lee, K. T. Kim, G.-G. Park and S. H. Joo, *Angew. Chem. Int. Ed.*, 2014, **126**, 4186-4190.

99   Y. Zhao, L. Yang, S. Chen, X. Wang, Y. Ma, Q. Wu, Y. Jiang, W. Qian and Z. Hu, *J. Am. Chem. Soc.*, 2013, **135**, 1201-1204.

100   J. Xu and L. Guan, *RSC Advances*, 2013, **3**, 5577-5582.

101   D. Yu, Y. Xue and L. Dai, *J. Phys. Chem. Lett.*, 2012, **3**, 2863-2870.

102   L. Yang, S. Jiang, Y. Zhao, L. Zhu, S. Chen, X. Wang, Q. Wu, J. Ma, Y. Ma and Z. Hu, *Angew. Chem. Int. Ed.*, 2011, **50**, 7132-7135.

103   S. Wang , E. Iyyamperumal , A. Roy, Y. Xue, D. Yu and L. Dai, *Angew. Chem. Int. Ed.*, 2011, **50**, 11756-11760.

104   D. Yu, Q. Zhang and L. Dai, *J. Am. Chem. Soc.*, 2010, **132**, 15127-15129.

105   W. Xiong, F. Du, Y. Liu, A. Perez, M. Supp, T. S. Ramakrishnan, L. Dai and L. Jiang, *J. Am. Chem. Soc.*, 2010, **132**, 15839-15841.

106   Y. Tang, B. L. Allen, D. R. Kauffman and A. Star, *J. Am. Chem. Soc.*, 2009, **131**, 13200-13201.

107   K. Gong, F. Du, Z. Xia, M. Durstock and L. Dai, *Science*, 2009, **323**, 760-764.

108   J.-M. You, M. S. Ahmed, H. S. Han, J. e. Choe, Z. Üstündağ and S. Jeon, *J. Power Sources*, 2015, **275**, 73-79.

109   Z. Ma, S. Dou, A. Shen, L. Tao, L. Dai and S. Wang, *Angew. Chem. Int. Ed.*, 2015, **127**, 1908-1912.

110   Y. Han, D. Tang, Y. Yang, C. Li, W. Kong, H. Huang, Y. Liu and Z. Kang, *Nanoscale*, 2015, **7**, 5955-5962.

111   M. Favaro, L. Ferrighi, G. Fazio, L. Colazzo, C. Di Valentin, C. Durante, F. Sedona, A. Gennaro, S. Agnoli and G. Granozzi, *ACS Catal.*, 2015, **5**, 129-144.

112   S. Bag, B. Mondal, A. K. Das and C. R. Raj, *Electrochim. Acta*, 2015, **163**, 16-23.

113   Y. Zhang, X. Zhuang, Y. Su, F. Zhang and X. Feng, *J. Mater. Chem. A*, 2014, **2**, 7742-7746.

114   W. Wei, H. Liang, K. Parvez, X. Zhuang, X. Feng and K. Müllen, *Angew. Chem. Int. Ed.*, 2014, **53**, 1570-1574.

115   F. Razmjooei, K. P. Singh, M. Y. Song and J.-S. Yu, *Carbon*, 2014, **78**, 257-267.

116   Y. Li, M. Li, L. Jiang, L. Lin, L. Cui and X. He, *Phys. Chem. Chem. Phys.*, 2014, **16**, 23196-23205.

117   H.-P. Cong, P. Wang, M. Gong and S.-H. Yu, *Nano Energy*, 2014,

3, 55-63.

118 C. a. Cao, X. Zhuang, Y. Su, Y. Zhang, F. Zhang, D. Wu and X. Feng, *Polm. Chem.*, 2014, **5**, 2057-2064.

119 X. Bo, C. Han, Y. Zhang and L. Guo, *ACS Applied Materials & Interfaces*, 2014, **6**, 3023-3030.

120 I.-Y. Jeon, S. Zhang, L. Zhang, H.-J. Choi, J.-M. Seo, Z. Xia, L. Dai and J.-B. Baek, *Adv. Mater.*, 2013, **25**, 6138-6145.

121 I.-Y. Jeon, H.-J. Choi, M. Choi, J.-M. Seo, S.-M. Jung, M.-J. Kim, S. Zhang, L. Zhang, Z. Xia, L. Dai, N. Park and J.-B. Baek, *Sci. Rep.*, 2013, **3**.

122 Z. Yao, H. Nie, Z. Yang, X. Zhou, Z. Liu and S. Huang, *Chem. Commun.*, 2012, **48**, 1027-1029.

123 Z. Yang, Z. Yao, G. Li, G. Fang, H. Nie, Z. Liu, X. Zhou, X. a. Chen and S. Huang, *ACS Nano*, 2012, **6**, 205-211.

124 S. Yang, L. Zhi, K. Tang, X. Feng, J. Maier and K. Müllen, *Adv. Funct. Mater.*, 2012, **22**, 3634-3640.

125 G. Wu, N. H. Mack, W. Gao, S. Ma, R. Zhong, J. Han, J. K. Baldwin and P. Zelenay, *ACS Nano*, 2012, **6**, 9764-9776.

126 S. Wang, L. Zhang, Z. Xia, A. Roy, D. W. Chang, J.-B. Baek and L. Dai, *Angew. Chem. Int. Ed.*, 2012, **51**, 4209-4212.

127 J. Liang, Y. Jiao, M. Jaroniec and S. Z. Qiao, *Angew. Chem. Int. Ed.*, 2012, **51**, 11496-11500.

128 Q. Li, S. Zhang, L. Dai and L.-s. Li, *J. Am. Chem. Soc.*, 2012, **134**, 18932-18935.

129 L. Lai, J. R. Potts, D. Zhan, L. Wang, C. K. Poh, C. Tang, H. Gong, Z. Shen, J. Lin and R. S. Ruoff, *Energy Environ. Sci.*, 2012, **5**, 7936-7942.

130 S. Yang, X. Feng, X. Wang and K. Müllen, *Angew. Chem. Int. Ed.*, 2011, **50**, 5339-5343.

131 Z.-H. Sheng, L. Shao, J.-J. Chen, W.-J. Bao, F.-B. Wang and X.-H. Xia, *ACS Nano*, 2011, **5**, 4350-4358.

132 D. Geng, Y. Chen, Y. Chen, Y. Li, R. Li, X. Sun, S. Ye and S. Knights, *Energy Environ. Sci.*, 2011, **4**, 760-764.

133 L. Qu, Y. Liu, J.-B. Baek and L. Dai, *ACS Nano*, 2010, **4**, 1321-1326.

134 Z. Zhao, Y. Dai, G. Ge, Q. Mao, Z. Rong and G. Wang, *ChemCatChem*, 2015, **7**, 1070-1077.

135 J. Zhang, Z. Zhao, Z. Xia and L. Dai, *Nat. Nanotechnol.*, 2015, **10**, 444–452.

136 T. Y. Ma, J. Ran, S. Dai, M. Jaroniec and S. Z. Qiao, *Angew. Chem. Ed.*, 2015, **54**, 4646-4650.

137 Z. Liu, X. Fu, M. Li, F. Wang, Q. Wang, G. Kang and F. Peng, *J. Mater. Chem. A*, 2015, **3**, 3289-3293.

138 X. Liu, Y. Zhou, W. Zhou, L. Li, S. Huang and S. Chen, *Nanoscale*, 2015, **7**, 6136-6142.

139 Y. Li, H. Zhang, P. Liu, Y. Wang, H. Yang, Y. Li and H. Zhao, *Electrochem. Commun.*, 2015, **51**, 6-10.

140 S. Gao, H. Liu, K. Geng and X. Wei, *Nano Energy*, 2015, **12**, 785-793.

141 S. Gao, K. Geng, H. Liu, X. Wei, M. Zhang, P. Wang and J. Wang, *Energy Environ. Sci.*, 2015, **8**, 221-229.

142 L. Chen, C. Xu, R. Du, Y. Mao, C. Xue, L. Chen, L. Qu, J. Zhang and T. Yi, *J. Mater. Chem. A*, 2015, **3**, 5617-5627.

143 L. Chen, X. Cui, L. Zhang, Y. Wang, M. Wang, F. Cui, C. Wei, J. Feng, T. Ge, W. Ren and J. Shi, *ChemSusChem*, 2015, **8**, 623-627.

144 Y. Zhao, C. Hu, L. Song, L. Wang, G. Shi, L. Dai and L. Qu, *Energy Environ. Sci.*, 2014, **7**, 1913-1918.

145 Y. Zhang, W.-J. Jiang, X. Zhang, L. Guo, J.-S. Hu, Z. Wei and L.-J. Wan, *Phys. Chem. Chem. Phys.*, 2014, **16**, 13605-13609.

146 D.-S. Yang, D. Bhattacharjya, M. Y. Song and J.-S. Yu, *Carbon*, 2014, **67**, 736-743.

147 P. Xu, D. Wu, L. Wan, P. Hu and R. Liu, *J. Colloid Interface Sci.*, 2014, **421**, 160-164.

148 H.-W. Liang, X. Zhuang, S. Brüller, X. Feng and K. Müllen, *Nat. Commun.*, 2014, **5**.

149 Y. Li, H. Zhang, Y. Wang, P. Liu, H. Yang, X. Yao, D. Wang, Z. Tang and H. Zhao, *Energy Environ. Sci.*, 2014, **7**, 3720-3726.

150 J.-S. Li, S.-L. Li, Y.-J. Tang, K. Li, L. Zhou, N. Kong, Y.-Q. Lan, J.-C. Bao and Z.-H. Dai, *Sci. Rep.*, 2014, **4**.

151 Y. Ito, H. J. Qiu, T. Fujita, Y. Tanabe, K. Tanigaki and M. Chen, *Adv. Mater.*, 2014, **26**, 4145-4150.

152 C. Hu, L. Wang, Y. Zhao, M. Ye, Q. Chen, Z. Feng and L. Qu, *Nanoscale*, 2014, **6**, 8002-8009.

153 W. He, C. Jiang, J. Wang and L. Lu, *Angew. Chem. Int. Ed.*, 2014,

154 S. Gao, Y. Chen, H. Fan, X. Wei, C. Hu, H. Luo and L. Qu, *J. Mater. Chem. A*, 2014, **2**, 3317-3324.

155 Z. Cui, S. Wang, Y. Zhang and M. Cao, *J. Power Sources*, 2014, **259**, 138-144.

156 J. Y. Cheon, J. H. Kim, J. H. Kim, K. C. Goddeti, J. Y. Park and S. H. Joo, *J. Am. Chem. Soc.*, 2014, **136**, 8875-8878.

157 P. Chen, L.-K. Wang, G. Wang, M.-R. Gao, J. Ge, W.-J. Yuan, Y.-H. Shen, A.-J. Xie and S.-H. Yu, *Energy Environ. Sci.*, 2014, **7**, 4095-4103.

158 Y. Xue, D. Yu, L. Dai, R. Wang, D. Li, A. Roy, F. Lu, H. Chen, Y. Liu and J. Qu, *Phys. Chem. Chem. Phys.*, 2013, **15**, 12220-12226.

159 C. Hu, Y. Xiao, Y. Zhao, N. Chen, Z. Zhang, M. Cao and L. Qu, *Nanoscale*, 2013, **5**, 2726-2733.

160 Y. Zhao, C. Hu, Y. Hu, H. Cheng, G. Shi and L. Qu, *Angew. Chem. Int. Ed.*, 2012, **51**, 11371-11375.

161 D.-S. Yang, D. Bhattacharjya, S. Inamdar, J. Park and J.-S. Yu, *J. Am. Chem. Soc.*, 2012, **134**, 16127-16130.

162 Z. Jin, H. Nie, Z. Yang, J. Zhang, Z. Liu, X. Xu and S. Huang, *Nanoscale*, 2012, **4**, 6455-6460.

163 S. Chen, J. Bi, Y. Zhao, L. Yang, C. Zhang, Y. Ma, Q. Wu, X. Wang and Z. Hu, *Adv. Mater.*, 2012, **24**, 5593-5597.

164 Y. Zheng, Y. Jiao, J. Chen, J. Liu, J. Liang, A. Du, W. Zhang, Z. Zhu, S. C. Smith, M. Jaroniec, G. Q. Lu and S. Z. Qiao, *J. Am. Chem. Soc.*, 2011, **133**, 20116-20119.

165 W. Yang, T.-P. Fellinger and M. Antonietti, *J. Am. Chem. Soc.*, 2011, **133**, 206-209.

166 D. S. Su, J. Zhang, B. Frank, A. Thomas, X. Wang, J. Paraknowitsch and R. Schlögl, *ChemSusChem*, 2010, **3**, 169-180.

167 R. Liu, D. Wu, X. Feng and K. Müllen, *Angew. Chem. Int. Ed.*, 2010, **49**, 2565-2569.

168 L. Dai, Y. Xue, L. Qu, H.-J. Choi and J.-B. Baek, *Chem. Rev.*, 2015, **115**, 4823–4892.

169 D. Shin, B. Jeong, M. Choun, J. D. Ocon and J. Lee, *RSC Advances*, 2015, **5**, 1571-1580.

170 D. Geng, N. Ding, T. S. Andy Hor, Z. Liu, X. Sun and Y. Zong, *J. Mater. Chem. A*, 2015, **3**, 1795-1810.

171 D.-W. Wang and D. Su, *Energy Environ. Sci.*, 2014, **7**, 576-591.

172 T.-F. Hung, S.-H. Chen, M.-H. Tu, Z.-H. Lu, C. K. Chen, R.-S. Liu, H. F. Greer, W. Zhou and M.-Y. Lo, *J. Chinese Chem. Soc.*, 2014, **61**, 93-100.

173 R. Othman, A. L. Dicks and Z. Zhu, *Int. J. Hydrogen Energy*, 2012, **37**, 357-372.

174 M. Sun, H. Liu, Y. Liu, J. Qu and J. Li, *Nanoscale*, 2015, **7**, 1250-1269.

175 F. Jaouen, E. Proietti, M. Lefevre, R. Chenitz, J.-P. Dodelet, G. Wu, H. T. Chung, C. M. Johnston and P. Zelenay, *Energy Environ. Sci.*, 2011, **4**, 114-130.

176 X. Wang, G. Sun, P. Routh, D.-H. Kim, W. Huang and P. Chen, *Chem. Soc. Rev.*, 2014, **43**, 7067-7098.

177 E. H. L. Falcao and F. Wudl, *J. Chem. Technol. Biotechnol.*, 2007, **82**, 524-531.

178 R. L. McCreery, in *Electroanal. Chem.*, ed. A. J. Bard, Dekker, New York, 1991, vol. 17, pp. 221-374.

179 R. L. McCreery, *Chem. Rev.*, 2008, **108**, 2646-2687.

180 R. McCreery, A. Bergren, A. Morteza-Najarian, S. Y. Sayed and H. Yan, *Faraday Discuss.*, 2014, **172**, 9-25.

181 F. M. Perkin, *Trans. Faraday Soc.*, 1908, **3**, 205-219.

182 J.-P. Dodelet, R. Chenitz, L. Yang and M. Lefèvre, *ChemCatChem*, 2014, **6**, 1866-1867.

183 J. Wang, *Electroanalysis*, 2005, **17**, 7-14.

184 P. Yáñez-Sedeño, J. M. Pingarrón, J. Riu and F. X. Rius, *Trend. Anal. Chem.*, 2010, **29**, 939-953.

185 W. Yang, K. R. Ratinac, S. P. Ringer, P. Thordarson, J. J. Gooding and F. Braet, *Angew. Chem. Int. Ed.*, 2010, **49**, 2114-2138.

186 S. K. Vashist, D. Zheng, K. Al-Rubeaan, J. H. T. Luong and F.-S. Sheu, *Biotechnol. Adv.*, 2011, **29**, 169-188.

187 Y. Shao, J. Wang, H. Wu, J. Liu, I. A. Aksay and Y. Lin, *Electroanalysis*, 2010, **22**, 1027-1036.

188 S. Guo and S. Dong, *Chem. Soc. Rev.*, 2011, **40**, 2644-2672.

189 A. Ambrosi, C. K. Chua, A. Bonanni and M. Pumera, *Chem. Rev.*, 2014, **114**, 7150-7188.

190 A. Walcarius, *Trend. Anal. Chem.*, 2012, **38**, 79-97.

191 A. Walcarius, *Chem. Soc. Rev.*, 2013, **42**, 4098-4140.

53, 9503-9507.

192   M. Zhou and S. Guo, *ChemCatChem*, 2015, **7**, 2744-2764.
193   Q. Li, N. Mahmood, J. Zhu, Y. Hou and S. Sun, *Nano Today*, 2014, **9**, 668-683.
194   Y. Zheng, Y. Jiao and S. Z. Qiao, *Adv. Mater.*, 2015, **27**, 5372-5378.
195   Y. Zheng, Y. Jiao, M. Jaroniec and S. Z. Qiao, *Angew. Chem. Int. Ed.*, 2015, **54**, 52-65.
196   J. Duan, S. Chen, M. Jaroniec and S. Z. Qiao, *ACS Catal.*, 2015, **5**, 5207-5234.
197   Y. Liang, Y. Li, H. Wang, J. Zhou, J. Wang, T. Regier and H. Dai, *Nat Mater*, 2011, **10**, 780-786.
198   Z. Wen, S. Ci, F. Zhang, X. Feng, S. Cui, S. Mao, S. Luo, Z. He and J. Chen, *Adv. Mater.*, 2012, **24**, 1399-1404.
199   W. Yang, X. Liu, X. Yue, J. Jia and S. Guo, *J. Am. Chem. Soc.*, 2015, **137**, 1436-1439.
200   Y. Hu, J. O. Jensen, W. Zhang, Y. Huang, L. N. Cleemann, W. Xing, N. J. Bjerrum and Q. Li, *ChemSusChem*, 2014, **7**, 2099-2103.
201   J.-S. Lee, G. S. Park, S. T. Kim, M. Liu and J. Cho, *Angew. Chem. Int. Ed.*, 2013, **52**, 1026-1030.
202   Y. Hu, J. O. Jensen, W. Zhang, L. N. Cleemann, W. Xing, N. J. Bjerrum and Q. Li, *Angew. Chem. Int. Ed.*, 2014, **53**, 3675-3679.
203   W. Yang, Y. Zhai, X. Yue, Y. Wang and J. Jia, *Chem. Commun.*, 2014, **50**, 11151-11153.
204   S. Zhao, H. Yin, L. Du, L. He, K. Zhao, L. Chang, G. Yin, H. Zhao, S. Liu and Z. Tang, *ACS Nano*, 2014, **8**, 12660-12668.
205   Y. Li, Y. Zhao, H. Cheng, Y. Hu, G. Shi, L. Dai and L. Qu, *Journal of the American Chemical Society*, 2012, **134**, 15-18.
206   X. Gong, S. Liu, C. Ouyang, P. Strasser and R. Yang, *ACS Catal.*, 2015, **5**, 920-927.
207   D. C. Higgins, M. A. Hoque, F. Hassan, J.-Y. Choi, B. Kim and Z. Chen, *ACS Catal.*, 2014, **4**, 2734-2740.
208   F. Gao, G.-L. Zhao and S. Yang, *ACS Catal.*, 2014, **4**, 1267-1273.
209   P. Zhang, F. Sun, Z. Xiang, Z. Shen, J. Yun and D. Cao, *Energy Environ. Sci.*, 2014, **7**, 442-450.
210   L. Feng, Y. Yan, Y. Chen and L. Wang, *Energy Environ. Sci.*, 2011, **4**, 1892-1899.
211   H. Jin, H. Zhang, H. Zhong and J. Zhang, *Energy Environ. Sci.*, 2011, **4**, 3389-3394.
212   X. Sun, Y. Zhang, P. Song, J. Pan, L. Zhuang, W. Xu and W. Xing, *ACS Catal.*, 2013, **3**, 1726-1729.
213   G. Tuci, C. Zafferoni, P. D'Ambrosio, S. Caporali, M. Ceppatelli, A. Rossin, T. Tsoufis, M. Innocenti and G. Giambastiani, *ACS Catal.*, 2013, **3**, 2108-2111.
214   Y. Jiao, Y. Zheng, M. Jaroniec and S. Z. Qiao, *Chem. Soc. Rev.*, 2015, **44**, 2060-2086.
215   S. Mao, Z. Wen, T. Huang, Y. Hou and J. Chen, *Energy Environ. Sci.*, 2014, **7**, 609-616.
216   Y. Hu, X. Zhao, Y. Huang, Q. Li, N. J. Bjerrum, C. Liu and W. Xing, *J. Power Sources*, 2013, **225**, 129-136.
217   G. Yang, W. Choi, X. Pu and C. Yu, *Energy Environ. Sci.*, 2015, **8**, 1799-1807.
218   U. I. Kramm, M. Lefèvre, N. Larouche, D. Schmeisser and J.-P. Dodelet, *J. Am. Chem. Soc.*, 2014, **136**, 978-985.
219   J. Liu, X. Sun, P. Song, Y. Zhang, W. Xing and W. Xu, *Adv. Mater.*, 2013, **25**, 6879-6883.
220   A. K. Geim and K. S. Novoselov, *Nat. Mater.*, 2007, **6**, 183-191.
221   H. W. Kroto, J. R. Heath, S. C. O'Brien, R. F. Curl and R. E. Smalley, *Nature*, 1985, **318**, 162-163.
222   R. F. Curl, *Angew. Chem. Int. Ed.*, 1997, **36**, 1566-1576.
223   H. Kroto, *Angew. Chem. Int. Ed.*, 1997, **36**, 1578-1593.
224   R. E. Smalley, *Angew. Chem. Int. Ed.*, 1997, **36**, 1594-1601.
225   C.-C. Chen, S. P. Kelty and C. M. Lieber, *Science*, 1991, **253**, 886-888.
226   L. O. S. Bulhoes, Y. S. Obeng and A. J. Bard, *Chem. Mater.*, 1993, **5**, 110-114.
227   H. Imahori and Y. Sakata, *Adv. Mater.*, 1997, **9**, 537-546.
228   L. Echegoyen and L. E. Echegoyen, *Acc. Chem. Res.*, 1998, **31**, 593-601.
229   S. Iijima, *Nature*, 1991, **354**, 56-58.
230   P. M. Ajayan, *Chem. Rev.*, 1999, **99**, 1787-1800.
231   P. Poncharal, Z. L. Wang, D. Ugarte and W. A. de Heer, *Science*, 1999, **283**, 1513-1516.
232   J. Kong, N. R. Franklin, C. Zhou, M. G. Chapline, S. Peng, K.

Cho and H. Dai, *Science*, 2000, **287**, 622-625.
233   R. Vieira, C. Pham-Huu, N. Keller and M. J. Ledoux, *Chem. Commun.*, 2002, DOI: 10.1039/B202032G, 954-955.
234   S. Fan, M. G. Chapline, N. R. Franklin, T. W. Tombler, A. M. Cassell and H. Dai, *Science*, 1999, **283**, 512-514.
235   P. Kim and C. M. Lieber, *Science*, 1999, **286**, 2148-2150.
236   H. Dai, J. H. Hafner, A. G. Rinzler, D. T. Colbert and R. E. Smalley, *Nature*, 1996, **384**, 147-150.
237   L. Dai, A. Patil, X. Gong, Z. Guo, L. Liu, Y. Liu and D. Zhu, *ChemPhysChem*, 2003, **4**, 1150-1169.
238   M. Lefèvre, E. Proietti, F. Jaouen and J.-P. Dodelet, *Science*, 2009, **324**, 71-74.
239   J. Yang, D.-J. Liu, N. N. Kariuki and L. X. Chen, *Chem. Commun.*, 2008, **3**, 329-331.
240   A. Titov, P. Zapol, P. Král, D.-J. Liu, H. Iddir, K. Baishya and L. A. Curtiss, *J. Phys. Chem. C*, 2009, **113**, 21629-21634.
241   S. Kundu, T. C. Nagaiah, W. Xia, Y. Wang, S. V. Dommele, J. H. Bitter, M. Santa, G. Grundmeier, M. Bron, W. Schuhmann and M. Muhler, *J. Phys. Chem. C*, 2009, **113**, 14302-14310.
242   Q. Shi, F. Peng, S. Liao, H. Wang, H. Yu, Z. Liu, B. Zhang and D. Su, *J. Mater. Chem. A*, 2013, **1**, 14853-14857.
243   D.-W. Wang, F. Li, Z.-G. Chen, G. Q. Lu and H.-M. Cheng, *Chem. Mater.*, 2008, **20**, 7195-7200.
244   Y. T. Lee, N. S. Kim, S. Y. Bae, J. Park, S.-C. Yu, H. Ryu and H. J. Lee, *J. Phys. Chem. B*, 2003, **107**, 12958-12963.
245   K. S. Novoselov, A. K. Geim, S. V. Morozov, D. Jiang, Y. Zhang, S. V. Dubonos, I. V. Grigorieva and A. A. Firsov, *Science*, 2004, **306**, 666-669.
246   A. K. Geim, *Angew. Chem. Int. Ed.*, 2011, **50**, 6966-6985.
247   K. S. Novoselov, *Angew. Chem. Int. Ed.*, 2011, **50**, 6986-7002.
248   C. Lee, X. Wei, J. W. Kysar and J. Hone, *Science*, 2008, **321**, 385-388.
249   A. A. Balandin, S. Ghosh, W. Bao, I. Calizo, D. Teweldebrhan, F. Miao and C. N. Lau, *Nano Lett.*, 2008, **8**, 902-907.
250   S. Park and R. S. Ruoff, *Nat. Nanotechnol.*, 2009, **4**, 217-224.
251   C. N. R. Rao, A. K. Sood, K. S. Subrahmanyam and A. Govindaraj, *Angew. Chem. Int. Ed.*, 2009, **48**, 7752-7777.
252   Y. Zhang, Y.-W. Tan, H. L. Stormer and P. Kim, *Nature*, 2005, **438**, 201-204.
253   S. Latil and L. Henrard, *Phys. Rev. Lett.*, 2006, **97**, 036803.
254   K. V. Krishna, C. Menard-Moyon, S. Verma and A. Bianco, *Nanomedicine*, 2013, **8**, 1669-1688.
255   Y. F. Ma, H. Shen, X. L. Tu and Z. J. Zhang, *Nanomedicine*, 2014, **9**, 1565-1580.
256   R. J. Young, I. A. Kinloch, L. Gong and K. S. Novoselov, *Compos. Sci. Technol.*, 2012, **72**, 1459-1476.
257   Y. Lee and J. H. Ahn, *NANO*, 2013, **8**.
258   J. D. Roy-Mayhew and I. A. Aksay, *Chem. Rev.*, 2014, **114**, 6323-6348.
259   H. J. Tang, C. M. Hessel, J. Y. Wang, N. L. Yang, R. B. Yu, H. J. Zhao and D. Wang, *Chem. Soc. Rev.*, 2014, **43**, 4281-4299.
260   Q. B. Zheng, Z. G. Li, J. H. Yang and J. K. Kim, *Progress in Materials Science*, 2014, **64**, 200-247.
261   K. S. Kim, Y. Zhao, H. Jang, S. Y. Lee, J. M. Kim, K. S. Kim, J.-H. Ahn, P. Kim, J.-Y. Choi and B. H. Hong, *Nature*, 2009, **457**, 706-710.
262   S. Gao, Y. Chen, H. Fan, X. Wei, C. Hu, L. Wang and L. Qu, *J. Mater. Chem. A*, 2014, **2**, 6320-6325.
263   Y. Jiao, Y. Zheng, M. Jaroniec and S. Z. Qiao, *J. Am. Chem. Soc.*, 2014, **136**, 4394-4403.
264   J.-i. Aihara, *J. Phys. Chem. A*, 1999, **103**, 7487-7495.
265   L. Zhang, J. Niu, L. Dai and Z. Xia, *Langmuir*, 2012, **28**, 7542-7550.
266   H.-W. Liang, Z.-Y. Wu, L.-F. Chen, C. Li and S.-H. Yu, *Nano Energy*, 2015, **11**, 366-376.
267   Z.-S. Wu, S. Yang, Y. Sun, K. Parvez, X. Feng and K. Müllen, *J. Am. Chem. Soc.*, 2012, **134**, 9082-9085.
268   J. Liang, R. F. Zhou, X. M. Chen, Y. H. Tang and S. Z. Qiao, *Adv. Mater.*, 2014, **26**, 6074-6079.
269   C. Zhang, N. Mahmood, H. Yin, F. Liu and Y. Hou, *Adv. Mater.*, 2013, **25**, 4932-4937.
270   Y. Zheng, Y. Jiao, L. Ge, M. Jaroniec and S. Z. Qiao, *Angew. Chem. Int. Ed.*, 2013, **52**, 3110-3116.
271   D. Deng, L. Yu, X. Chen, G. Wang, L. Jin, X. Pan, J. Deng, G.

Sun and X. Bao, *Angew. Chem. Int. Ed.*, 2013, **52**, 371-375.

272   J. H. Hafner, M. J. Bronikowski, B. R. Azamian, P. Nikolaev, A. G. Rinzler, D. T. Colbert, K. A. Smith and R. E. Smalley, *Chem. Phys. Lett.*, 1998, **296**, 195-202.

273   D. Takagi, Y. Homma, H. Hibino, S. Suzuki and Y. Kobayashi, *Nano Lett.*, 2006, **6**, 2642-2645.

274   M. Pumera, A. Ambrosi and E. L. K. Chng, *Chem. Sci.*, 2012, **3**, 3347-3355.

275   C. E. Banks, A. Crossley, C. Salter, S. J. Wilkins and R. G. Compton, *Angew. Chem. Int. Ed.*, 2006, **45**, 2533-2537.

276   B. Šljukić, C. E. Banks and R. G. Compton, *Nano Lett.*, 2006, **6**, 1556-1558.

277   C. Batchelor-McAuley, G. G. Wildgoose, R. G. Compton, L. Shao and M. L. H. Green, *Sens. Actuators B: Chem.*, 2008, **132**, 356-360.

278   X. Dai, G. G. Wildgoose and R. G. Compton, *Analyst*, 2006, **131**, 901-906.

279   A. Ambrosi and M. Pumera, *Chem. Eur. J*, 2010, **16**, 10946-10949.

280   E. L. K. Chng and M. Pumera, *Electrochem. Commun.*, 2011, **13**, 781-784.

281   E. J. E. Stuart and M. Pumera, *Chem. Asian J.*, 2011, **6**, 804-807.

282   E. J. E. Stuart and M. Pumera, *Chem. Eur. J*, 2011, **17**, 5544-5548.

283   L. Wang and M. Pumera, *Chem. Commun.*, 2014, **50**, 12662-12664.

284   M. Pumera, H. Iwai and Y. Miyahara, *ChemPhysChem*, 2009, **10**, 1770-1773.

285   M. Pumera and H. Iwai, *J. Phys. Chem. C*, 2009, **113**, 4401-4405.

286   A. Ambrosi, C. K. Chua, B. Khezri, Z. Sofer, R. D. Webster and M. Pumera, *Proc. Natl. Acad. Sci.*, 2012, **109**, 12899-12904.

287   A. Ambrosi, S. Y. Chee, B. Khezri, R. D. Webster, Z. Sofer and M. Pumera, *Angew. Chem. Int. Ed.*, 2012, **51**, 500-503.

288   C. H. A. Wong, Z. Sofer, M. Kubesova, J. Kucera, S. Matejkova and M. Pumera, *Proc. Natl. Acad. Sci.*, 2014, **111**, 13774-13779.

289   A. Ambrosi and M. Pumera, *Nanoscale*, 2014, **6**, 472-476.

290   X. Yang, X. Li, X. Ma, L. Jia and L. Zhu, *Electroanalysis*, 2014, **26**, 139-146.

291   W. S. Hummers and R. E. Offeman, *J. Am. Chem. Soc.*, 1958, **80**, 1339-1339.

292   A. Y. S. Eng, A. Ambrosi, C. K. Chua, F. Šaněk, Z. Sofer and M. Pumera, *Chem. Eur. J*, 2013, **19**, 12673-12683.

293   R. A. Sidik, A. B. Anderson, N. P. Subramanian, S. P. Kumaraguru and B. N. Popov, *J. Phys. Chem. B*, 2006, **110**, 1787-1793.

294   S.-F. Huang, K. Terakura, T. Ozaki, T. Ikeda, M. Boero, M. Oshima, J.-i. Ozaki and S. Miyata, *Physical Review B*, 2009, **80**, 235410.

295   D. Deng, X. Pan, L. Yu, Y. Cui, Y. Jiang, J. Qi, W.-X. Li, Q. Fu, X. Ma, Q. Xue, G. Sun and X. Bao, *Chem. Mater.*, 2011, **23**, 1188-1193.